INFORMATION TO USERS

This reproduction was made from a copy of a document sent to us for microfilming. While the most advanced technology has been used to photograph and reproduce this document, the quality of the reproduction is heavily dependent upon the quality of the material submitted.

The following explanation of techniques is provided to help clarify markings or notations which may appear on this reproduction.

1. The sign or "target" for pages apparently lacking from the document photographed is "Missing Page(s)". If it was possible to obtain the missing page(s) or section, they are spliced into the film along with adjacent pages. This may have necessitated cutting through an image and duplicating adjacent pages to assure complete continuity.

2. When an image on the film is obliterated with a round black mark, it is an indication of either blurred copy because of movement during exposure, duplicate copy, or copyrighted materials that should not have been filmed. For blurred pages, a good image of the page can be found in the adjacent frame. If copyrighted materials were deleted, a target note will appear listing the pages in the adjacent frame.

3. When a map, drawing or chart, etc., is part of the material being photographed, a definite method of "sectioning" the material has been followed. It is customary to begin filming at the upper left hand corner of a large sheet and to continue from left to right in equal sections with small overlaps. If necessary, sectioning is continued again—beginning below the first row and continuing on until complete.

4. For illustrations that cannot be satisfactorily reproduced by xerographic means, photographic prints can be purchased at additional cost and inserted into your xerographic copy. These prints are available upon request from the Dissertations Customer Services Department.

5. Some pages in any document may have indistinct print. In all cases the best available copy has been filmed.

University Microfilms International
300 N. Zeeb Road
Ann Arbor, MI 48106

Downloaded from SHAREOK. Persistent Handle URL: https://hdl.handle.net/11244/5145

8324873

Brandes, Edward Alan

RELATIONSHIPS BETWEEN THUNDERSTORM MESOSCALE CIRCULATION AND TORNADOGENESIS

The University of Oklahoma PH.D. 1983

University
Microfilms
International 300 N. Zeeb Road, Ann Arbor, MI 48106

THE UNIVERSITY OF OKLAHOMA

GRADUATE COLLEGE

RELATIONSHIPS BETWEEN THUNDERSTORM MESOSCALE CIRCULATION AND TORNADOGENESIS

A DISSERTATION

SUBMITTED TO THE GRADUATE FACULTY

in partial fulfillment of the requirements for the

degree of

DOCTOR OF PHILOSOPHY

By

EDWARD A. BRANDES

Norman, Oklahoma

1983

RELATIONSHIPS BETWEEN THUNDERSTORM MESOSCALE

CIRCULATION AND TORNADOGENESIS

Approved by

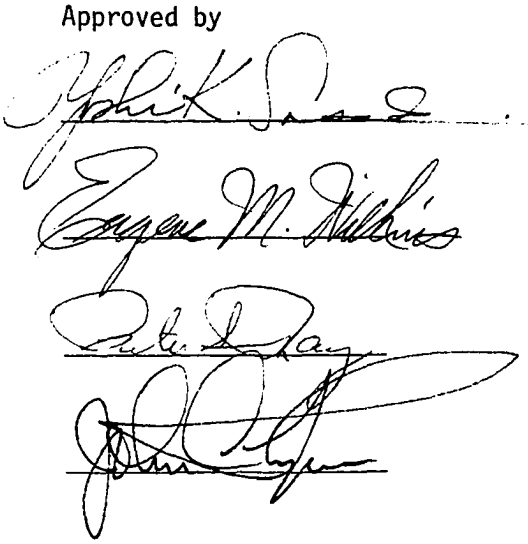

DISSERTATION COMMITTEE

TABLE OF CONTENTS

	Page
ACKNOWLEDGMENTS	iii
ABSTRACT	iv
LIST OF SYMBOLS AND NOTATION	vi
I. INTRODUCTION	1
II. THE GOVERNING EQUATIONS	8
A. Vorticity Equation	8
B. Computation of Pressure and Potential Temperature Perturbations	13
III. DATA	18
A. Radar Data Synthesis and Error in Derived Wind Fields	18
B. Data Processing: Thermodynamic Retrieval	23
1. Filling of Data Voids and Transformation to a Staggered Grid	23
2. Base State, Computation of Condensate Mixing Ratio and Neglect of Water Vapor Perturbations	26
3. Computation of Time Derivatives	27
C. Trajectory Analysis	28
D. Additional Remarks	28
IV. OBSERVATIONS	29
A. The Del City-Edmond Storm of 20 May 1977	29
1. 1826 CST: Pretornadic Stage	29

		Page
	2. 1845 CST: Tornadic Stage	47
	3. Del City-Edmond Storm Summary	65
B.	The Oklahoma City Storm of 8 June 1974	66
	1. 1315 CST: Early Storm Development	67
	2. 1409 CST: Pretornadic Mesocyclone	72
	3. 1420 CST: Tornadic Mesocyclone	79
	4. 1432 CST: Mesocyclone Decline	92
	5. Oklahoma City Storm Summary	102
C.	The Harrah Storm of 8 June 1974	103
	1. 1515 CST: Early Mesocyclone Development	105
	2. 1530 CST: Mesocyclone Intensification and Appearance of Incipient Tornado	112
	3. 1543 CST: Further Mesocyclone Intensification	115
	4. 1553 CST: Tornadic Stage	129
	5. 1603 CST: Tornado Dissipation	139
	6. 1611 CST: Mesocyclone Decline	148
	7. Harrah Storm Summary	159
V.	COMPARISON WITH NUMERICAL SIMULATIONS OF SEVERE THUNDERSTORMS	161
VI.	SUMMARY AND CONCLUSIONS	165
VII.	REFERENCES	172
APPENDICES		177
A.	PARAMETERIZATION OF SUBGRID TURBULENCE	177
B.	DERIVATION OF THE ELLIPTIC EQUATIONS FOR PRESSURE AND TEMPERATURE	179
C.	RESPONSE OF A TRUNCATED GAUSSIAN WEIGHT FUNCTION	183

ACKNOWLEDGMENTS

I am grateful to my mentor, Dr. Yoshi K. Sasaki, for his encouragement, guidance and council over the years I have known him and to Drs. John McCarthy, John C. Thompson and Eugene Wilkins for their helpful suggestions and discussions regarding this research. A special acknowledgment is due Dr. Peter S. Ray for his critique of the manuscript and stimulating questions raised, many of which are addressed in the text. Drs. Robert Davies-Jones and Dusan Zrnic provided valuable technical reviews and assistance. I wish to thank Ms. Sandra McPherson who typed the manuscript and Ms. Joan Kimpel and Mr. Robert Goldsmith who developed the numerous figures. Drs. Joseph B. Klemp and Robert B. Wilhelmson graciously provided output from their numerical thunderstorm model which was used to verify the computer algorithms for retrieving temperature and pressure. I am most grateful for the support and understanding of my wife Barbara and my children throughout the course of this research.

ABSTRACT

A methodology for obtaining pressure and potential temperature deviations in thunderstorm flows reconstructed from Doppler radar observations is described. Results are combined with detailed vorticity analyses to study properties of severe thunderstorm circulations (mesocyclones) known to have spawned tornadoes.

The data show that vertical vorticity production in tornadic storms begins at the very roots of the updraft as horizontal vorticity associated with low level environmental air is tilted toward the vertical. Then as the flow passes through the updraft, the vertical vorticity produced is amplified by the convergence mechanism to create the low level mesocyclone. In early stages, mesocyclone vorticity increases with height to middle storm levels where vorticity is produced primarily by the twisting of horizontal vorticity.

A sudden intensification of mesocyclone rotation, particularly at low levels, heralds the tornadic stage and transforms the mesocyclone. Significant twisting term vorticity production at this stage appears to involve locally generated horizontal vorticity associated with air that has cycled about the mesocyclone and with air that has descended on the storm's rear. Updrafts and rainy downdrafts are strong at this critical stage and interact to locally increase convergence. Low level vorticity amplification by the convergence mechanism surges, exceeding twisting

term generation by a factor of 2 or more. Tornadoes feed upon low level air which passes through the region of strong convergence term amplification and are most likely triggered by that vorticity production.

The dependence on vorticity causes the low level pressure deficit associated with the mesocyclone to deepen during intensification. Upward perturbation pressure gradients in vicinity of the mesocyclone are reduced and can be reversed by the build-up of low level vorticity. The sudden formation of concentrated rear downdrafts commonly observed in tornadic thunderstorms results from the vertical pressure gradient reversal.

Mesocyclone intensification may also precipitate storm decline. The reduction in the vertical perturbation pressure gradient decreases the storm's ability to lift negatively buoyant air at the base of updrafts. Further, downdraft formation results in a flux of air parcels into the mesocyclone from higher levels on the storm's rear. This air is potentially cold and when mixed with updraft air reduces buoyancy in middle storm levels. In final stages, updrafts weaken and downdrafts fill the mesocyclone. Vertical vorticity rapidly dissipates toward ground via the convergence term and the association between the updraft and the mesocyclone ends.

LIST OF SYMBOLS AND NOTATION

A,B,C,D	Geometric-radial velocity terms used in computation of Cartesian components of velocity
a	a constant (0.61)
c_p	specific heat of dry air at constant pressure (1.004×10^3 $m^2\ s^{-2}\ °C^{-1}$)
D	notation representing $\vec{\nabla} \cdot \vec{V}$
Def	deformation
E	turbulent kinetic energy [$= \frac{1}{2} \sum_{i=1}^{3} u_i' u_i'$]
e^2	sum of squares of the rates of strain [$=e_{ij}e_{ij}=e_{ji}e_{ji}$]
e_{ij}	rate of strain tensor [$= \frac{1}{2} (\frac{\partial u_i}{\partial x_j} + \frac{\partial u_j}{\partial x_i})$]
F	turbulent diffusion vector [$=F_x\vec{i} + F_y\vec{j} + F_z\vec{k}$]
f	fractional distance of point (x) between grid locations x_i and x_{i+1} [$=(x-x_i)/(x_{i+1}-x_i)$]
g	acceleration of gravity (9.8 m s^{-2})
h	weighting factor
i,j	velocity (u_i,u_j=u,v,w) and coordinate (x_i,x_j=x,y,z) indices; grid numbering index (x_i,x_{i+1},x_{i+2},x_{i-1})
$\vec{i},\vec{j},\vec{k}$	unit vectors directed eastward, northward and upward respectively
j_o	spherical Bessel function of zero order
K	wave number [$= \frac{2\pi}{\lambda}$]
K_m	momentum eddy diffusion coefficient

p	dimensional pressure (mb)
q_c	condensate mixing ratio
q_v	water vapor mixing ratio
R	radar slant range
R_d	gas constant for dry air (2.87×10^2 m^2 s^{-2} $°C^{-1}$)
r	three-dimensional distance between a radar observation and a grid point
r_*	radius of influence
t	time
u,v,w	magnitudes of the eastward, northward and vertical wind components respectively
$\vec{V}$	three-dimensional wind velocity [$= u\vec{i} + v\vec{j} + w\vec{k}$]
V_r	radial velocity as measured by radar
V_t	hydrometeor terminal velocity
x,y,z	Cartesian coordinates increasing eastward, northward and upward respectively
Z	radar reflectivity factor
Δ	grid interval parameter [$=(\Delta x \Delta y \Delta z)^{1/3}$]
$\Delta x, \Delta y, \Delta z$	grid spacing in eastward, northward and vertical directions respectively
δ_{ij}	Kronecker delta
θ	potential temperature; spherical angle
θ_v	virtual potential temperature [$= \theta(1+aq_v)$]
λ	wavelength
ν	weight parameter (0.54 km^2)
π	non-dimensional pressure; mathematical constant (=3.14159)
ρ	air density

σ	response function
ϕ	interpolated grid point value; spherical angle
ψ	radar measurement
$\vec{\omega}$	three-dimensional vorticity [$=\xi\vec{i} + \eta\vec{j} + \zeta\vec{k}$]
∞	infinity
$\vec{\nabla}$	three-dimensional del operator [$= \vec{i}\frac{\partial}{\partial x} + \vec{j}\frac{\partial}{\partial y} + \vec{k}\frac{\partial}{\partial z}$]
∇^2	three-dimensional Laplacian operator [$= \frac{\partial^2}{\partial x^2} + \frac{\partial^2}{\partial y^2} + \frac{\partial^2}{\partial z^2}$]
∇_H^2	two-dimensional Laplacian operator [$= \frac{\partial^2}{\partial x^2} + \frac{\partial^2}{\partial y^2}$]
$(\ )'$	perturbation (deviation) of quantity from mean
$(\ )_o$	base state value at height z
$(\ )_{oo}$	base state value at z=0

I. INTRODUCTION

Tornadoes form within larger scale thunderstorm circulations that have strong rotary winds and reduced pressure. These parental circulations (mesocyclones), first identified by Brooks (1949), typically have horizontal dimensions of ~5 km; whereas tornadoes are generally several hundred meters wide. The closeness of the relationship between tornadoes and mesocyclones is illustrated, for example, by the pilot radar study of Burgess (1976) who found that 62% of Oklahoma thunderstorms with mesocyclones produced tornadoes and that no tornadoes occurred without mesocyclones. Moreover, mesocyclones often precede tornadoes by tens of minutes and are readily detected by radar. Hence, the mesocyclone is of considerable interest.[1]

Generally the source of thunderstorm rotation is attributed to either the convergence or the twisting terms of the vertical vorticity tendency equation. Conceptual models based on convergence require a background of vertical vorticity, often concentrated at a wind discontinuity, and updraft to further concentrate the vorticity (e.g., Bates, 1962; Fujita, 1965). However, the preponderant evidence suggests that tilting of low level environmental wind shear (horizontal vorticity) by updraft is the ultimate source of thunderstorm rotation. Indeed, strong

---

[1] A few small tornadoes have occurred in which a background vertical vorticity has not been detected by radar. Documentation of these situations is awaited.

environmental wind shear is an integral part of the Browning (1964) severe thunderstorm model and its possible role as the source of updraft rotation was recognized (Browning, 1968). Further, the motion of the storm updraft relative to the boundary layer shear dictates the sign of the vertical vorticity produced (Barnes, 1970).

That storm mesocyclone vorticity is determined by horizontal vorticity is primarily supported by numerical simulations of severe thunderstorms in environs free of vertical vorticity but having vertical wind shear (Schlesinger, 1975 and 1978; Klemp and Wilhelmson, 1978a; Wilhelmson and Klemp, 1978). The initial vertical vorticity generation in modeled storms occurs at middle storm levels and is dominated by updraft tilting of base state horizontal vorticity. Later, as rainy downdrafts intensify and strong convergence develops at low level gust fronts, vorticity generation is dominated by the convergence of tilted vertical vorticity. The magnitude of the vertical vorticity production is augmented by horizontal vorticity created in inflow regions by buoyancy (Klemp and Rotunno, 1983).

Mesocyclone vorticity increases exponentially in modeled storms as small amounts of horizontal vorticity are added to the thunderstorm environment (Bleckman, 1981). Further, the vertical distribution of environmental wind shear strongly influences the configuration and the relative magnitudes of the cyclonic and anticyclonic circulations produced (see also, Klemp and Wilhelmson, 1978b).

Doppler radar observations indicate a well-defined storm metamorphosis accompanies tornadogenesis. Mesocyclone rotation increases, particularly in lower storm levels. Gust fronts separating subsiding rainy downdraft and inflow air accelerate forward, and attendant updraft and

vertical vorticity distributions become markedly perturbed (e.g., Brandes, 1981). Intense local downdrafts, entraining air directly from the storm's rear, suddenly form behind the gust front (e.g., Barnes, 1978a; Brandes, 1978; Lemon and Doswell, 1979). Rear downdrafts are widely thought to result either from evaporative cooling (Barnes, 1978a) or from dynamical interaction between the environmental wind and the storm (Lemon and Doswell, 1979). But recent numerical simulations (Klemp and Rotunno, 1983) suggest these downdrafts are induced by the intensification of vorticity near ground.

Represented as anomalous shear zones in the radar measurements (Burgess et al., 1975), tornadoes are usually first detected within elevated portions of the mesocyclone and lower to ground over a period of several tens of minutes. Tornadoes tend to be located within the vertical velocity gradient between the principal storm updraft and the concentrated rear downdraft.

Exactly what triggers tornadoes and how they acquire their intense vorticity is not known. Most theories extend mechanisms invoked to explain the rotation of the tornado parental circulation or call upon interaction between various storm features, but more than one mechanism may be operating. Bates (1962) postulated tornadoes form by conservation of angular momentum when local convergence maxima along gust fronts are drawn into the main updraft. Similarly, Starr (1976) proposed tornadoes begin as eddies within mesocyclones which intensify when swept up in updrafts.

Ludlam (1963) suggested tornado spin originates with ambient horizontal vorticity being tilted by spreading outflow air from rainy downdraft

beneath storms. Alternately, Lemon and Doswell (1979) propose that tornadoes feed upon horizontal vorticity tilted by spreading rear downdraft air.

Twisting downdrafts, laden with precipitation, were considered by Fujita (1973) to impart their angular momentum to the low level mesocyclone and thereby trigger tornadoes. Similar roles for rear downdrafts have been proposed by Barnes (1978a) and Brandes (1978). Davies-Jones (1982) suggests a downward transport of vertical vorticity in the lowest few kilometers of rear downdrafts is necessary for tornadoes to complete their descent to ground.

It is has also been suggested that shearing instabilities along wind discontinuities and gust fronts could generate tornadoes (Ward, 1962; Barnes, 1978b; Brandes, 1977b). However, Barnes (1978b) supposes shearing instabilities produce only small tornadoes while large tornadoes, as indicated by laboratory experiments (Ward, 1972; Fitzjarrold, 1973), respond to critical relationships between the rotational and divergent components of mesocyclone flow.

Tornado flow patterns are not resolved in the radar measurements used in this study, but the flow of mesocyclones is readily reconstructed. Hence, the larger scale parental circulation, particularly the lowest 5 km, is examined and those properties favoring tornadogenesis are detailed. The radar data are incomplete observational records and are not without problems. Nevertheless, the composite data set seems to typify tornadic storms. Indeed, the data have been used previously by a number of investigators to study storm morphology and evolution; results are often cited in the literature. Specifically this research seeks to:

1) Document the distribution and generation of vorticity in tornadic thunderstorms.

2) Quantify the contributions of the various mechanisms that generate mesocyclone vorticity.

3) Combine thermodynamic information extracted from the radar derived wind fields with kinematic properties to clarify those severe storm processes which cause tornadoes.

For convenience, mesocyclones are defined as vertical vorticity maxima exceeding 10^{-2} s^{-1}. (Lower thresholds resulted in large elongated mesocyclones with multiple maxima while higher thresholds produced small mesocyclones having poor spatial and temporal continuity.) To facilitate comparison between the various mesocyclone evolutionary stages and between storms, the maximum vertical vorticity, the range in divergence, the mean divergence and the mean vertical vorticity production by convergence, twisting and turbulence at each analysis level are tabulated.

In theory, if the wind field and its behavior are known, the equations of motion can be manipulated to yield the thermodynamic variables.[2] Previously, Bonesteele and Lin (1978) have described a computation scheme in which the horizontal temperature distribution is specified and horizontal pressure perturbations are found by solving a two-dimensional elliptic equation. Leise (1978) derived a buoyancy equation by cross-differentiating the equations of motion to yield density deviations and ultimately the pressure and temperature fields. With his approach the density distribution at ground needs to be specified. An iterative method involving a two-dimensional elliptic equation for pressure in a vertical cross-section and the third equation of motion for virtual

---

[2]The procedure is often referred to as "thermodynamic retrieval" or simply "retrieval" after Hane and Scott (1978).

temperature was proposed by Hane and Scott (1978). Gal-Chen (1978) described a noniterative scheme with a horizontal pressure equation and an averaged form of the third equation of motion to find density variations.

Gal-Chen's technique was modified by Hane et al. (1981) to yield pressure and buoyancy fluctuations. A unique pressure-temperature solution, not routinely available when Neumann boundary conditions are used to solve for pressure, is found in terms of perturbations by removing the mean pressure at each analysis level and then calculating buoyancy deviations from a form of the third equation of motion in which the mean of each term has been subtracted. By repeating this procedure at each level, a three-dimensional coupling of the thermodynamic variables is ensured.

This investigation begins with a scale analysis of the various mechanisms that produce vertical vorticity in severe thunderstorms (Chapter II). A different methodology is then described for estimating thermodynamic variables in storm flow fields reconstructed from Doppler radar observations. A two-dimensional elliptic equation, independent of pressure, is derived that yields perturbation potential temperatures. The temperatures become input to a three-dimensional elliptic equation yielding perturbation pressures. Radar data handling procedures, error sources in the wind fields and computational considerations are discussed (Chapter III). The evolution and generation of vertical vorticity is documented with observations from three tornadic storms (Chapter IV). When data quality warrants, thermodynamic information extracted from the observed wind fields is incorporated into the discussion. Observed

thermodynamic properties are compared to recent numerical simulations of the tornadic region in severe thunderstorms (Chapter V). Principal findings of this research are summarized in Chapter VI.

II. THE GOVERNING EQUATIONS

A. Vorticity Equation

The equations used in this study are of the "anelastic" form derived by Ogura and Phillips (1962) for deep convection and are based on the assumption that the percent variation in potential temperature is small compared to the potential temperature itself. A modification (e.g., Wilhelmson and Ogura, 1972) allows the inclusion of a potential temperature base state that varies with height.

The momentum equations (ignoring earth's rotation) are written

$$\frac{d\vec{V}}{dt} = -c_p\theta_{vo}\vec{\nabla}\pi' + \vec{F} + \vec{k}g\left(\frac{\theta'}{\theta_o} + aq_v'-q_c\right) \qquad (1)$$

where $\vec{V}$ is the velocity vector, $\vec{F}$ represents subgrid turbulent forces, θ is potential temperature, θ_v is the virtual potential temperature, π is the non-dimensional pressure, q_v and q_c are the mixing ratios of water vapor and condensate, c_p is the specific heat capacity of air at constant pressure, g is the acceleration of gravity and a = 0.61.[3] Zero subscripted variables refer to the base state (environment) and prime

[3]The ratio between tornadic storm relative vorticity and the Coriolis force is ~100. Consequently the Coriolis force is neglected in this diagnostic study. In a time integration model, however, the accumulated effect of this force can be significant (e.g., see Fig. 8 of Klemp and Wilhlemson, 1978b).

terms are perturbations thereof. The actual pressure, water vapor mixing ratio, and potential temperature are defined

$$\pi(x,y,z) = \pi_0(z) + \pi'(x,y,z)$$
$$q_v(x,y,z) = q_{vo}(z) + q_v'(x,y,z)$$
$$\theta(x,y,z) = \theta_0(z) + \theta'(x,y,z) \quad .$$

Velocity and friction vectors have the component forms

$$\vec{V} = u\vec{i} + v\vec{j} + w\vec{k}$$
$$\vec{F} = F_x\vec{i} + F_y\vec{j} + F_z\vec{k} \quad .$$

The orthogonal wind components u, v and w correspond to the x(east), y(north) and z(vertical) directions. The system of equations also includes the anelastic continuity equation

$$\vec{\nabla}\cdot\rho_0\vec{V} = 0 \qquad (2)$$

where $\rho_0=\rho_0(z)$ is the air density and the hydrostatic equation for the environment

$$\frac{\partial\pi_0}{\partial z} = -\frac{g}{c_p\theta_0} \quad . \qquad (3)$$

Cross-differentiation of the momentum equations yields the three-dimensional vorticity tendency equation

$$\frac{d\vec{\omega}}{dt} = (\vec{\omega}\cdot\vec{\nabla})\vec{V} - (\vec{\nabla}\cdot\vec{V})\vec{\omega} - c_p\vec{\nabla}\theta_{vo}x\vec{\nabla}\pi' + \vec{\nabla}x[\vec{k}g(\frac{\theta'}{\theta_o} + aq_v' - q_c)] + \vec{\nabla}x\vec{F} \qquad (4)$$

where $\vec{\omega}[\equiv\vec{\nabla}x\vec{V}]$ has the component form

$$\vec{\omega} = \xi\vec{i} + \eta\vec{j} + \zeta\vec{k}$$

and the rotations about the x, y and z axes are

$$\xi = \frac{\partial w}{\partial y} - \frac{\partial v}{\partial z}$$

$$\eta = \frac{\partial u}{\partial z} - \frac{\partial w}{\partial x}$$

$$\zeta = \frac{\partial v}{\partial x} - \frac{\partial u}{\partial y} \quad .$$

Because mesocyclones are often nearly vertical with height (a median departure of 18° in this study) and because tornadoes form within regions of strong vertical vorticity, the vertical vorticity tendency following air parcel motion is desired and Eq. (4) is dot multiplied by $\vec{k}$ to obtain

$$\frac{d\zeta}{dt} = (\frac{\partial w}{\partial y}\frac{\partial u}{\partial z} - \frac{\partial w}{\partial x}\frac{\partial v}{\partial z}) - \zeta(\frac{\partial u}{\partial x} + \frac{\partial v}{\partial y}) + (\frac{\partial F_y}{\partial x} - \frac{\partial F_x}{\partial y}) \quad . \qquad (5)$$

Turbulent forces have been parameterized using Schlesinger's (1978) anelastic adaptation of the Deardorff (1970) scheme for incompressible flow (see Appendix A). The turbulent diffusion of vorticity $\frac{\partial F_y}{\partial x} - \frac{\partial F_x}{\partial y}$ is primarily proportional to $\nabla^2\zeta$ and consequently reduces concentrations of vorticity. Production was roughly 15% of that due to advection in

Schlesinger's simulation of severe thunderstorms. Because the term is small and because the distribution of turbulent vorticity diffusion can be deduced from the vertical vorticity, turbulent effects in this report will be presented with little or no comment.

The effect of surface friction has been ignored altogether. Deceleration of flow near ground by surface friction generates horizontal vorticity which may diffuse upward. However, except near ground, viscous stresses should be much smaller than eddy stresses associated with turbulent flow (Haltiner and Martin, 1957). Further, numerical experiments with tornado-like vortices show concentrated vortices form with or without the inclusion of surface friction (Rotunno, 1977); only the details of the vortex flow are changed.

It is widely agreed the remaining two forcing terms on the right hand side of (5) play dominant roles in vertical vorticity amplification. Radar studies (Ray, 1976; Heymsfield, 1978; Brandes, 1981) reveal vorticity amplification via horizontal convergence, i.e., by the concentration of existing vertical vorticity $-\zeta(\frac{\partial u}{\partial x} + \frac{\partial v}{\partial y})$, exceeds $6\text{x}10^{-5}$ s^{-2} and may approach $5\text{x}10^{-4}$ s^{-2} in the roots of severe storm updrafts.

The term $\frac{\partial w}{\partial y}\frac{\partial u}{\partial z} - \frac{\partial w}{\partial x}\frac{\partial v}{\partial z}$ represents the twisting of vertical wind shear by horizontal variations in the vertical wind. Alternately, this term can be expressed either as the tilting of the horizontal vorticity components by variations in the vertical wind $\xi\frac{\partial w}{\partial x} + \eta\frac{\partial w}{\partial y}$ or as products of shearing deformations and the horizontal vorticity components $\frac{1}{2}[\xi(\frac{\partial u}{\partial z} + \frac{\partial w}{\partial x}) + \eta(\frac{\partial v}{\partial z} + \frac{\partial w}{\partial y})]$. Davies-Jones (1982) points out that the shearing deformations (rates of strain) play the same role as horizontal convergence $\frac{\partial u}{\partial x} + \frac{\partial v}{\partial y}$ plays in the convergence term and that the convergence

and twisting terms both stretch and reorient vortex tubes. Not unexpectedly, the importance of the twisting mechanism increases away from ground and becomes large wherever strong horizontal gradients of the vertical wind and strong vertical wind shears coexist. Productivity is comparable to the convergence term.

The advective terms contained within the substantial derivative in Eq. (5), i.e., $u\frac{\partial \zeta}{\partial x}$, $v\frac{\partial \zeta}{\partial y}$ and $w\frac{\partial \zeta}{\partial z}$, have been evaluated in a ground relative coordinate system by Ray (1976) and found to be 4 times greater than the convergence and twisting terms. Here, in a storm relative coordinate system, the advective terms are nearly equivalent. While advection does not raise the vorticity above values which already exist in the domain, advection can be important for redistributing vorticity, e.g., extending the updraft mesocirculation to the storm anvil (Schlesinger, 1978).

Before concluding this section on the vorticity equation some discussion concerning baroclinicity is relevant. Horizontal solenoids are precluded in (5) by the anelastic assumption used in the derivation of the motion Eqns. (1). Although their scale analyses indicate otherwise, Heymsfield (1978) and Lemon and Doswell (1979) argue that horizontal solenoids could produce significant vertical vorticity wherever negatively buoyant middle level air interacts with updraft air. The paucity of pressure and temperature measurements within severe thunderstorms causes some uncertainty concerning the quantification of such effects. Based on aircraft measurements, Heymsfield estimates production rates to be $6\text{x}10^{-7}$ s^{-2} while Ray (1976) gives an upper limit of $4\text{x}10^{-6}$ s^{-2}.

The contribution to vertical vorticity by the neglected horizontal solenoids in (5) $c_p(\frac{\partial \theta'}{\partial x}\frac{\partial \pi'}{\partial y} - \frac{\partial \theta'}{\partial y}\frac{\partial \pi'}{\partial x})$ was estimated <u>a posteriori</u> from

retrieved thermodynamic fields (Chapter IV). Maximum values of 3.6×10^{-6} s^{-2} were roughly two orders of magnitude less than the largest forcing terms in Eq. (5).

In summary, vertical vorticity production in thunderstorms is largely by the convergence of vertical vorticity and by the twisting of the horizontal vorticity components. Turbulent diffusion of vorticity is almost an order of magnitude less. From the current observational evidence, it would seem neglected solenoidal effects are two orders of magnitude smaller than the largest forcing terms.

B. Computation of Pressure and Potential Temperature Perturbations

For this study, the three-dimensional elliptical equation (see Appendix B)

$$\nabla^2 \pi' + \frac{\partial \ell n(\rho_o \theta_{vo})}{\partial z} \frac{\partial \pi'}{\partial z} = \frac{1}{c_p \theta_{vo}} \left\{ - \frac{1}{\rho_o} \vec{\nabla} \cdot \rho_o (\vec{V} \cdot \vec{\nabla}) \vec{V} + \frac{g \partial}{\rho_o \partial z} \left[\rho_o \left(\frac{\theta'}{\theta_o} + a q_v' - q_c \right) \right] + \frac{1}{\rho_o} \vec{\nabla} \cdot \rho_o \vec{F} \right\} \tag{6}$$

is used to compute pressure perturbations. Imposed Neumann lateral boundary conditions are

$$\frac{\partial \pi'}{\partial x} = \frac{1}{c_p \theta_{vo}} \left[- \vec{V} \cdot \vec{\nabla} u - \frac{\partial u}{\partial t} + F_x \right]$$

$$\frac{\partial \pi'}{\partial y} = \frac{1}{c_p \theta_{vo}} \left[- \vec{V} \cdot \vec{\nabla} v - \frac{\partial v}{\partial t} + F_y \right] \quad .$$

Additionally, we require

$$w = \frac{\partial w}{\partial x} = \frac{\partial w}{\partial y} = \frac{\partial u}{\partial z} = \frac{\partial v}{\partial z} = 0$$

$$\frac{\partial \pi'}{\partial z} = \frac{1}{c_p \theta_{vo}} \left[g\left(\frac{\theta'}{\theta_o} + a q_v' - q_c\right) + F_z \right]$$

at the lower and the upper boundaries, respectively. Whenever the data did not extend to storm top,

$$\frac{\partial \pi'}{\partial z} = \frac{1}{c_p \theta_{vo}} \left[-\vec{V} \cdot \vec{\nabla} w - \frac{\partial w}{\partial t} + g\left(\frac{\theta'}{\theta_o} + a q_v' - q_c\right) + F_z \right]$$

was substituted as an upper boundary condition.

Solutions to Eq. (6), found by relaxation, are not unique and are known only to within a constant. Unlike the two-dimensional approach (e.g., Hane et al., 1981), time derivatives do not explicitly appear in (6) but pressure depends upon q_v' and q_c, which must be parameterized, and on temperature. However, perturbation pressures obtained are readily differentiable in the vertical.

Temperature could be computed with the third equation of motion, but the pressure dependence in (1) would necessitate an iterative solution with (6). By cross-differentiating the equations of motion twice and dot multiplying the result with $\vec{k}$ an elliptic equation giving the perturbation potential temperature in a horizontal plane (see Appendix B)

$$\nabla_H^2 \theta' = - \frac{\theta_o}{g} \left\{ \vec{k} \cdot \vec{\nabla} \times \vec{\nabla} \times \left[\frac{d\vec{V}}{dt} + c_p \theta_{vo} \vec{\nabla} \pi' - \vec{F} - \vec{k} g (a q_v' - q_c) \right] \right\} \qquad (7)$$

is obtained. Temperature solutions depend on the pressure terms $c_p \frac{\partial \theta_{vo}}{\partial z} \frac{\partial^2 \pi'}{\partial x^2}$ and $c_p \frac{\partial \theta_{vo}}{\partial z} \frac{\partial^2 \pi'}{\partial y^2}$. Empirically, these terms are at most of order 0.06 °C km^{-2} while the velocity terms approach 4°C km^{-2}.[4] Ignoring the pressure contribution, the temperature equation reduces to

$$\nabla_H^2 \theta' = -\frac{\theta_o}{g} \left\{ \vec{k} \cdot \vec{\nabla} \times \vec{\nabla} \times \left[\frac{d\vec{V}}{dt} - \vec{F} - \vec{k} g (a q_v' - q_c) \right] \right\} \qquad (8)$$

and temperature can be determined in situations where pressure is not known or desired.

Thus, Eq. (8) can be solved for temperature and results substituted into (6) for pressure. The methodology is analogous to Hane et al. where the pressure retrieval is independent of buoyancy and the perturbation pressures are input to the third equation of motion for buoyancy.

To obtain the true perturbations necessary for the solution of (6) and to preserve the dependence from pressure, Eq. (8) was solved (by relaxation) with the boundary condition $\theta' = 0$. This condition suits storms well contained within the analysis grid and is consistent with the assumption of a horizontally homogeneous environment. However, this condition is inappropriate at boundaries--as occasionally was the case here with limited computer storage--where strong forcing extends outside the computation grid. Boundary induced errors in such regions were mitigated by extrapolating the temperature solution outward with $\frac{\partial \theta'}{\partial x_i} = 0$ and then solving (8) a second time using the extrapolated temperatures as a boundary condition. This procedure was for cosmetic purposes and had

---

[4] Similar terms have already been found to be negligible in comparison to the dynamical forcing terms of the vorticity tendency equation.

very little effect on the retrieved temperature fields except in those fringe areas with strong forcing. Further, subsequent investigation of the retrieved thermodynamic fields was restricted to an interior subgrid of the actual data domain; the outer grid point values of temperature and pressure are not used.

Equations (6) and (8) have forms better suited for this tornadogenesis study. Following Bradshaw and Koh (1981), the dynamical forcing in (6) is partitioned among the square of the rate of strain and the square of the vorticity (Appendix B)

$$\nabla^2\pi' + \frac{\partial \ell n(\rho_o \theta_{vo})}{\partial z}\frac{\partial \pi'}{\partial z} = \frac{1}{c_p \theta_{vo}}\left\{-e^2 + \frac{1}{2}(\xi^2+\eta^2+\zeta^2) + w^2\frac{\partial^2 \ell n \rho_o}{\partial z^2}\right.$$

$$\left. + \frac{g}{\rho_o}\frac{\partial}{\partial z}\left[\rho_o\left(\frac{\theta'}{\theta_o} + aq_v' - q_c\right)\right] + \frac{1}{\rho_o}\vec{\nabla}\cdot\rho_o\vec{F}\right\} \qquad (9)$$

where $e^2 = e_{ij}e_{ij} = e_{ji}e_{ji}$, the rate of strain $e_{ij} = \frac{1}{2}\left(\frac{\partial u_i}{\partial x_j} + \frac{\partial u_j}{\partial x_i}\right)$, u_i, u_j = u,v,w and x_i, x_j = x,y,z. Experience shows the forcing for pressure is largely determined by strain rate and vorticity and somewhat less by temperature buoyancy. Because the solution for pressure is related to the negative of the forcing, strong vorticity associates with low pressure and saddle points in the wind field associate with high pressure. For display, π' is converted to dimensional pressure p' (mb) using

$$p' = P_{oo}[\pi_o + \pi']^{c_p/R_d} - p_o \qquad (10)$$

where P_{oo} is the base state pressure $p_o(z)$ at z=0 and R_d is the gas constant for dry air. Because pressure solutions are not unique, comparisons between analyses are properly based on pressure gradients.

The diagnostic equation for potential temperature (8) can be written (Appendix B)

$$\nabla_H^2\theta' = -\frac{\theta_o}{g}\left\{\vec{K}\cdot\vec{\nabla}\times\left[\frac{d\vec{\omega}}{dt} - (\vec{\omega}\cdot\vec{\nabla})\vec{V} + (\vec{\nabla}\cdot\vec{V})\vec{\omega}\right]\right.$$

$$\left. - \vec{K}\cdot\vec{\nabla}\times\vec{\nabla}\left[\vec{F} + \vec{K}g(aq_v'-q_c)\right]\right\} \qquad (11)$$

which in scalar form becomes

$$\nabla_H^2\theta' = \frac{\theta_o}{g}\left\{\frac{\partial}{\partial y}\left[\frac{d\xi}{dt} + \left(\frac{\partial v}{\partial y} + \frac{\partial w}{\partial z}\right)\xi - \eta\frac{\partial u}{\partial y} - \zeta\frac{\partial u}{\partial z}\right]\right.$$

$$- \frac{\partial}{\partial x}\left[\frac{d\eta}{dt} + \left(\frac{\partial u}{\partial x} + \frac{\partial w}{\partial z}\right)\eta - \xi\frac{\partial v}{\partial x} - \zeta\frac{\partial v}{\partial z}\right]$$

$$\left. - \nabla_H^2\left[g(aq_v'-q_c) - F_z\right] + \frac{\partial}{\partial z}\left[\frac{\partial F_x}{\partial x} + \frac{\partial F_y}{\partial y}\right]\right\} . \qquad (12)$$

Herein, the temperature distribution in horizontal planes is largely influenced by dynamical and vortical factors which determine the projection of the three-dimensional temperature gradient vector. Inspection of Eqns. (6) and (8) reveals that the forcing for temperature involves one or more derivative than the forcing for pressure. A greater "noise level" is expected a priori in the retrieved temperature fields; and consequently, temperature results are viewed as being qualitative in nature.

III. DATA

A. Radar Data Synthesis and Errors in Derived Wind Fields

The basic data are coordinated volumetric samples of radial velocity and radar reflectivity from Doppler radars located near Norman and Yukon, Oklahoma. Measurements were spaced at 1° azimuthal, 1 or 2° elevation and 0.15 or 0.6 km radial intervals. Individual data collections were ~5 min in duration and usually terminated before storm top.

Measurements were projected to common three-dimensional Cartesian grids (0.8 km horizontal and 0.5 km vertical spacing) with a single pass of a Gaussian weight function (Barnes, 1964). Observations ψ_i were weighted (filtered) according to

$$h(r) = \exp[-r^2/\nu]$$

where r is the three-dimensional distance between an observation and a grid point and ν is a filtering parameter experimentally selected to be 0.54 km^2. In practice the weighting of observations is restricted to a prespecified volume. Here the influence region was spherical and had a radius r_* of 1.5 km. Weights varied from 1.0 for observations coincident with grid locations to 0.02 for observations at the periphery of the influence region. Interpolated grid point estimates ϕ are determined from

$$\phi = \frac{\sum_{i=1}^{n} h\psi_i}{\sum_{i=1}^{n} h}$$

where n is the number of observations within the influence region. The response function for a finite influence radius (see Appendix C) is

$$\sigma = \frac{2\lambda}{\pi\sqrt{\pi}\nu^{3/2}} \int_0^{r_*} re^{-r^2/\nu} \sin \frac{2\pi r}{\lambda} \, dr$$

where λ is the wavelength of meteorological features in the data. The response function for $r_* = 1.5$ km and $\nu = 0.54$ km^2 is plotted in Fig. 1; the amplitude of a 5 km wave is reduced to ~80% of its original size by the interpolation procedure.

During lengthy data collections, storms may move several kilometers; consequently, prior to interpolation, measurement locations were adjusted for mean storm motion to a common reference time. No correction was applied for the differential motion of smaller storm elements or changes in storm intensity.

Typically, radial velocity measurement errors are ~1 m s^{-1}, but bias errors >3 m s^{-1} are possible in areas of low signal intensity. Because grid point estimates involve linear combinations of individual measurements, the error of interpolated velocities is essentially that of the input measurements. However, poor spatial sampling of small scale meteorological wavelengths in the vicinity of grid points and contamination of measurements by non-meteorological features can increase the

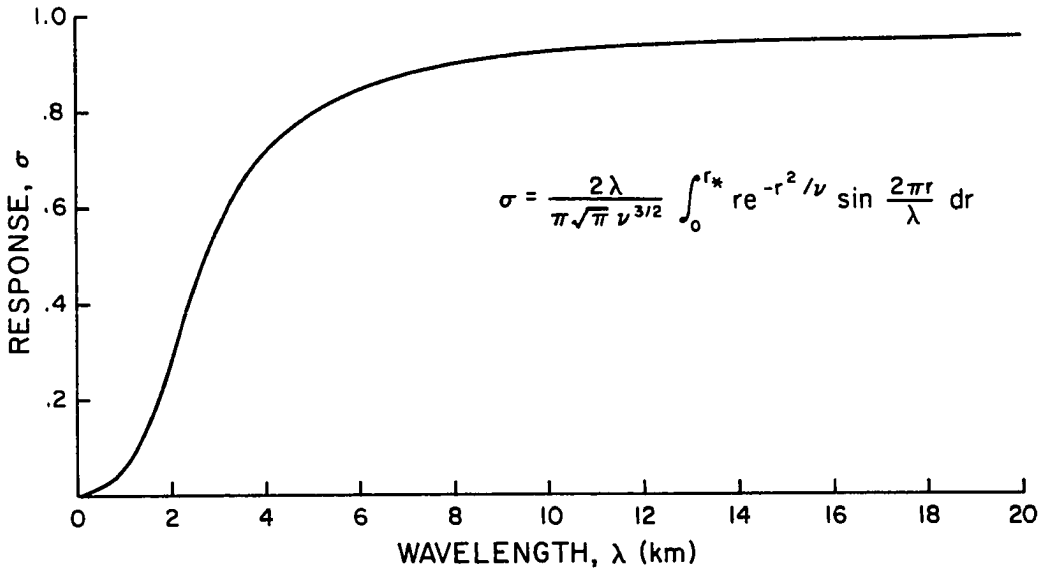

Figure 1. Response function for a truncated Gaussian weight function with ν=0.54 km^2 and r_*=1.5 km.

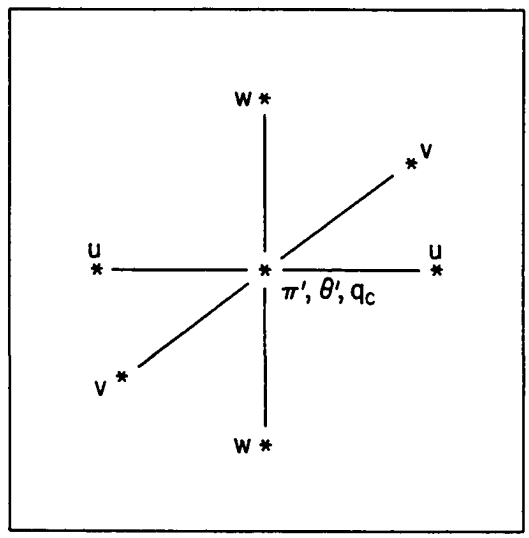

Figure 2. Three-dimensional staggered grid stencil.

error. Heymsfield (1978) experimentally determined that the standard error of interpolated velocities was ~2 m s^{-1}.[5]

Three-dimensional wind fields were constructed from the interpolated radial velocity estimates using methodology described by Brandes (1977a and 1978). Radial velocities V_r are related to Cartesian wind components by

$$V_{r1} = [x_1 u + y_1 v + z(w + V_t)] / R_1 \tag{13a}$$

$$V_{r2} = [x_2 u + y_2 v + z(w + V_t)] / R_2 \tag{13b}$$

where the numerical subscripts denote the radars, the radar slant range $R = \sqrt{x^2+y^2+z^2}$ and V_t is the hydrometeor terminal velocity. The latter is estimated by combining Rodger's (1964) formula $V_t = -3.8\ Z^{1/14}$, where Z is the radar reflectivity, with the Foote and du Toit (1969) density-height correction $(\frac{\rho_{00}}{\rho_0(z)})^{0.4}$. Equations (13a) and (13b) are solved for u and v and written

$$u = Aw + B \tag{14a}$$

$$v = Cw + D \tag{14b}$$

where A, B, C, and D involve known parameters. The vertical wind component is determined by integrating the continuity Eq. (2) and iterating

---

[5]Such an error would create a random error in vorticity and divergence of ~80×10^{-4} s^{-1}. Worst case situations here (late stages in the Harrah storm, Chapter IV) suggest the "noise level" in the computed vorticity fields is at most 50×10^{-4} s^{-1} and in general about 25×10^{-4} s^{-1}.

with (14). Because data collection did not routinely extend to storm top, the vertical wind component was computed by integrating the continuity equation upward from ground. Whenever observations were missing at ground but available at higher levels, e.g., in inflow regions on the storm's right flank, the vertical wind was not computed but the horizontal flow was estimated from the dominant terms B and D in (14).

During synthesis of three-dimensional wind fields, errors in the interpolated velocities are amplified by geometric factors that relate to the location of the radars (e.g., Lhermitte and Miller, 1970). Errors tend to accumulate (particularly in w) and because of atmospheric compressibility grow with height. The coupling of u and v with w causes horizontal wind field errors that are approximately equal to the product of the sine of the radar elevation angle and vertical wind error. A bias in computed divergence of $25\text{-}50 \times 10^{-4}$ s^{-1} could create updraft errors >12-25 m s^{-1} by 5 km elevation with such a computation scheme. Tests in which the mean storm motion vector was varied indicate vertical velocities of storm elements not moving with the mean vector could be in error by an additional 5 m s^{-1}.

Dependence on w and its gradients makes retrieved temperatures sensitive to the accumulated error. Near strong vertical drafts, temperature is principally determined by

$$\theta' = \frac{\theta_o}{g} \left(\frac{\partial w}{\partial t} + u \frac{\partial w}{\partial x} + v \frac{\partial w}{\partial y} + w \frac{\partial w}{\partial z}\right)$$

and errors are roughly proportional to the error in w, i.e., a factor of two error in updraft velocity causes a similar error in temperature.

Pressure has strong dependence on all three wind components and is less affected. In the absence of compensating effects, pressure can be contaminated through its temperature dependency; an error of 3°C corresponds to vertical pressure gradient of ~1 mb km^{-1}. Kinematic variables most affected by wind field error are the horizontal vorticity and tilting term vertical vorticity production.

B. Data Processing: Thermodynamic Retrieval

1. Filling of Data Voids and Transformation to a Staggered Grid

For convenience, data voids in the observed wind and radar reflectivity fields were filled and the data transferred to a staggered grid (Fig. 2) prior to thermodynamic retrieval. The grid filling procedure was designed to create minimal forcing in areas without data. Small data voids were filled by simple extrapolation from surrounding data areas by setting first derivatives to zero. Where more than one estimate was possible, estimates were averaged.

Large data voids, outside the data boundary but within the analysis grid, were filled by merging extrapolated values with the base state. Extrapolated values were weighted according to the Cressman (1957) weight function

$$h(r) = \frac{r_*^2 - r^2}{r_*^2 + r^2}$$

where r is the horizontal distance between the grid point to be filled and the nearest grid point with data and r_* is an arbitrarily specified radius of influence taken to be roughly one half the storm width (10 km).

When the nearest data point lay outside the influence region ($r>r_*$), h was set to zero. Selection of the weight function is arbitrary and based on the fact that this function gives a near linear combination of extrapolated and base state values over a wide range of distances. Modified grid point estimates ϕ were computed from

$$\phi = \phi_0(1-h) + \phi_e h$$

where ϕ_0 is the base state value and ϕ_e is the estimate produced by simple extrapolation. The three-point Shuman (1956) filter

$$\bar{\phi}_i = \phi_i + \frac{1}{4}(\phi_{i-1}-2\phi_i+\phi_{i+1}) \quad ,$$

where i in this usage is a grid index number, was then applied (once) in the x and y directions to smooth the resulting u and v fields. This filter has the response

$$\sigma = 1.0 - \frac{1}{2}(1.0-\cos\frac{2\pi\Delta x}{\lambda})$$

where Δx is the grid spacing. The amplitude of a 5 km wave is reduced to 77% of its original size by this operation (Fig. 3).

The horizontal wind components and radar reflectivity were then interpolated in three dimensions to the staggered grid using the highest possible ordered formula of

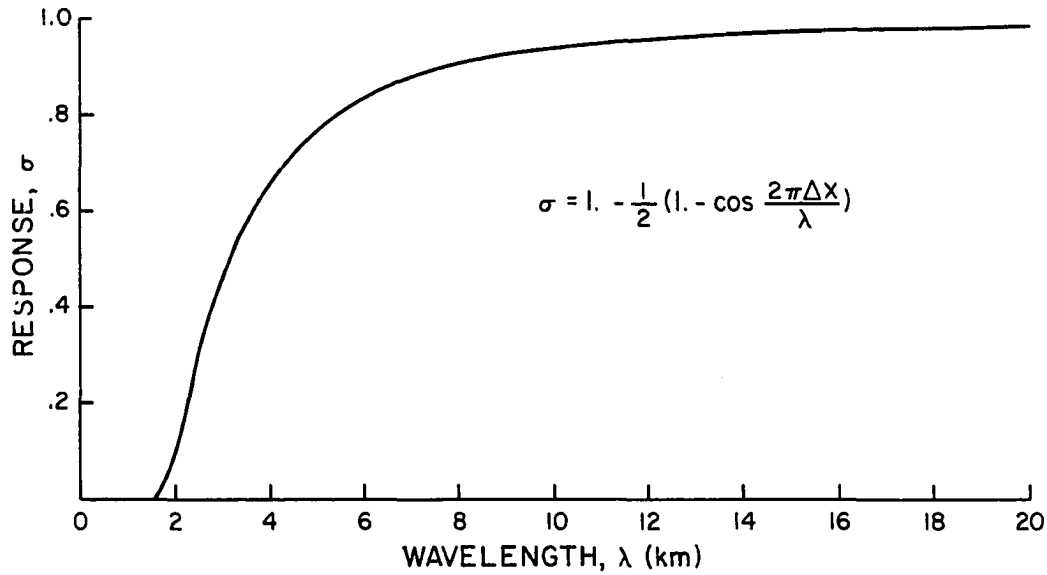

Figure 3. Response of the three-point Shuman (1956) filter with a smoothing element of 1/2.

$$\phi(x_i + f\Delta x) = \phi_i + f(\phi_{i+1}-\phi_i) \qquad (15a)$$

$$\phi(x_i+f\Delta x) = \phi_i + f(\phi_{i+1}-\phi_i) + f(f-1)(\phi_{i-1}+\phi_{i+2}-\phi_i-\phi_{i+1}) \qquad (15b)$$

where f is the fractional distance of the interpolated point between grid locations x_i and x_{i+1}. The continuity Eq. (2) was then reintegrated to ensure that the vertical wind component remained consistent with the horizontal wind fields.

2. Base State, Computation of Condensate Mixing Ratio and Neglect of Water Vapor Perturbations

All base state parameters were taken from environmental soundings. Condensate mixing ratios (assumed liquid) were estimated from radar reflectivity with

$$q_c = \frac{3.91\times10^{-9}}{\rho_0} Z^{.55} \qquad \text{gm water gm}^{-1} \text{ air} \quad . \qquad (16)$$

This relationship, determined from observational data given by Marshall and Palmer (1948), equates a reflectivity of 60 dBZ with a mixing ratio of ~8×10^{-3} gm water gm^{-1} air. Because the radar is insensitive to the smallest cloud droplets, actual liquid water concentrations may be somewhat higher. Aircraft measurements of water concentrations in nonprecipitating cumulus clouds without radar echoes (e.g., Draginis, 1958) suggest the mixing ratio of the nondetectable droplets is probably less than 2×10^{-3} gm water gm^{-1} air (a temperature equivalent $\theta_0 q_c$ of ~0.6°C). When hail is present, radar reflectivity may be enhanced or attenuated; and

mixing ratios estimated with (16) may be in error. Corrections are not possible without detailed information concerning hail size, number concentration and water film thickness. However, storms described here produced little hail and errors are probably less than 40 dBZ (~0.2°C).

Water vapor perturbations are difficult to estimate and have been ignored. (Note neglect of this term causes retrieved temperature deviations to behave like virtual potential temperature deviations.) Maximum water vapor perturbations of 9×10^{-3} gm water gm^{-1} air are suggested by comparisons between moist adiabatic temperatures of lifted air parcels and observed dew point temperatures determined from environmental soundings (a temperature equivalent $\theta_0 a q_v'$ of ~1.7°C). However, experiments with numerically simulated thunderstorm data indicates neglect of the water vapor perturbations causes maximum errors of 0.5°C and typical errors of 0.1°C in retrieved potential temperature deviations. Test results showed the maximum effect on retrieved pressures was ~0.1 mb.

3. Computation of Time Derivatives

The long and irregular intervals between consecutive data collections made it necessary that time derivatives, required for temperature retrieval, be determined from uncentered differences. Cross-correlation functions between consecutive observations were calculated at 1 km vertical intervals for each of the three wind components and for reflectivity. Derivatives were computed after displacing (lagging) one analysis with respect to the other to obtain the best average fit for the four variables. In fringe areas without data overlap, time derivatives were simply extrapolated with first derivatives set to zero.

C. Trajectory Analysis

To elucidate storm flow properties, the interpolating algorithms (15) were combined with a predictor-corrector method to determine the history and destination of select air parcels. For these analyses the original unstaggered wind fields were used. Wind components from the lowest data level (0.3 km) were extrapolated to ground by setting the vertical derivatives of the horizontal wind components to zero and by linearly decreasing the absolute value of w to zero. Poor temporal resolution between observations dictated that the simplifying steady-state assumption be made. Hence, computed paths are in truth streamlines rather than trajectories. The utility of the indicated paths depends on the time lengths involved and the persistence of features from one analysis time to another.

D. Additional Remarks

Unfortunately there are no independent measurements to support the retrieved thermodynamic fields. Approximate incloud temperatures can be deduced from hypothetical adiabatic processes with an environmental sounding. For example, the lifting of air parcels gives an estimate of updraft temperatures.

Consistency between input observations and retrieved variables has been assured by the closed system of equations and by separate verification of the computer code. However, the observations, particularly the vertical wind and the time derivatives, may contain considerable error. An implausible temperature or pressure result is a manifestation of that error.

IV. OBSERVATIONS

A. The Del City-Edmond Storm of 20 May 1977

The Del City-Edmond storm was ideally positioned for Doppler radar analysis (Fig. 4) and measurements obtained were more dense than in other storms studied (1° in azimuth and elevation and 0.15 km in range). Estimated time derivatives, based on a 19 min period, are poor; but with that exception, the observations are thought to be the most reliable of those to be described. Previously, the data have been compared to simulated thunderstorms (Klemp et al., 1981) and have been examined for severe storm morphological structure (Brandes, 1981; Ray et al., 1981). Prominent storm features observed during tornadogenesis include a concentrated rear downdraft and arc-like vertical vorticity and updraft zones. Brandes (1981) speculated about the roles of twisting and convergence term vertical vorticity production. These relationships and the storm's thermodynamic properties are now examined in detail.

1. 1826 CST: Pretornadic Stage

Radar observations prior to tornadogenesis reveal a principal updraft and a developing mesocyclone located on the storm's rear (Figs. 5 and 6).[6]

---

[6] All times are Central Standard Time (CST) and all heights, unless otherwise indicated, are above ground level (AGL).

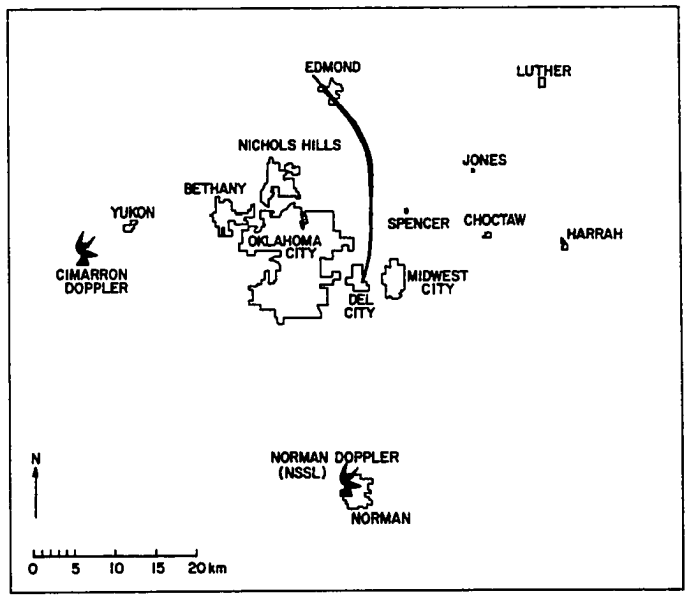

Figure 4. Map showing location of two Doppler radars and damage track of Del City-Edmond tornado, 20 May 1977.

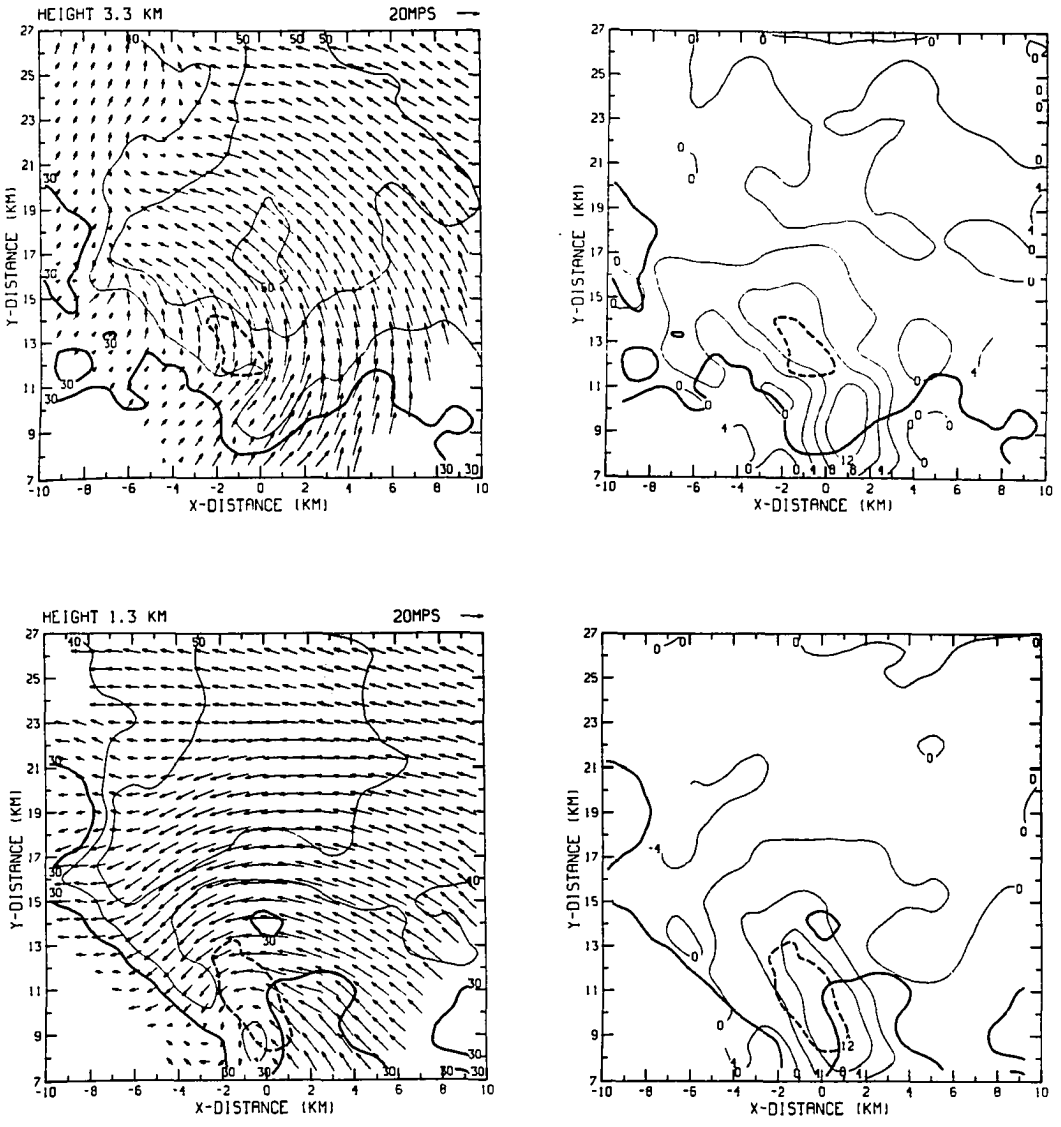

Figure 5. Wind fields in Del City-Edmond thunderstorm prior to tornadogenesis (1826 CST). Left hand panels show horizontal wind (vectors) relative to the storm [Cimarron radar reflectivity (dBZ) superimposed and 30 dBZ contour accentuated]. Right hand panels show vertical wind distribution ($m\ s^{-1}$) with the 30 dBZ reflectivity contour superimposed. Distances are from the Norman radar and heights (upper left) are AGL. A horizontal wind vector 1 km in length equals 20 $m\ s^{-1}$. Storm motion is from 200° at 17.5 $m\ s^{-1}$. Subsequent tornado damage, occurring between 1840 and 1912 CST, shown by stippling. The mesocyclone is indicated by a heavy dashed line. (z=1.3 and 3.3 km)

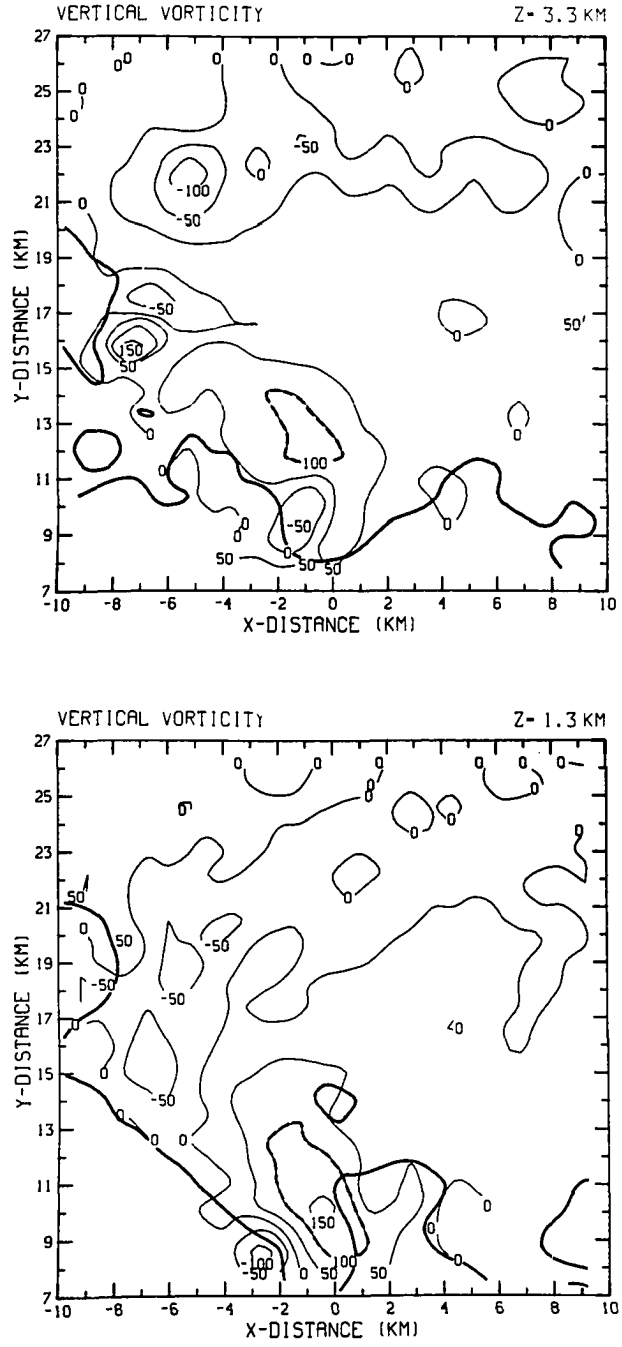

Figure 6. Vertical vorticity at 1.3 and 3.3 km elevation prior to tornadogenesis in the Del City-Edmond thunderstorm (1826 CST). Contouring interval is 50×10^{-4} s^{-1}. Heavy line denotes 30 dBZ radar reflectivity contour and heavy dashed line denotes the mesocyclone.

Both features are elongated in the southeast to northwest direction and slope north-northwestward with height. A rainy downdraft extends from the core of high radar reflectivity ≥50 dBZ southward along the storm's left flank. The subsiding flow converges with inflow air to form a gust front that continues southward outside the data domain. Single Doppler data, available at 6 to 8 min intervals, indicates the tornado later descended from the region of strong vertical vorticity near x=-1, y=12 km.

Weak positive vertical vorticity exists upwind (north through east) of the low level mesocyclone where inflow air turns cyclonically toward the mesocyclone and the updraft. On the storm's left flank, where storm flow recurves in the direction of the prevailing wind and in the rainy downdraft (x=-6, y=19 km), anticyclonic vertical vorticity predominates.

Horizontal vorticity is displayed vectorally ($\xi\vec{i} + \eta\vec{j}$) in Fig. 7 and the magnitude of the total (three-dimensional) vorticity is presented in Fig. 8. Inspection reveals total vorticity is primarily determined by the horizontal components. Strong horizontal vorticity exists throughout the inflow region. On the average, horizontal vorticity is about an order of magnitude larger than vertical vorticity found there; and maximum values $\sim 350 \times 10^{-4}$ s^{-1} are a factor of two larger than maximum mesocyclone vertical vorticity. Strong horizontal vorticity stems primarily from rapid wind veering with height. A storm relative hodograph from an atmospheric sounding (Fig. 9) shows a similar veering of the low level ambient wind. Curiously, inflow horizontal vorticity is about a factor of three larger than that of the ambient wind.

In the strong vertical wind gradient two to three kilometers upwind of the mesocyclone (e.g., x=2, y=10, z=1.3 km), horizontal vorticity is

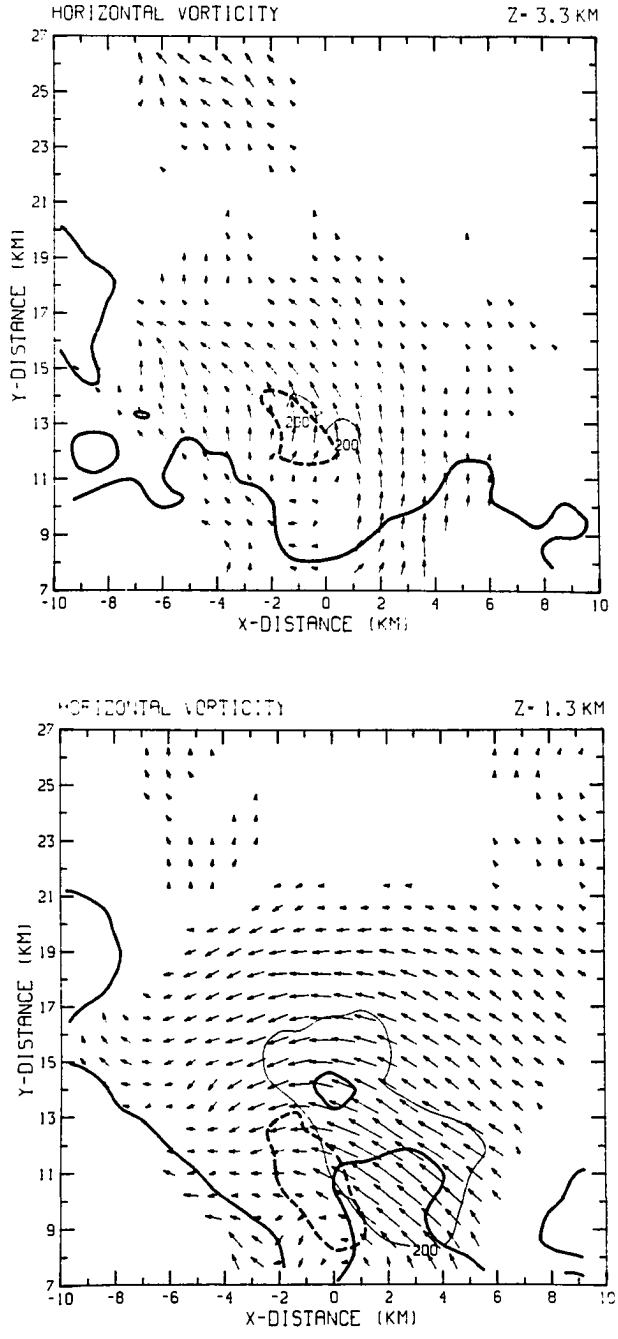

Figure 7. Horizontal vorticity at 1.3 and 3.3 km elevation prior to tornadogenesis in the Del City-Edmond thunderstorm (1826 CST). Rotation axis in plane shown vectorally. Only vorticity values $\geq 50 \times 10^{-4}$ s^{-1} plotted. Contouring interval 200×10^{-4} s^{-1}. Heavy line denotes 30 dBZ radar reflectivity contour and heavy dashed line denotes mesocyclone.

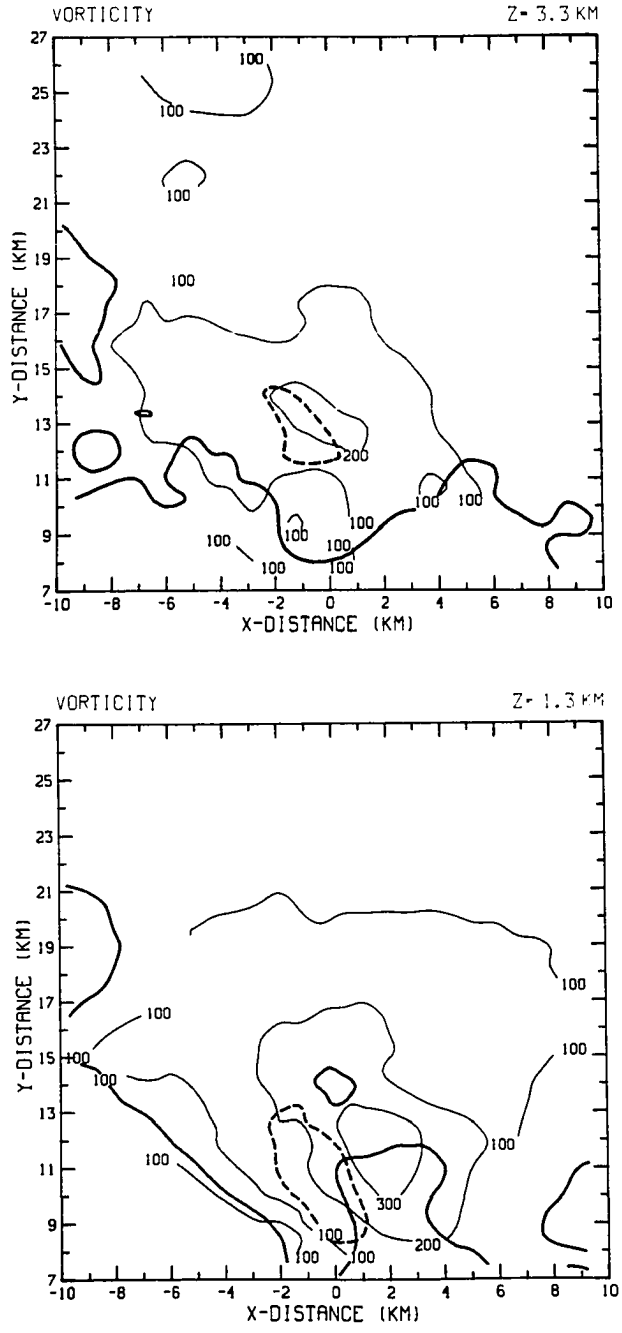

Figure 8. Magnitude of the total (three-dimensional) vorticity at z=1.3 and 3.3 km elevation prior to tornadogenesis in the Del City-Edmond thunderstorm (1826 CST). Contouring interval is 100×10^{-4} s^{-1}. Heavy line denotes 30 dBZ radar reflectivity contour and heavy dashed line denotes mesocyclone.

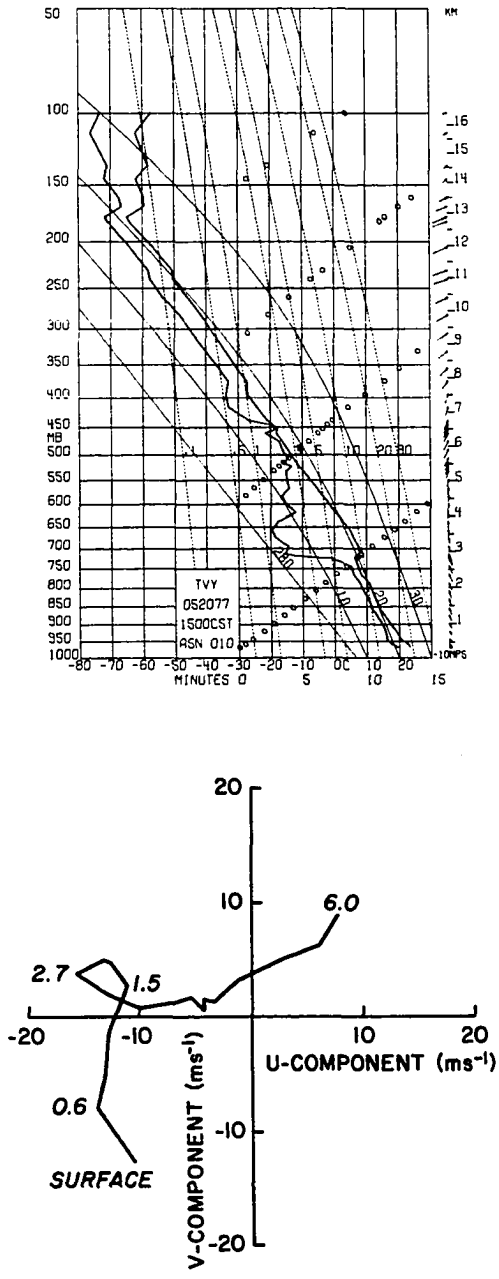

Figure 9. Stüve diagram (with ground relative wind) and hodograph (with storm relative wind) for environmental sounding released 40 km north of Norman, Oklahoma at 1500 CST on 20 May 1977. Sounding wind scale is at lower right and balloon ascent rate (height versus time) shown by circles. Heights are above mean sea level (MSL), ground height is 0.36 km. Hodograph winds are plotted at 300 m increments with select heights in km indicated.

tilted into positive vertical vorticity at rates exceeding 75×10^{-6} s^{-2} (Fig. 10). Exposure to this generation rate for just 1 min would raise vertical vorticity by ~50×10^{-4} s^{-1}--well above that pre-existing in inflow areas. The vertical vorticity actually produced, plus that already possessed by this air, is then further amplified by convergence as the flow encounters stronger updraft (Fig. 11). Because peak updraft lie in right hand (upwind) quadrants, the twisting term is predominantly dissipative within the arbitrarily defined mesocyclone. Dissipation is largely offset by convergence term vorticity amplification (70×10^{-6} s^{-2}, Fig. 11). Peak convergence term amplification 140×10^{-6} s^{-2} was computed near ground (0.3 km elevation). Both twisting and convergence term vorticity production are relatively small in regions remote from the mesocyclone and the updraft.

With height the separation between horizontal and vertical vorticity maxima diminishes (Fig. 7, z=3.3 km). Peak updraft shift to northern (downwind) quadrants of the mesocyclone, and twisting term vorticity generation becomes predominantly positive.

Air parcels passing through the elevated mesocyclone and the zone of strong twisting term generation originate mostly from lower levels on the right flank (Fig. 12) and have retained their large initial horizontal vorticity. At variance are a small number of parcels that overtake the storm from the rear and sink slightly before being entrained into the updraft. Such parcels have relatively little horizontal vorticity before entering the mesocyclone.

As also shown in the analyses of Klemp et al. (1981), in plan view, parcels from the right flank turn anticyclonically as they rise (near

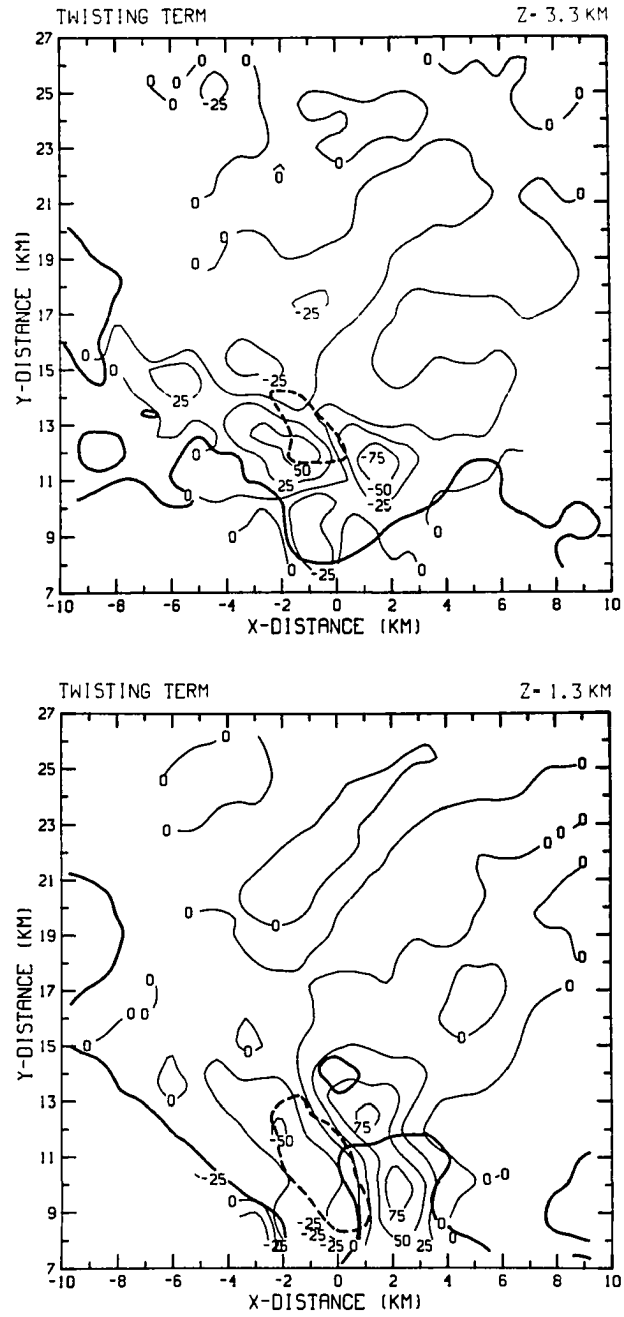

Figure 10. Vertical vorticity generation by the twisting term at 1.3 and 3.3 km elevation prior to tornadogenesis in the Del City-Edmond thunderstorm (1826 CST). Contouring interval is 25×10^{-6} s^{-2}. Heavy line denotes 30 dBZ radar reflectivity contour and heavy dashed line denotes the mesocyclone.

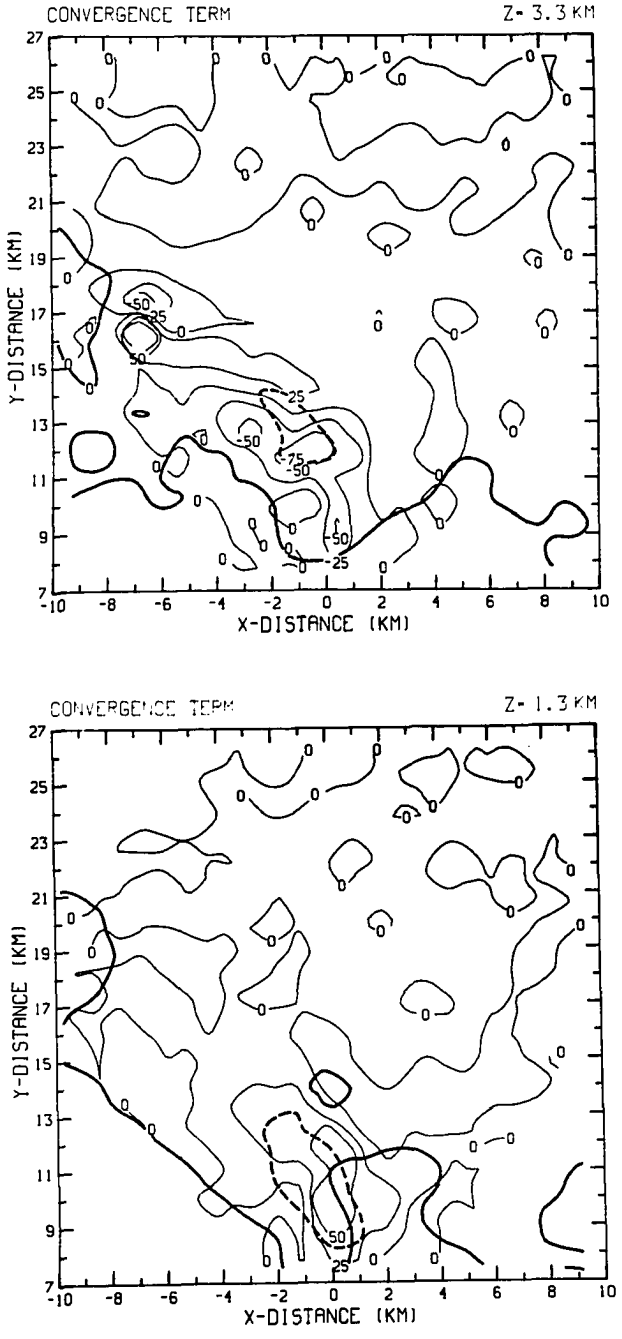

Figure 11. Vertical vorticity amplification by the convergence term at 1.3 and 3.3 km elevation prior to tornadogenesis in the Del City-Edmond thunderstorm (1826 CST). Contour interval is 25×10^{-6} s^{-2}. Heavy line denotes 30 dBZ radar reflectivity contour and heavy dashed line denotes the mesocyclone.

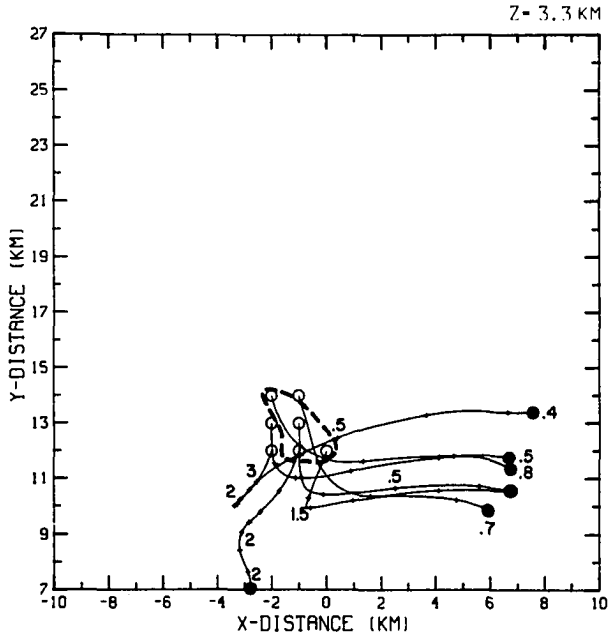

Figure 12. Parcel trajectories in the Del City-Edmond storm computed from synthesized wind fields obtained prior to tornadogenesis (1826 CST). Initial parcel locations shown by dots and final locations (all z=3.3 km) shown by open circles. Parcel paths projected on a horizontal plane. Select parcel heights (km) indicated and location of mesocyclone at 3.3 km shown by heavy dashed line. Tick marks give parcel locations at 2 min intervals.

x=-1, y=11 km). These parcels reside continuously within environs rich in positive vertical vorticity and the anticyclonic turning stems entirely from strong wind veering. Below 3.3 km, all parcels passing through the mesocyclone originate from the lower right and have trajectories similar to those in Fig. 12.

The mean and range in grid point divergence within the mesocyclone are plotted in Fig. 13. Results show that prior to tornadogenesis low level mesocyclone flow is entirely convergent (negative divergence) and the flow is convergent in the mean to ~2 km. The range in values is relatively small. With elevation, the updraft slopes more rapidly than the mesocyclone and the mean flow becomes divergent. Notwithstanding, updrafts exist throughout the mesocyclone (e.g., z=3.3 km, Fig. 5).

Mesocyclone vertical vorticity (Fig. 14), like horizontal and total vorticity, exhibits a slight maximum near z=1.5 km and declines slowly above. Not unexpectedly, vertical vorticity amplification by the convergence term dominates below 1.5 km (Fig. 15). Updraft repositioning and horizontal wind turning with height causes mesocyclone vorticity dissipation by twisting near ground to become productive aloft. At all levels, subgrid turbulence dissipates mesocyclone vertical vorticity. Peak grid point values, at the mesocyclone core (not shown), are about twice as large as the mean values.

Retrieved perturbation potential temperature and perturbation pressure fields (the latter with the volume mean removed) are presented in Fig. 16. Immediately apparent are the smaller wavelengths in the temperature fields. Cloud base temperatures (z=1.3 km) are relatively cool (negative perturbations), especially in updraft northwest of the

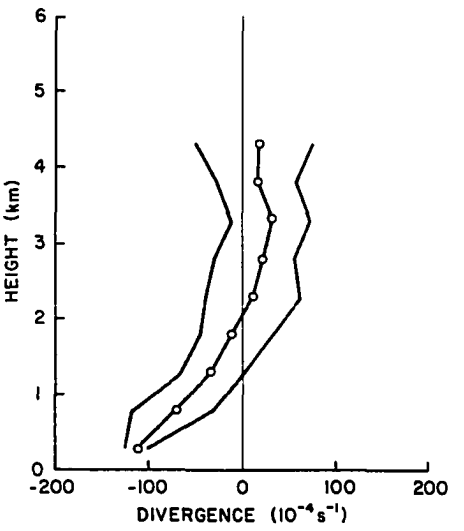

Figure 13. Vertical distribution of mean mesocyclone divergence (central curve) and the range in grid point values (outer curves) prior to tornadogenesis in Del City-Edmond thunderstorm (1826 CST).

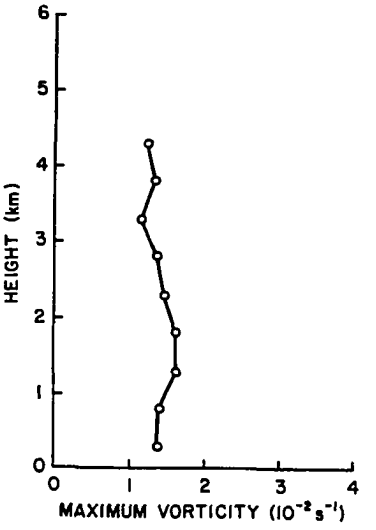

Figure 14. Vertical distribution of maximum vertical vorticity at grid points in Del City-Edmond mesocyclone prior to tornadogenesis (1826 CST).

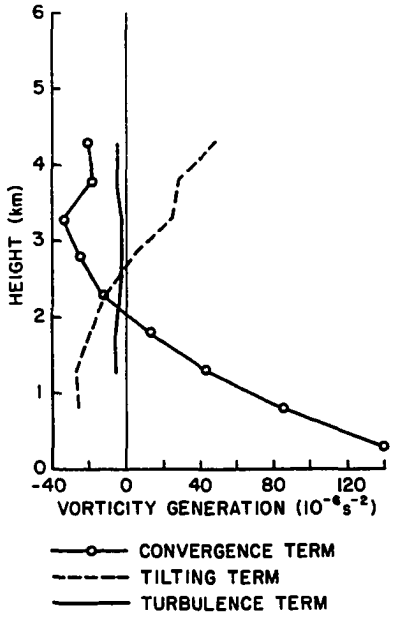

Figure 15. Vertical distribution of mean mesocyclone vertical vorticity production by the convergence, tilting, and turbulence terms prior to tornadogenesis in the Del City-Edmond thunderstorm (1826 CST).

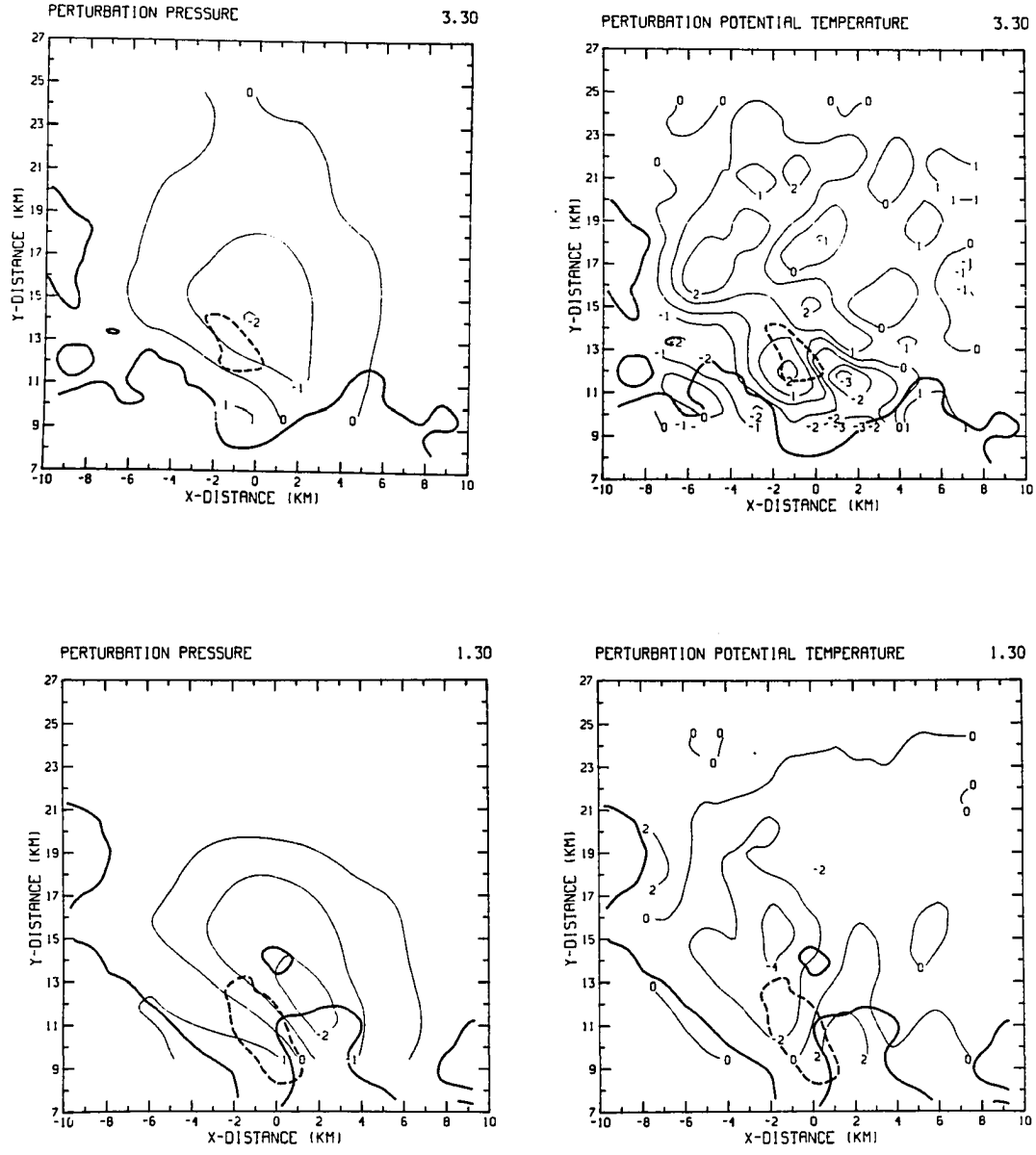

Figure 16. Retrieved perturbation potential temperature in °C and perturbation pressure in mb at 1.3 and 3.3 km elevation prior to tornadogenesis in Del City-Edmond thunderstorm (1826 CST). Heavy line denotes 30 dBZ radar reflectivity contour and heavy dashed line denotes the mesocyclone.

mesocyclone (x=-2, y=15 km). Cool temperatures are attributed to adiabatic cooling during ascent and to the evaporation of droplets falling into the unsaturated updraft. The air ascends because its negative buoyancy is overcome by a strong upward perturbation pressure gradient ($-\frac{\partial p'}{\partial z}$, Fig. 17).

Relatively warm air is evident upwind of major updraft on the storm's fringe (x=1, y=10 km). The term $\nabla^2 \frac{dw}{dt}$ (Eq. 8) is large here and θ' is essentially proportional to $\frac{dw}{dt}$. The thermal gradient across the mesocyclone may relate to both evaporative and adiabatic processes, i.e., air parcels originating from the lowest levels and having the longest path lengths through the storm are the most cooled.

Minimum pressure at z=1.3 km coincides with the three-dimensional vorticity maximum (Figs.16 and 8) and is 2-3 km northeast of the major updraft and the mesocyclone center. The rate of strain contribution to pressure forcing is large here, but its magnitude is about one-half that of the vorticity forcing. Low level moist inflow from the right flank is accelerated by pressure gradients toward the leading edge of the updrafts and toward the region of maximum vorticity generation by twisting. Farther west the pressure gradient reverses as vorticity decreases and the flow turns upward.

At 3.3 km the storm interior is warmed by the release of latent heat by condensation. Warmest temperatures are displaced slightly upwind of peak updrafts, i.e., where the advective terms $u \frac{\partial w}{\partial x}$ and $v \frac{\partial w}{\partial y}$ are large. Cool temperatures on the southern storm fringe are suggestive of evaporative cooling as dry environmental air (Fig. 9) overtakes the storm. The cold pocket at x=1, y=11 km is suspicious.

Much like the three-dimensional vorticity maximum, the low center slopes northwestward with height and weakens slowly. As in studies by

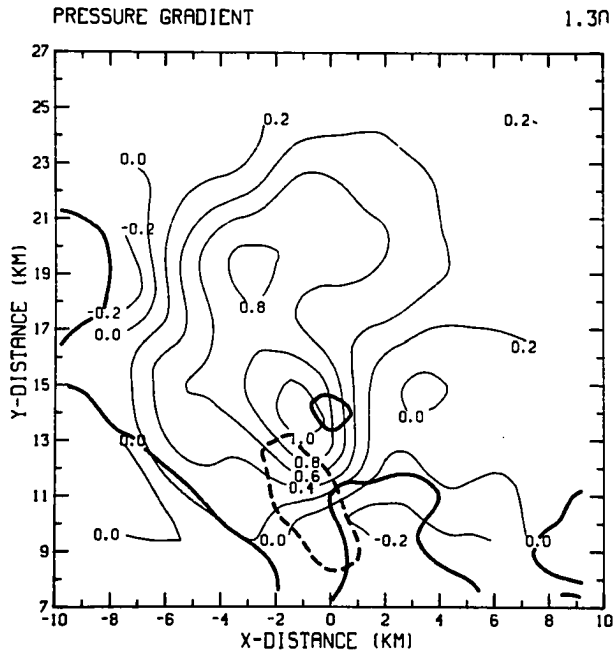

Figure 17. Computed vertical perturbation pressure gradient $[\equiv -\frac{\partial p'}{\partial z}]$ at z=1.3 km elevation prior to tornado development in the Del City-Edmond thunderstorm (1826 CST). Contour interval 0.2 mb km^{-1}. Mesocyclone indicated by heavy dashed line and heavy line denotes 30 dBZ radar reflectivity contour.

Bonesteele and Lin (1978) and Pasken and Lin (1982), high pressure is indicated on the storm's rear. Unfortunately the data do not extend sufficiently far upwind so that the vertical pressure gradient forces existing in the stagnation region between storm and environmental flows can be unambiguously determined.

2. 1845 CST: Tornadic Stage

Only single Doppler radar observations were available when the incipient tornado circulation was first detected (1838; Brandes, 1981). An anomalous shear zone indicative of the tornado formed along the elongated horizontal axis of the mesocyclone and was most prominent below 2 km. The anomaly could not be distinguished from mesocyclone flow above 3 km. Field surveys suggest tornado-like wind damage began at 1840 and ended at 1912.

The transition to the tornadic stage is marked by the development of a large cyclonic circulation (Fig. 18) that extended to above 10 km. The elongated updraft and vertical vorticity zones of the pretornadic stage had become distinctly arc-shaped as the low level gust front (in vicinity of the 30 dBZ contour) was accelerated forward by the intensifying mesocyclone (also Fig. 19). The tornado coincides with the vertical vorticity maximum and resides within the strong vertical wind gradient between the principal storm updraft and an intense rear downdraft that has formed on the storm's rear. Vertical vorticity also concentrates near the gust front and extends weakly in a broad band ~5 km wide ahead of it. Anticyclonic vorticity persists in the rainy downdraft

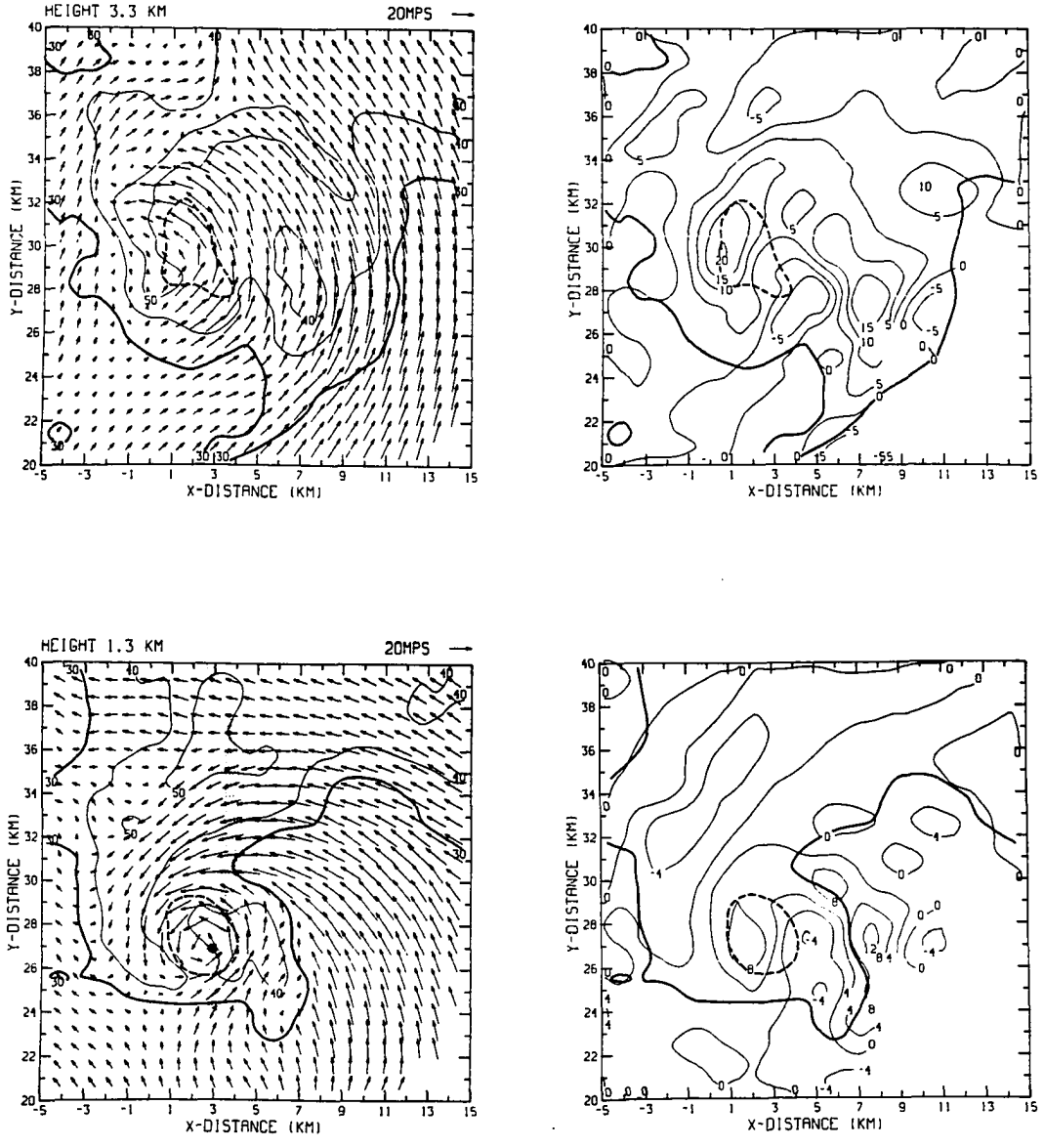

Figure 18. Storm flow, as in Fig. 5, except for tornadic stage (1845 CST). Tornado indicated by dot.

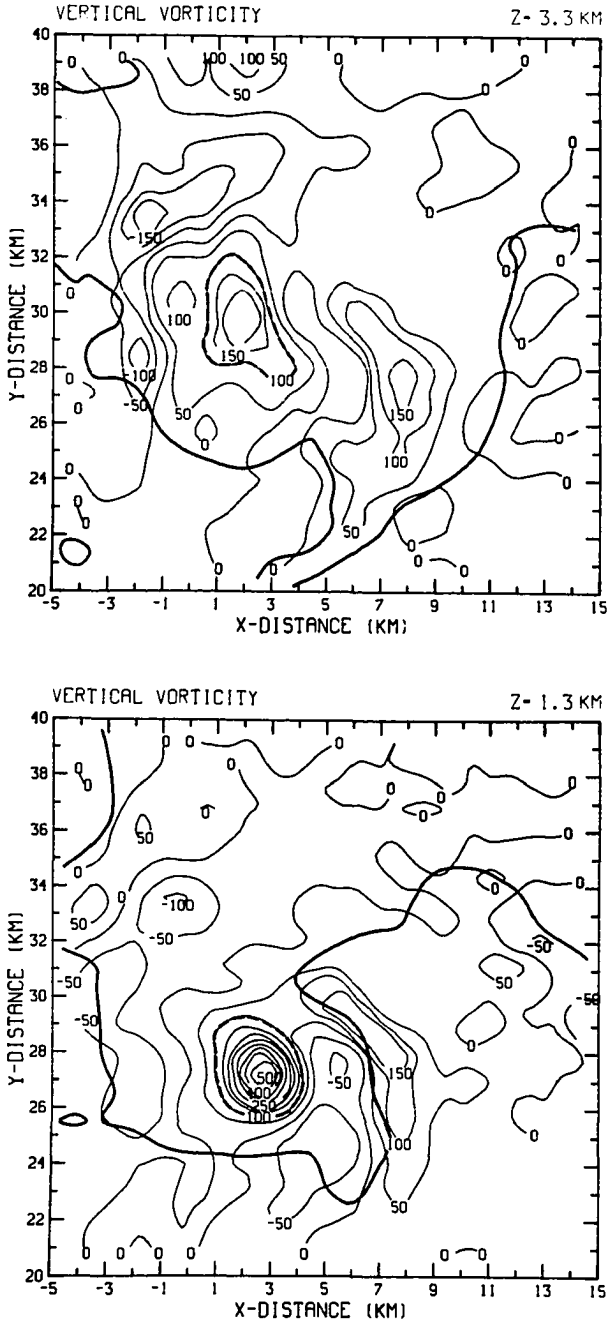

Figure 19. Vertical vorticity, as in Fig. 6, except for tornadic stage (1845 CST).

and on the storm's rear left flank. In addition, anticyclonic vorticity now concentrates in the rear downdraft region (x=5, y=25, z=1.3 km).

In simulated thunderstorms, updraft and vertical vorticity intensification respond to the strengthening of rainy downdraft and the resulting interaction between subsiding and inflow air at gust fronts (Klemp and Rotunno, 1983). Evidence for such an interaction includes a small increase in areal coverage of strong rainy downdrafts (x=-1, y=32, z=1.3 km), a reduction in areal coverage of radar reflectivity $\geq$50 dBZ, enhancement of the vertical wind gradient between the rainy downdraft and the updraft and a noticeable growth of updraft near the elevated mesocyclone (z=3.3 km).

Increased vertical vorticity (manifest by mesocyclone intensification, greater mesocyclone areal coverage, and the development of new circulation centers along the vorticity arc) matches a substantial reduction in areal coverage and intensity of strong horizontal vorticity (Fig. 20). Maximum horizontal vorticity has declined (270×10^{-4} s^{-1}, z=1.3 km) and now concentrates close to the mesocyclone and in a narrow band slightly ahead of the perturbed updraft and vertical vorticity zones.

Air parcels approaching the mesocyclone from ahead of the gust front experience both twisting term generation and dissipation (Figs. 21 and 22, z=1.3 km). Maximum production has shifted to the mesocyclone and is more complex than in pretornadic stages. Air parcels passing ahead of the gust front attain their maximum horizontal vorticity about 2 km north of the mesocyclone. This vorticity is slowly tilted into anticyclonic vertical vorticity as the flow skirts the mesocyclone's

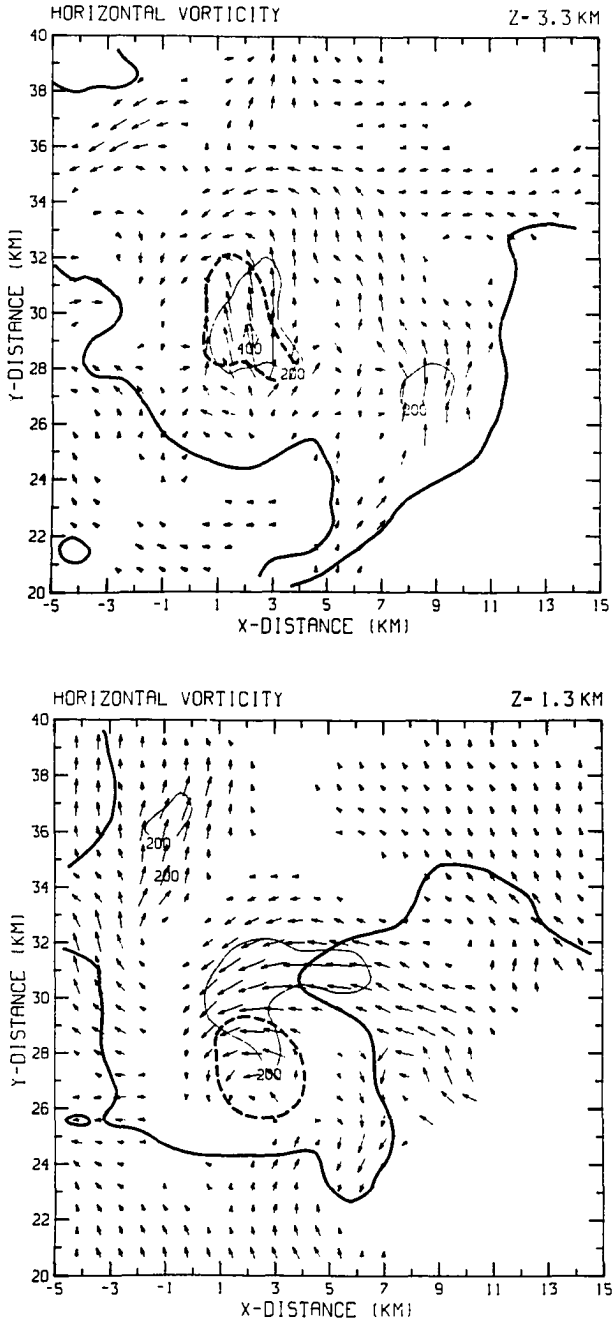

Figure 20. Horizontal vorticity, as in Fig. 7, except for tornadic stage (1845 CST).

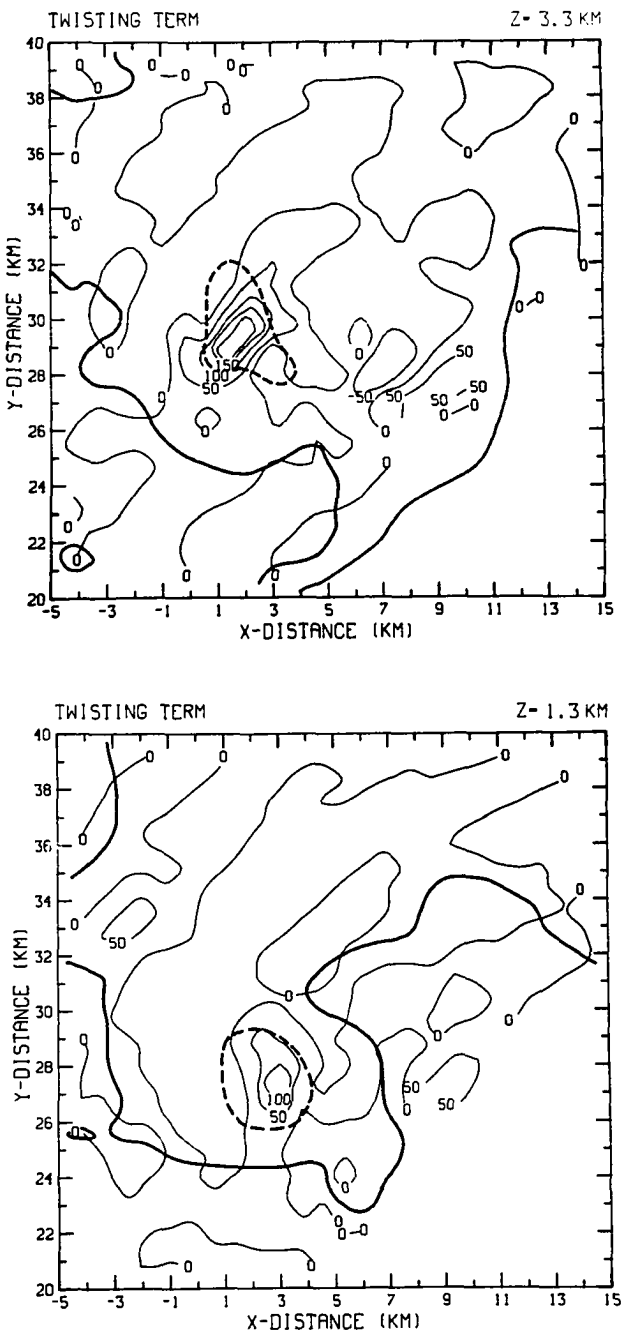

Figure 21. Vertical vorticity generation by twisting term, as in Fig. 10, except for tornadic stage (1845 CST). Contouring interval 50×10^{-6} s^{-2}.

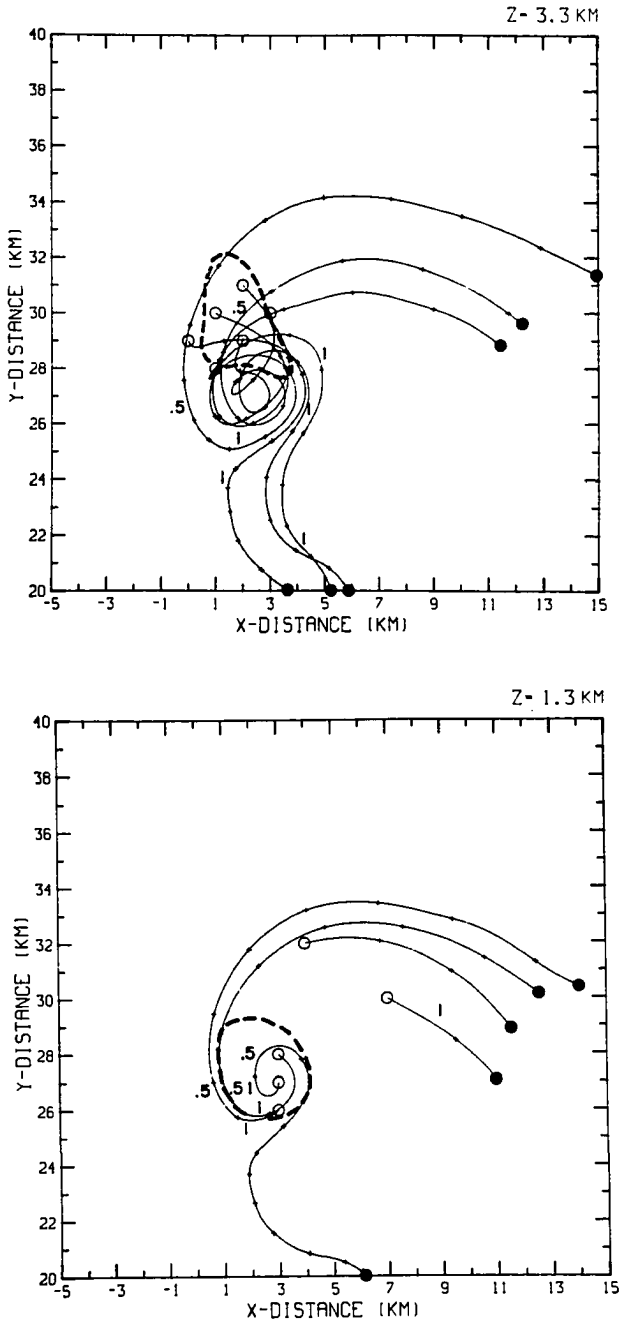

Figure 22. Parcel trajectories, as in Fig. 12, except for tornadic stage (1845 CST). Histories shown for select parcels at 1.3 and 3.3 km elevation.

western fringe. Then, as the flow continues south and east of the mesocyclone center, horizontal vorticity is reacquired. This enhancement of horizontal vorticity seems related to the general intensification and restructuring of storm vorticity. Updraft perturbation and rear downdraft formation have reversed the vertical wind gradient across the low level mesocyclone (c.f., Figs. 18 and 5); the gradient tilts the horizontal vorticity into positive vertical vorticity.

Moderate horizontal vorticity possessed by rear downdraft air primarily tilts into anticyclonic vorticity southeast of the mesocyclone (x=4, y=23-26 km). A small number of air parcels from the storm's rear are swept up by the low level mesocyclone and their horizontal vorticity is converted to cyclonic vertical vorticity at rates sufficient to overcome their initial anticyclonic vorticity (see Fig. 22, z=1.3 km, for an example). Like flow originating ahead of the gust front, these parcels gain horizontal vorticity once they enter the mesocyclone. Except in close proximity to the mesocyclone, horizontal vorticity in the rear downdraft decreases with height; hence, the vertical transport of horizontal vorticity is negative.

Vorticity amplification by convergence (Fig. 23) is extremely large in updraft to the left of the tornado, exceeding the twisting term production by almost a factor of three. Productivity relates to the interaction between inflow and rainy downdraft air. The region of strong vorticity amplification extends upwind toward flow from the storm's right flank. Strong convergence term dissipation in eastern mesocyclone quarters relates to downdraft infiltration, while weak convergence term production in portions of the downdraft (e.g., x=5, y=27, z=1.3 km) represents the compression of anticyclonic vortex tubes.

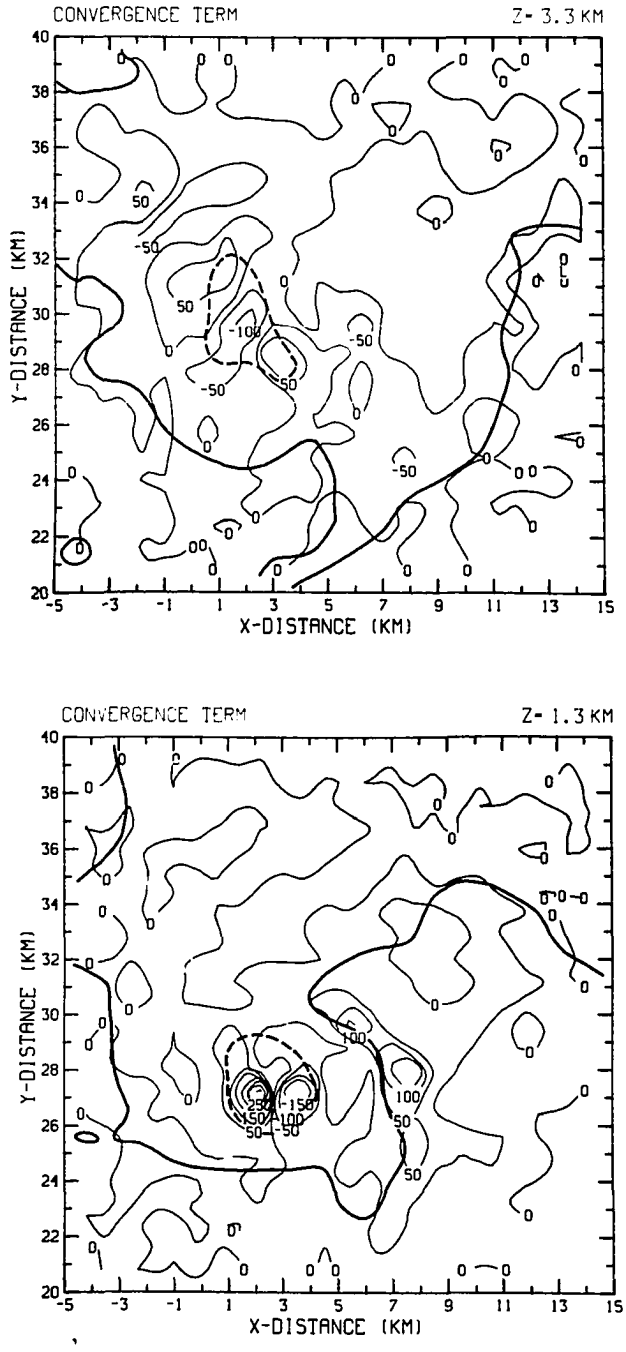

Figure 23. Vertical vorticity amplification by convergence term, as in Fig. 11, except for tornadic stage. Contouring interval is 50×10^{-6} s^{-2}.

Vertical advection of vertical vorticity $-w \frac{\partial \zeta}{\partial z}$ responds principally to mesocyclone inclination. A westward slope near ground toward strong updrafts causes vertical vorticity advection in left hand quadrants to be negative as weak vorticity is brought upward (z=0.8 km, Fig. 24). In extreme right hand sections advection is negative as weak vertical vorticity is brought downward from above. Throughout much of the rear downdraft (e.g., x=4, y=24 km), advection is positive because anticyclonic vertical vorticity decreases with height. Positive vorticity is not transported. East of the mesocyclone (x=5, y=27 km) the vertical gradient of anticyclonic vorticity reverses and advection is negative. Again only anticyclonic vorticity is involved.

Turbulent diffusion of vertical vorticity is shown in Fig. 25. Dissipation, about an order of magnitude less than the convergence term and a factor of three less than the twisting term, concentrates within the mesocyclone. In regions of strong anticyclonic vorticity, e.g., the rear downdraft, positive vorticity diffusion disperses anticyclonic vorticity.

The strengthened updraft and the rear downdraft combine effectively at higher elevations to tilt horizontal vorticity toward the vertical (z=3.3 km, Fig. 21). Vorticity is dissipated by the convergence term in central regions of the elevated mesocyclone (z=3.3 km, Fig. 23). Amplification in the northern third relates to updraft slope, while amplification in the southern third is due to convergence atop the rear downdraft. Comparison of Figs. 22 and 12 reveals the number of parcels passing through the elevated mesocyclone that are entrained from the storm's rear has increased from the pretornadic stage.

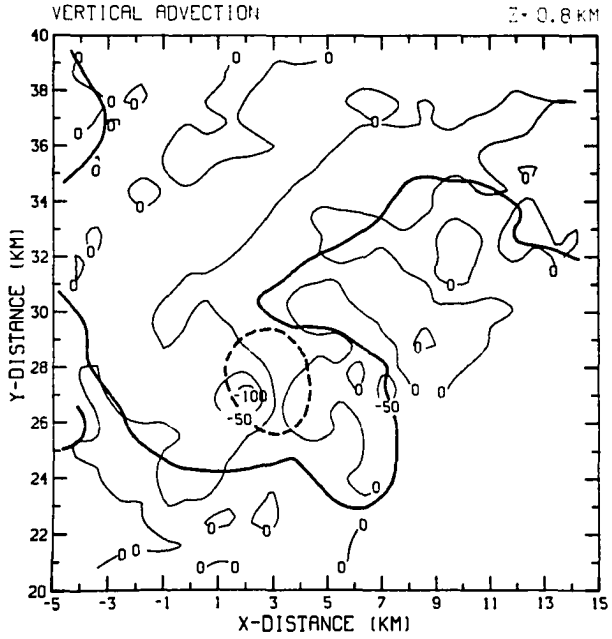

Figure 24. Vertical advection of vertical vorticity at 0.8 km elevation during the tornadic stage in the Del City-Edmond thunderstorm (1845 CST). Contouring interval is 50×10^{-6} s^{-2}. Heavy line denotes 30 dBZ radar reflectivity contour and heavy dashed line denotes the mesocyclone.

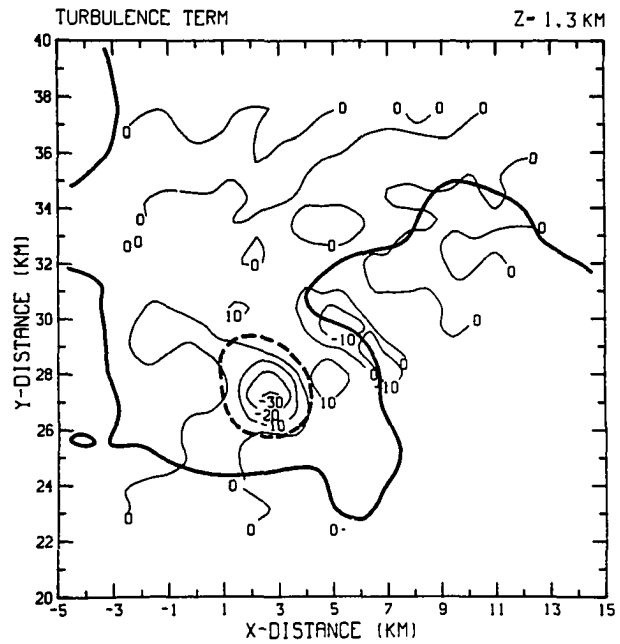

Figure 25. Vertical vorticity diffusion by turbulence term at 1.3 km elevation during tornadic stage in the Del City-Edmond thunderstorm (1845 CST). Contouring interval is 10×10^{-6} s^{-2}. Heavy line denotes 30 dBZ radar reflectivity contour and heavy dashed line denotes mesocyclone.

In summary, low level air parcels within the mesocyclone originate primarily on the storm's lower right flank and pass through a broad region where the prevailing vertical vorticity is positive. Twisting and convergence terms in the inflow region are also generally positive but neither term clearly dominates. Significant amplification of vertical vorticity occurs only in the vicinity of the mesocyclone where both convergence and twisting terms contribute to vorticity production; but the convergence term clearly dominates.

Flow overtaking the mesocyclone from the rear historically has less vorticity than air from the storm's lower right flank. Depending on the particular path taken, the horizontal vorticity of rear downdraft air is tilted either into anticyclonic or cyclonic vorticity. Little vorticity is vertically transported. Where the downdraft penetrates the mesocyclone, vertical vorticity is dissipated via the convergence term.

The distribution of maximum vertical vorticity during this early tornadic stage (Fig. 26) shows a threefold increase near ground and a twofold increase aloft. Note that the increase toward ground does not represent a lowering of an elevated vorticity maximum but follows from the production of new vertical vorticity. There has been a slight decrease in the mean convergence layer (Fig. 27) and an increase in the spread of point divergence values. The great range in values, most pronounced below 3 km, stems from rear downdraft development and enhanced local convergence. The vertical distribution of mean vorticity amplification by convergence (Fig. 28) is similar to but more intense than that at 1826. The considerable mean production relates to the enhanced convergence and occurs despite strong dissipation in eastern mesocyclone

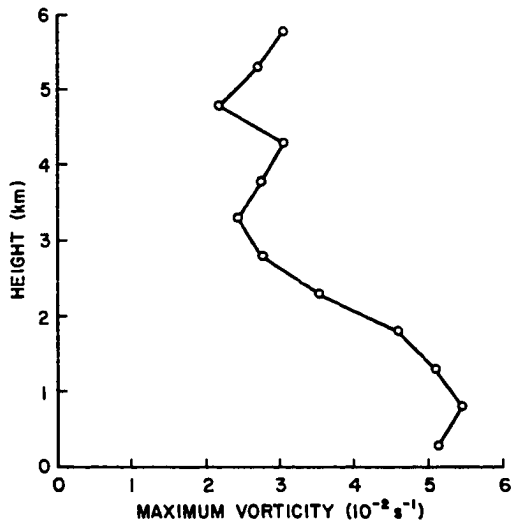

Figure 26. Vertical distribution of maximum vertical vorticity, as in Fig. 14, except for tornadic stage (1845 CST).

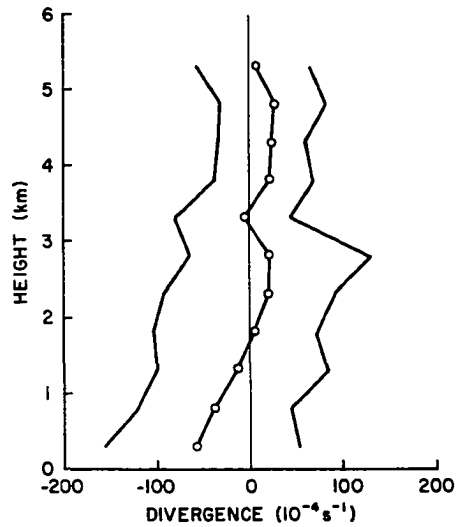

Figure 27. Vertical distribution of mean divergence and range of values, as in Fig. 13, except for tornadic stage (1845 CST).

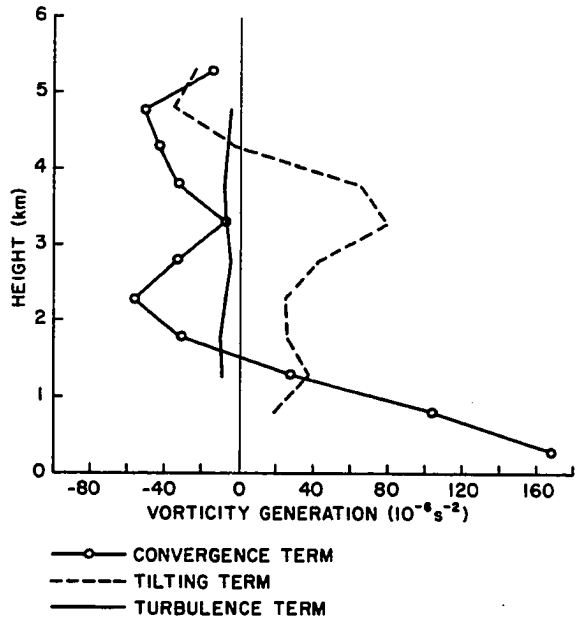

Figure 28. Vertical distribution of mean mesocyclone vertical vorticity production by the convergence, tilting, and turbulence terms, as in Fig. 15, except for tornadic stage (1845 CST).

quadrants. As discussed, low level twisting term production is now positive because the vertical wind gradient across the mesocyclone has reversed.

Actual changes in mesocyclone vertical vorticity between 1826 and 1845 are considerably less than indicated by the net rates of change for either time. The apparent discrepancy is explained by the fact that air parcels are subjected to these production rates only for short periods (Figs. 12 and 22).

Retrieved thermodynamic variables for the tornadic stage are shown in Fig. 29. Warm temperatures in the mesocyclone's eastern quadrants and behind the gust front probably result from subsidence. Warm temperatures ahead of the gust front (x=8, y=27, z=1.3 km) could represent environmental thermals. However, this region is at the boundary between observed and manufactured data which makes the temperatures suspect. Cool temperatures persist north of the mesocyclone and beneath higher reflectivity portions of the storm.

At 3.3 km, the mesocyclone and windward portions of updraft are warm. A south-to-north temperature gradient exists across the rear downdraft with coldest temperatures near peak downdrafts (x=5, y=27 km). Erosion of radar reflectivity here suggests evaporative cooling is taking place. No physical explanation is proffered for the dubious cold spot at x=8 and y=29 km.

Inspection of Figs. 16 and 29 reveals a number of locations where the sign of the temperature deviations is largely determined by the curl of the horizontal vorticity [Eq. (11)], i.e., where warm (cool) air tends to be found to the left (right) of the axis of maximum

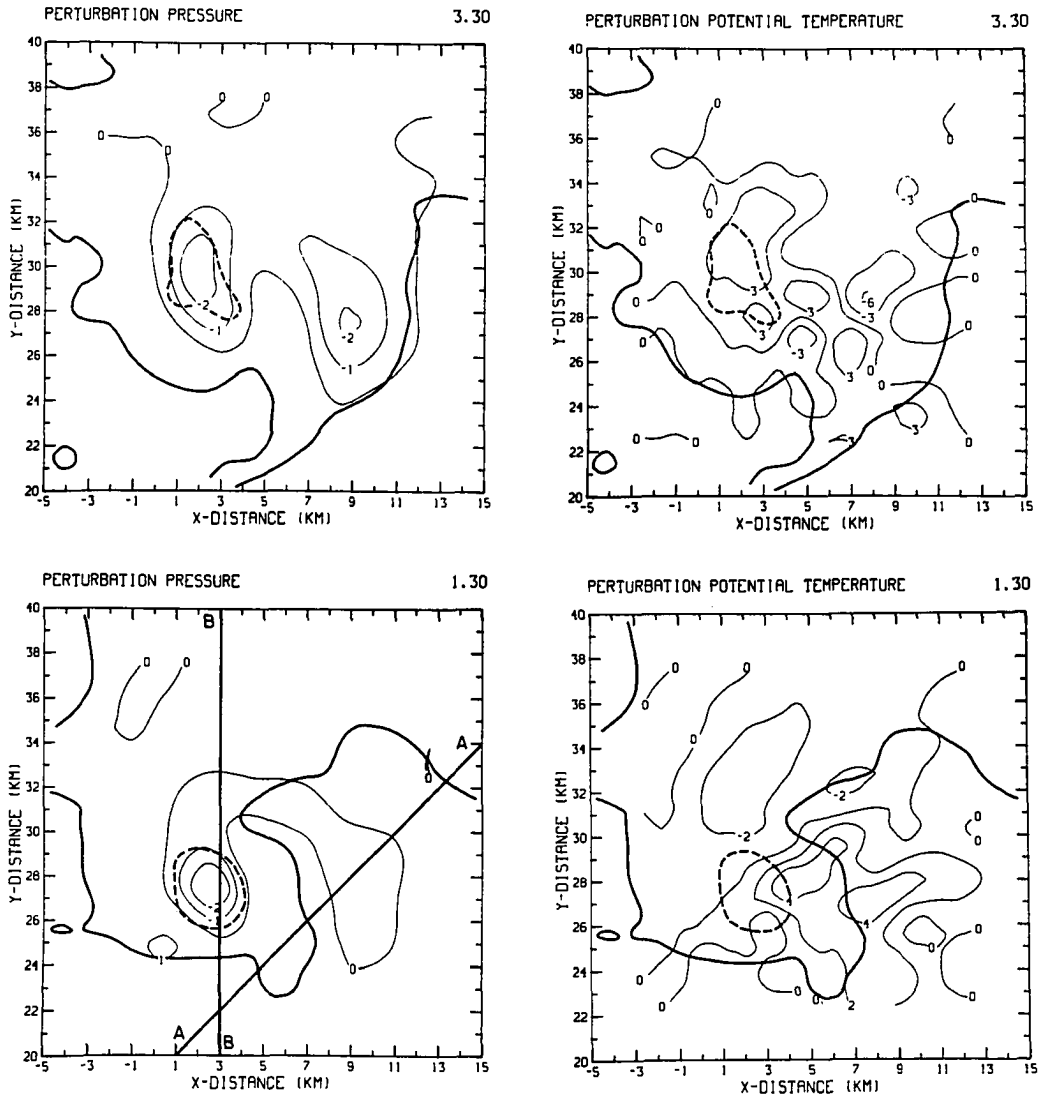

Figure 29. Retrieved perturbation potential temperature and perturbation pressure, as in Fig. 16, except for tornadic stage (1845 CST).

horizontal vorticity and where the horizontal vorticity vectors turn cyclonically (anticyclonically). See, e.g., the warm region at x=7, y=27 km and the cool regions x=5, y=27 and x=8, y=29 km (z=3.3 km, Fig. 29). Such vectoral configurations relate to toroidal circulations created by sinking cold and rising warm air.

The multifold vertical vorticity increase at low levels causes the mesolow to be colocated with the mesocyclone and reduces the central pressure. Strong pressure gradients accelerate air parcels horizontally toward the mesocyclone from all directions, including the rear downdraft. Low pressure extends from the mesocyclone ahead of the gust front to a second low center near the nose of the gust front (x=9, y=28 km). This feature corresponds with a developing mesocirculation that may have spawned a second tornado near Arcadia, Oklahoma at 1909. Relatively high pressure persists on the storm's rear and beneath the radar reflectivity core. Note the small high pressure center at the saddle point in the horizontal wind fields at z=1.3 km (x=0, y=25 km).

A vertical cross-section through the rear downdraft and in the direction of the entrained flow (Fig. 30) reveals a downward perturbation pressure gradient below 3 km that forces in situ buoyant air downward (see x=5.7, y=24.7 km). Reduced surface pressure and inclination of the mesolow with height causes downward pressure gradients in vicinity of the low level mesocyclone as well (Fig. 30). It is these pressure gradients, responding to the explosive growth of vorticity at low levels and to mesocyclone slope, that are thought to cause the sudden appearance of concentrated rear downdraft in tornadic storms.

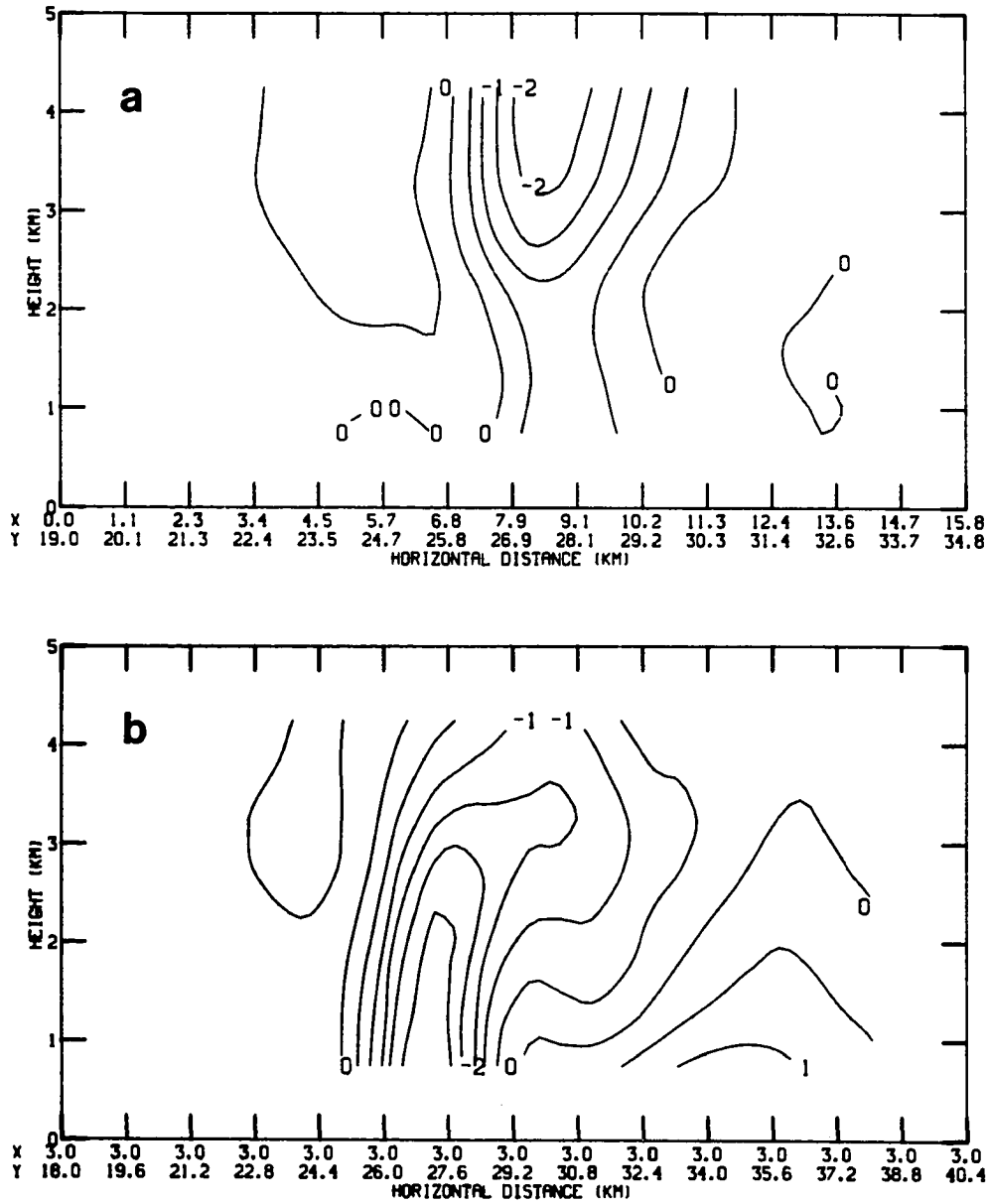

Figure 30. Vertical cross-section of perturbation pressure (a) through the rear downdraft and (b) through the mesocyclone during tornadic stage of the Del City-Edmond thunderstorm. Contour interval is 0.5 mb. Section locations shown as A-A and B-B at z=1.3 km in Fig. 29.

3. Del City - Edmond Storm Summary

Inflow air feeding the Del City-Edmond storm possessed strong horizontal vorticity which in pretornadic stages exceeded mesocyclone vertical vorticity by a factor of two. The horizontal vorticity was tipped into vertical vorticity ~2-3 km upwind of the mesocyclone. Subsequent amplification of the tilted vorticity and pre-existing vertical vorticity by the convergence mechanism raised the magnitude of the vertical vorticity above the threshold used for defining mesocyclones. The middle level mesocyclone was sustained principally by the tilting of horizontal vorticity.

A multiplicative growth of mesocyclone vertical vorticity near ground and rapid amplification of vorticity by the convergence mechanism distinguished the tornadic stage. Vorticity amplification seems tied to greater interaction between rainy downdraft air and inflow air from the storm's lower right flank. At this stage, twisting of horizontal vorticity within the mesocyclone far exceeded tilting on the fringe of the storm. The strong vorticity generation involved air parcels from the storm's lower right flank that had cycled about the mesocyclone and a small number of air parcels that were entrained from the storm's rear. The horizontal vorticity tilted was locally acquired and was associated with a general increase in vorticity during tornadogenesis. Moreover, vorticity amplification at low levels by the convergence mechanism was several times larger than the tilting rate. Because the majority of air parcels swept-up by the mesocyclone passed through the region of rapid convergence term amplification and because convergence term amplification

exceeded twisting term generation, the convergence mechanism probably triggered the tornado.

Prior to tornadogenesis, upward perturbation pressure gradients existed within the updraft and the mesocyclone. The vorticity build-up during the tornadic stage lowered the pressure deficit near ground. Consequently, vertical gradients of perturbation pressure were reduced or were reversed in vicinity of the mesocyclone. In response to the downward pressure gradients, a rear downdraft formed and a larger volume of air from the storm's rear was entrained into low levels of the mesocyclone. The downdraft warmed toward ground and its buoyancy was overcome by the pressure gradient.

B. The Oklahoma City Storm of 3 June 1974

On 8 June 1974 a major tornado outbreak occurred in central Oklahoma. Two thunderstorms passed through the radar network and were sampled repeatedly at 1° azimuthal, 1-2° elevation and 0.6 km radial intervals. The first storm struck Oklahoma City and neighboring communities with multiple tornadoes (Fig. 31).[7] Curiously, the storm had weak mesocyclones and produced a mesocyclone that was fed by inflow from ahead of the gust front only during the tornadic stage. Because mesocyclones were located in fringe areas of the storm, the extraction of thermodynamic information presented special problems. Nevertheless, the observations illustrate important storm-to-storm variations.

Interrelationships between mesocyclone flow, gust fronts and tornadoes were previously examined by Burgess et al. (1977) and Brandes

[7] Tornadic stages were 1342-1350, 1406-1412 and 1416-1428.

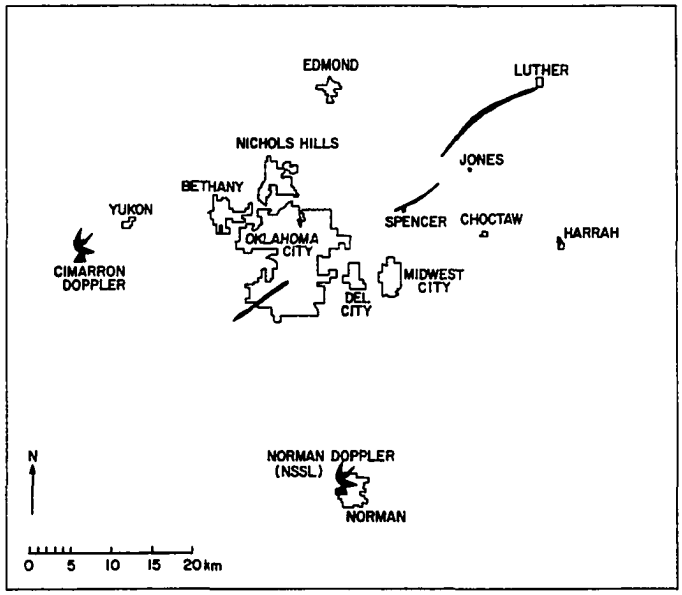

Figure 31. Map showing location of two Doppler radars and damage tracks of tornadoes produced by Oklahoma City storm of 8 June 1974.

(1977b and 1978). In addition, the observations are the basis for conceptual models of severe thunderstorms (Eagleman and Lin, 1977) and tornadogenesis (Lemon and Doswell, 1979).

1. 1315 CST: Early Storm Development

Data collection began well before genesis of the first tornado. Early observations (Fig. 32) show that radar reflectivity already exceeded 50 dBZ and that the storm width, as seen by radar, was more then 20 km. Low level horizontal winds are relatively undisturbed except for a slight cyclonic turning of the wind near the updraft and the reflectivity gradient on the storm's rear (x=-31, y=5 km). Beyond the updraft the flow turns anticyclonically into the direction of the prevailing wind.

Despite considerable data editing, computed kinematic parameters in weak signal areas (<30 dBZ) on the right flank have a noisy appearance. Hence, the spatial distribution of variables is of primary interest. Select vertical vorticity distributions for this early developmental stage are given in Fig. 33. Peak vorticity varied almost linearly from 70×10^{-4} s^{-1} at z=0.3 km to 170×10^{-4} s^{-1} at 5.3 km. Several small centers, all loosely connected with updraft, are evident. Anticyclonic vorticity tends to be distributed in several locations on the southern storm fringe where flow subsides (e.g., x=-24, y=0 and x=-29, y=-1, at z=1.3 km) and on the storm's left flank. Horizontal vorticity, associated with a veering and vertically increasing wind, concentrates in right hand storm quadrants (Fig. 34). Maximum horizontal vorticity $\sim 150 \times 10^{-4}$ s^{-1} is

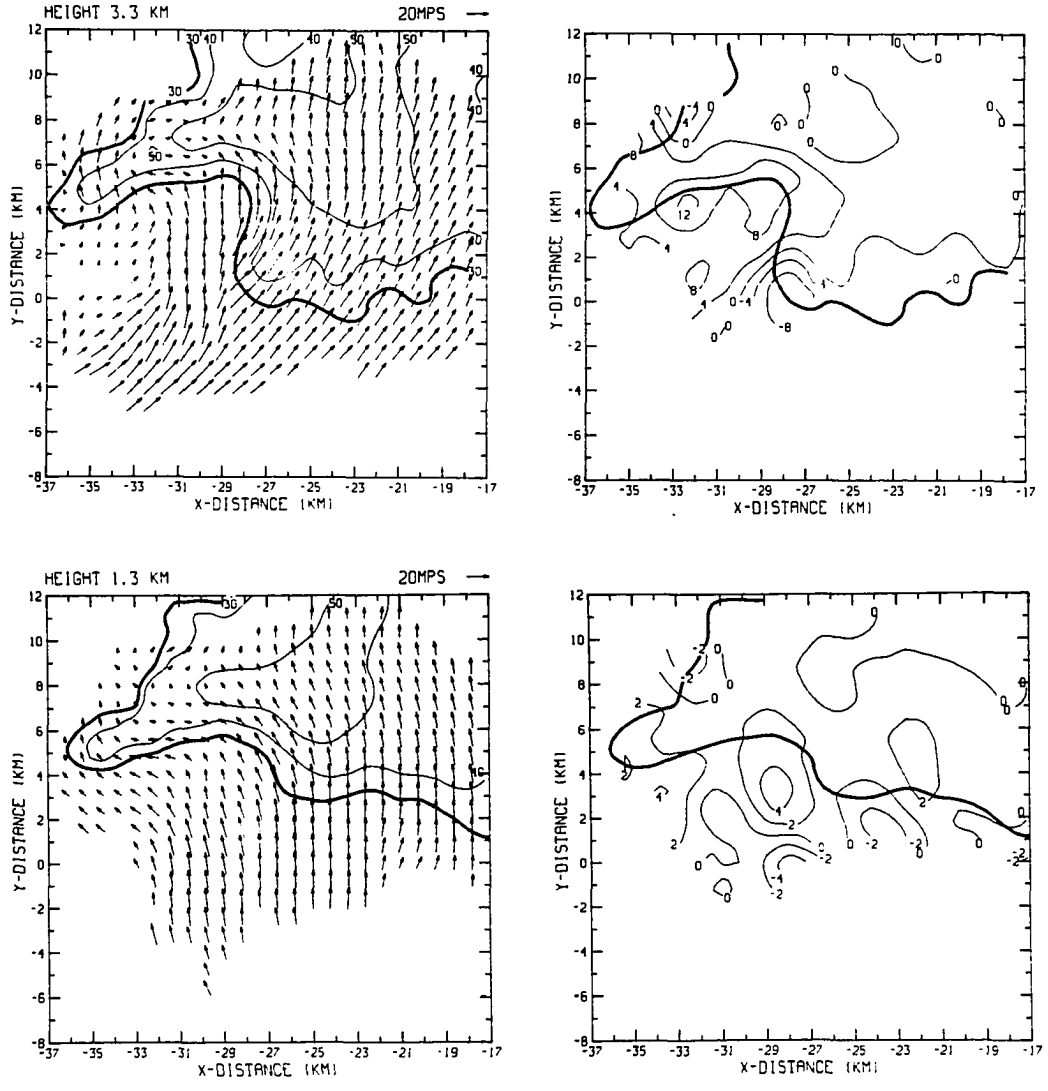

Figure 32. Wind fields early in Oklahoma City thunderstorm (1315 CST). Left hand panels show horizontal wind (vectors) relative to the storm [Cimarron radar reflectivity (dBZ) superimposed and 30 dBZ contour accentuated]. Right hand panels show vertical wind distribution (m s^{-1}) with the 30 dBZ reflectivity contour superimposed. Distances are from the Norman radar and heights (upper left) are AGL. A horizontal wind vector 1 km in length equals 20 m s^{-1}. Storm motion is from 230° at 15 m s^{-1}. (z=1.3, 3.3 km).

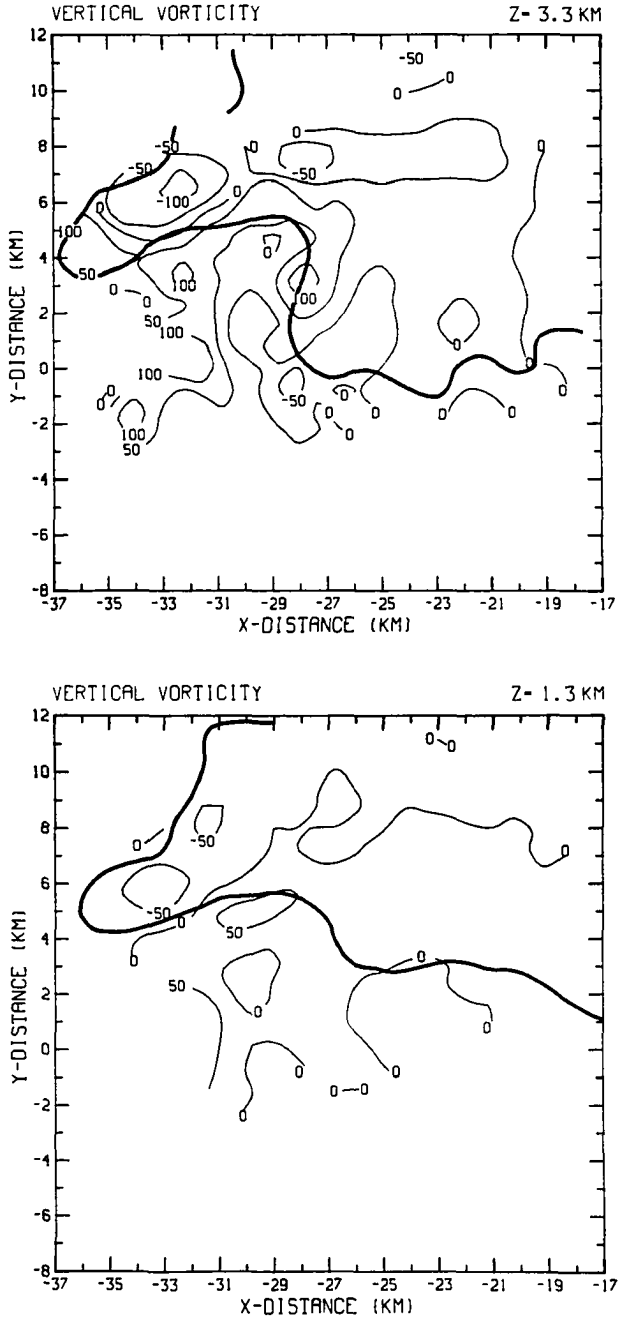

Figure 33. Vertical vorticity at 1.3 and 3.3 km elevation, early in Oklahoma City thunderstorm (1315 CST). Contouring interval 50×10^{-4} s^{-1}. Heavy line denotes 30 dBZ radar reflectivity contour.

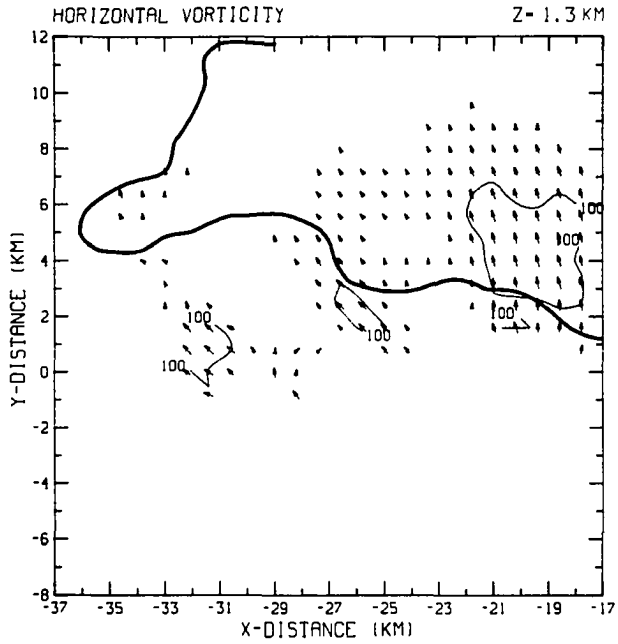

Figure 34. Horizontal vorticity at 1.3 km, early in the Oklahoma City thunderstorm (1315 CST). Local rotation axis in plane shown vectorally. Only vorticity 50×10^{-4} s^{-1} plotted. Contour interval 100×10^{-4} s^{-1}. Heavy line denotes 30 dBZ radar reflectivity contour.

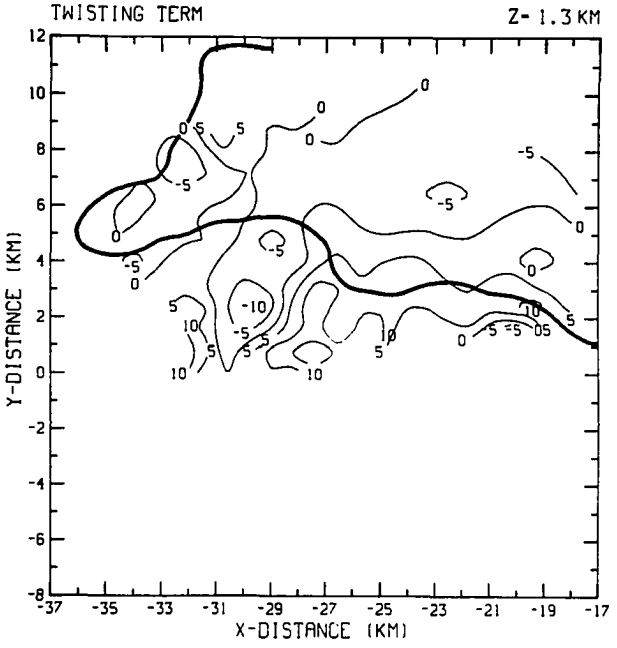

Figure 35. Vertical vorticity generation by twisting term at 1.3 km elevation, early in the Oklahoma City thunderstorm (1315 CST). Contouring interval is 5×10^{-6} s^{-2}. Heavy line denotes 30 dBZ contour.

about twice as large as low level vertical vorticity. The distribution changes little with height (not shown).

Horizontal vorticity is slowly tilted into positive vertical vorticity in upwind fringe areas, while dissipation occurs mainly in the storm interior and near x=-30, y=3 km (Fig. 35). The convergence term tends to be positive downwind from the twisting production region (e.g., near x=-28, y=3; x=-29, y=5 km and x=-23, y=5; Fig. 36). As in early stages of the Del City storm, rotation would seem determined by ambient horizontal vorticity tilted at the edge of updraft and the subsequent amplification of the tilted vertical vorticity by the convergence mechanism.

2. 1409 CST: Pretornadic Mesocyclone

After 1315 the Oklahoma City storm moved across the baseline between the radars (Fig. 31), and for a time the three-dimensional flow structure could not be resolved. Data presented in Fig. 37 were obtained while a small "gust front tornado" (the second) was in progress. The discrepancy between the radar indicated tornado location (an average position determined from the unsmoothed measurements of both radars) and the damage path is roughly equal to the spacing between measurements. However, the displacement is fairly consistent in the 8 June 1974 data and could represent a small radar ranging error.

The absence of radar scatterers precludes determination of flow properties near the gust front tornado. Instead, attention is focused on the vorticity center near x=7.5, y=36.5, z=0.3 km (Fig. 38) from

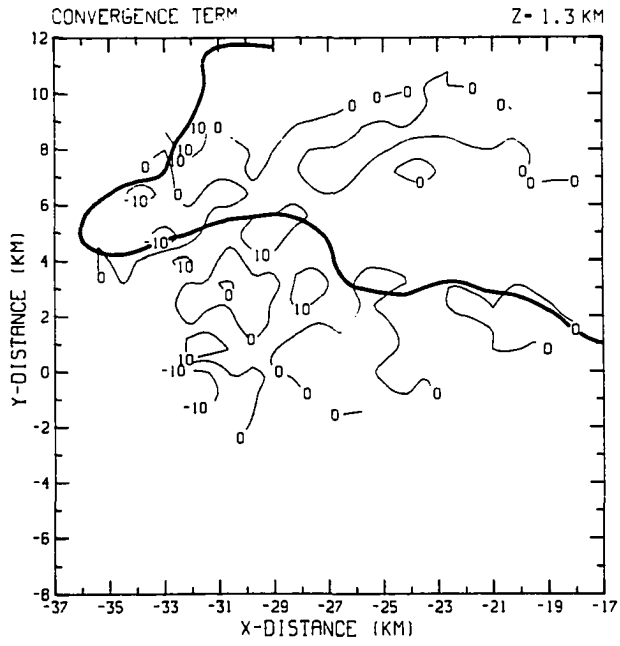

Figure 36. Vertical vorticity amplification by the convergence term at 1.3 km elevation, early in the Oklahoma City thunderstorm (1315 CST). Contour interval is 10×10^{-6} s^{-2}. Heavy line denotes 30 dBZ contour.

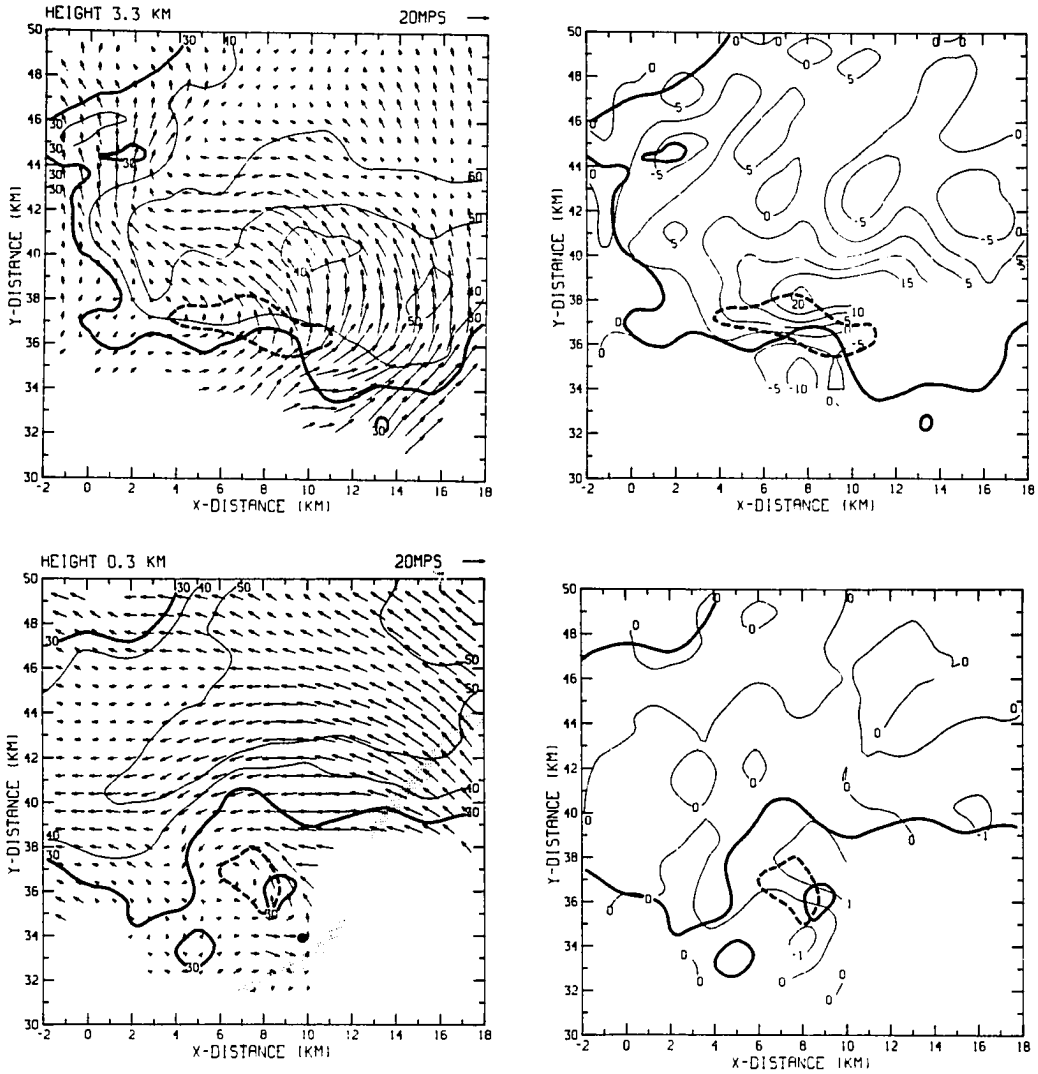

Figure 37. Storm flow, as in Fig. 32, except for 1409 CST in Oklahoma City thunderstorm. Mesocyclone indicated by heavy dashed line. Tornado damage paths are stippled. Location of gust front tornado shown by dot. Tornadic wind damage occurred from 1406 to 1412 and from 1416 to 1428.

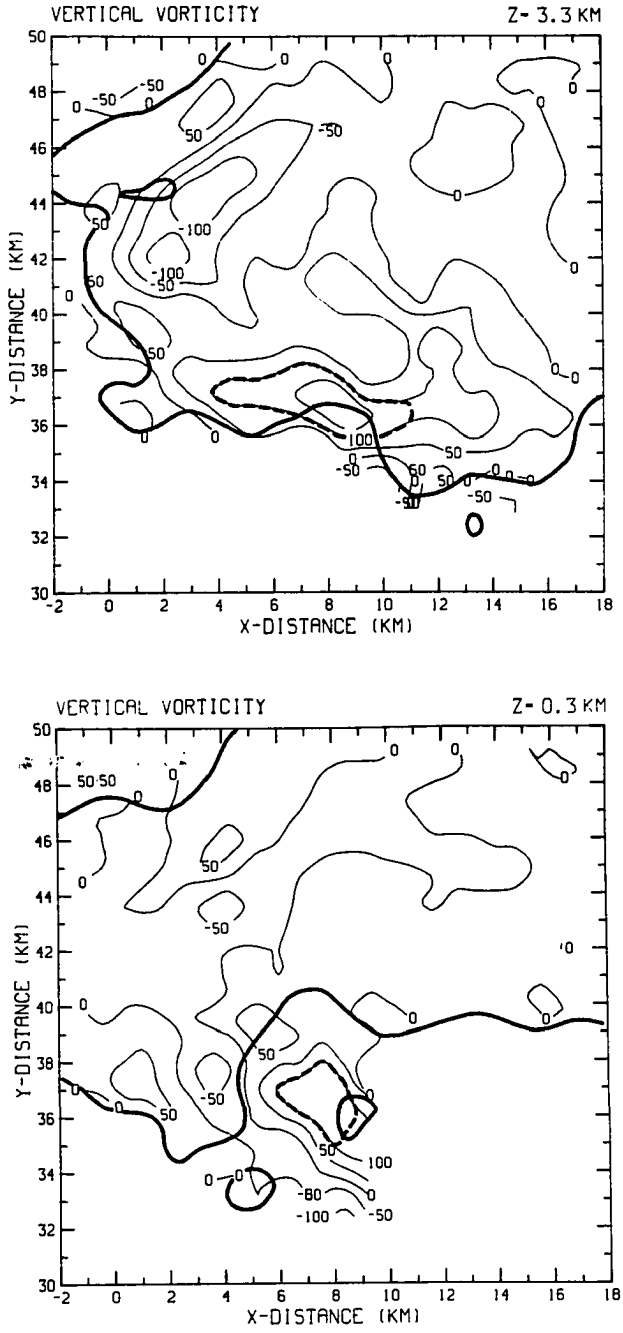

Figure 38. Vertical vorticity, as in Fig. 33, except for 1409 CST in Oklahoma City thunderstorm. Mesocyclone indicated by heavy dashed line.

which a major tornado emerged at 1416. Undoubtedly the presence of the gust front tornado influences kinematic properties computed for the latter mesocirculation.

Vertical height, strength and areal coverage of the defined mesocyclone (also Fig. 39) are all less than similar stages in the Del City storm (1826) and in the Harrah storm yet to be described (Chapter IV.C). Maximum vertical vorticity is aloft (~2.5 km), but a closed cyclonic wind pattern was discernable only at 0.3 km. Updrafts have intensified since 1315 but rainy downdrafts in trailing sections of the storm remained weak and disorganized. A rear downdraft is evident behind the gust front (x=8, y=34 km). Oddly, except in extreme northern sections, low level mesocyclone flow comprises slowly sinking air from higher levels on the storm's rear (Fig. 40). At 3.3 km elevation, the mesocyclone is elongated and lies within the vertical wind gradient on the storm's right flank. Much like the Del City storm but not yet as pronounced, radar reflectivity is eroded in the subsidence region adjacent to the mesocyclone (x=8, y=35, z=3.3 km).

The twisting term (Fig. 41, z=0.8 km) is predominately negative and weak within the low level mesocyclone. Positive vorticity is generated in the mesocyclone's southeastern (upwind) quadrant and throughout much of the rear downdraft, but production rates are $<10 \times 10^{-6}$ s^{-2}. At 3.3 km, wind veering and the vertical wind gradient combine to generate significant vorticity inside the mesocyclone. The convergence term (Fig. 42) opposes twisting near ground, i.e., vorticity is most rapidly amplified in northern mesocyclone quadrants and dissipated in the southeast. Amplification and dissipation rates are several times larger than those

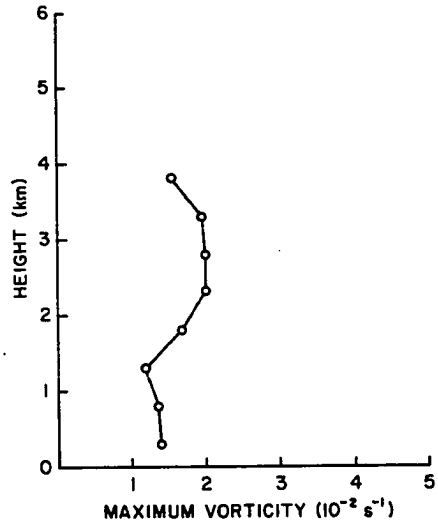

Figure 39. Vertical distribution of maximum vertical vorticity in Oklahoma City mesocyclone at 1409 CST.

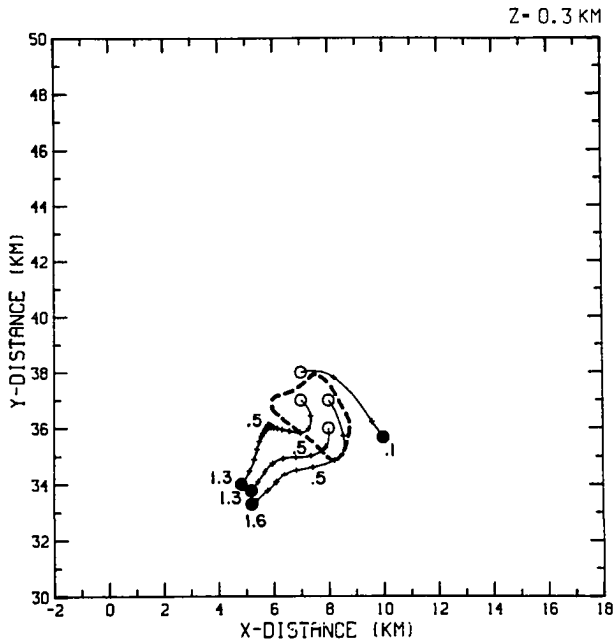

Figure 40. Air parcel trajectories in the Oklahoma City thunderstorm computed from synthesized wind fields at 1409 CST. Initial parcel locations shown by dots and final positions (all 0.3 km) shown by open circles. Tick marks give positions at 2 min intervals. Select parcel heights (km) and location of mesocyclone at 0.3 km (heavy dashed line) indicated.

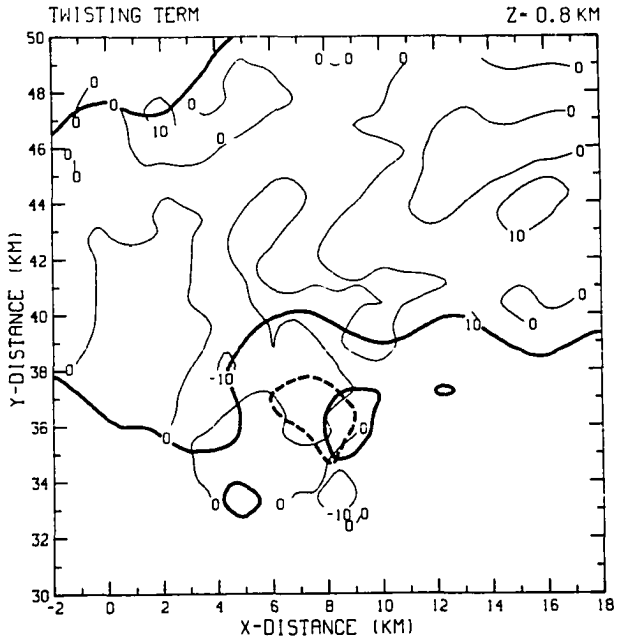

Figure 41. Vertical vorticity generation by the twisting term, as in Fig. 35, except for 1409 CST. Mesocyclone indicated by heavy dashed line.

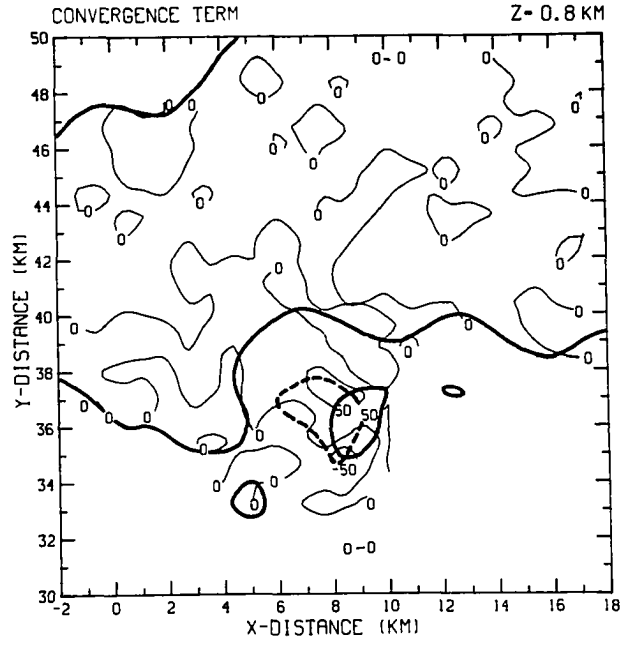

Figure 42. Vertical vorticity amplification by the convergence term, as in Fig. 36, except for 1409 CST. Mesocyclone indicated by heavy dashed line.

for twisting. Relative to pretornadic stages in the other two storms, production by both mechanisms is small.

Vertical vorticity transport within the mesocyclone is slightly negative at low levels (Fig. 43). In northern sections the vertical vorticity lapse is positive and weak vorticity is lifted from lower levels. In southern sections the vorticity gradient is reversed and weak vorticity descends in the rear downdraft. Positive transport in downdraft upwind of the mesocyclone results from positive vertical lapses of both positive and negative vorticity. Convergence term amplification of vorticity transported and tilted in the rear downdraft seems to maintain the low level mesocyclone. There is no ambiguity at middle levels; tilting clearly is the dominant mechanism.

Summarized mesocyclone properties show the mean flow is slightly convergent at low levels and divergent above ~1.5 km (Fig. 44). The range in point values is fairly large due to the presence of the rear downdraft. Mean mesocyclone vorticity production by convergence and twisting are weak below 2 km (Fig. 45). Above, the convergence term becomes dissipative and the twisting term is productive. Large twisting generation at z=3.8 km stems from colocation of a shrunken mesocyclone and the region of strong generation.

3. 1420 CST: Tornadic Stage

The Oklahoma City storm was next sampled shortly after descent of the final tornado (Fig. 46). Prominent mesocyclone morphological changes include increased rotation and greater vertical extent (Figs. 47

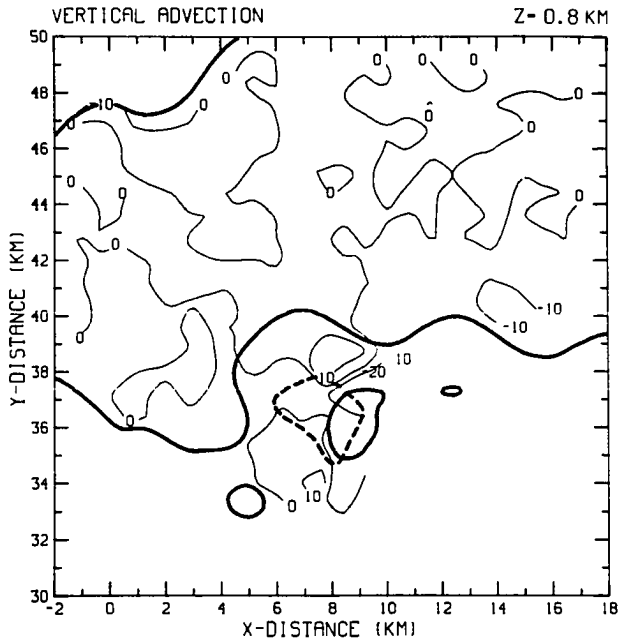

Figure 43. Vertical advection of vertical vorticity at 0.8 km elevation in Oklahoma City thunderstorm (1409 CST). Contouring interval is 10×10^{-6} s^{-2}. Heavy line denotes 30 dBZ radar reflectivity contour and heavy dashed line denotes mesocyclone.

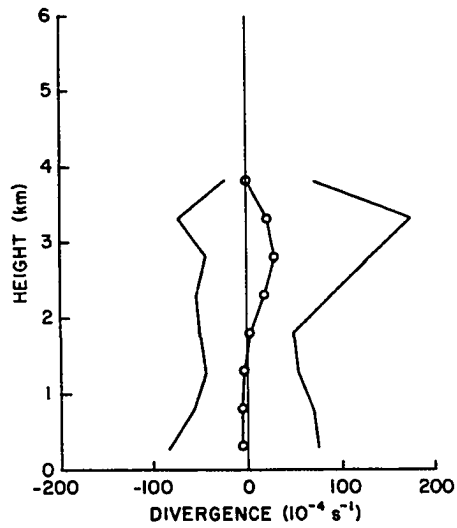

Figure 44. Vertical distribution of mean mesocyclone divergence (central curve) and the range in grid point values (outer curves) in Oklahoma City thunderstorm at 1409 CST.

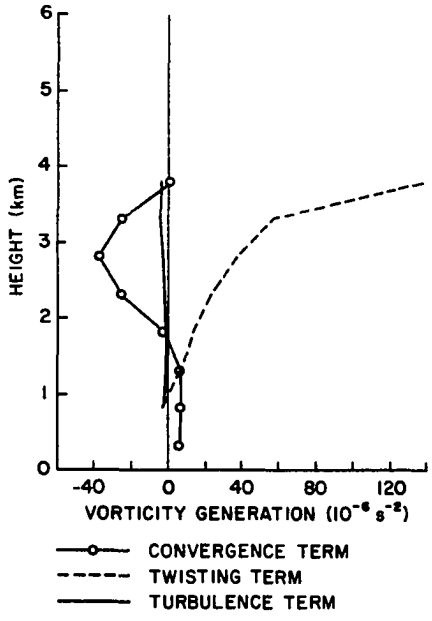

Figure 45. Vertical distribution of mean mesocyclone vertical vorticity production by the convergence, twisting and turbulence terms in the Oklahoma City thunderstorm at 1409 CST.

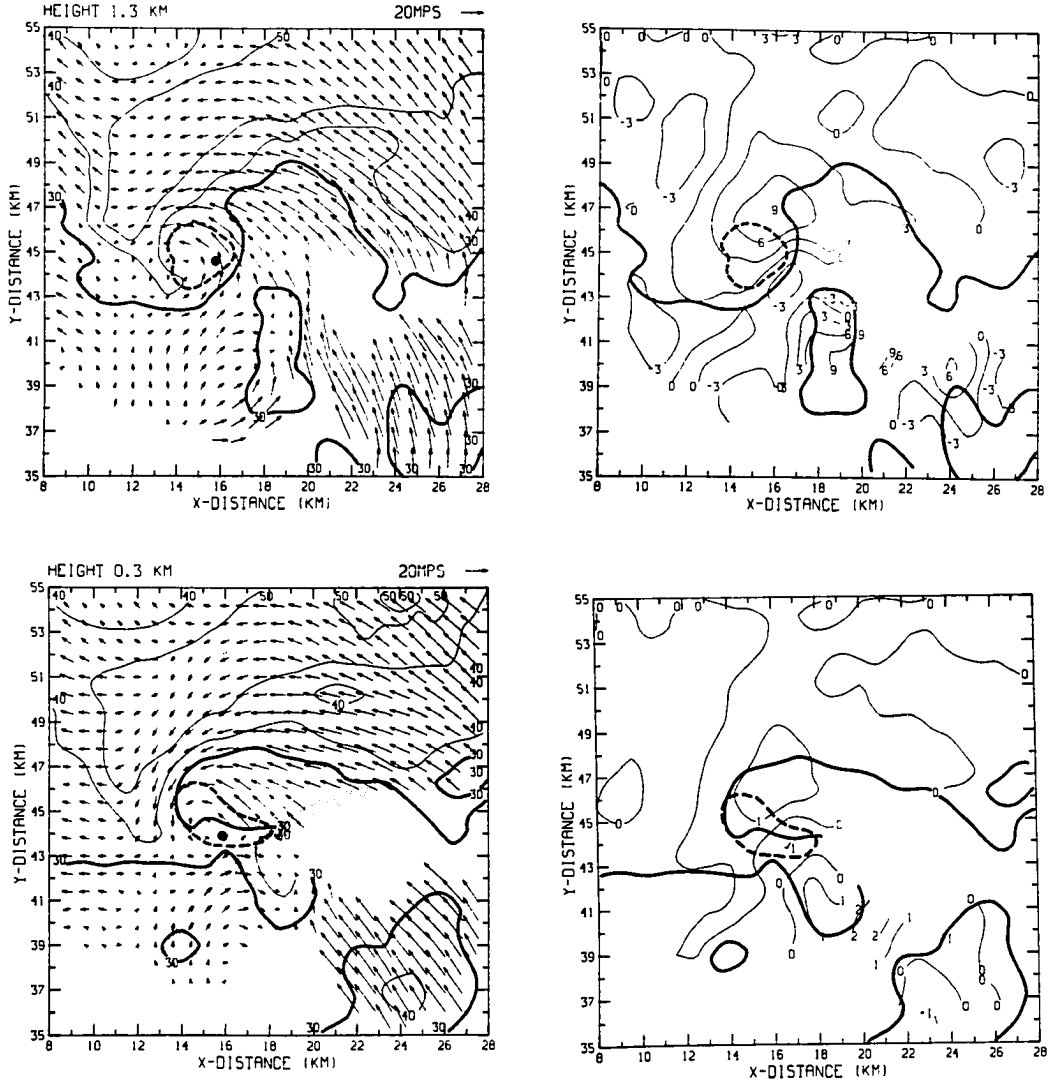

Figure 46. Storm flow, as in Fig. 32, except for tornadic stage (1420 CST). (z=0.3, 1.3, 3.3 km)

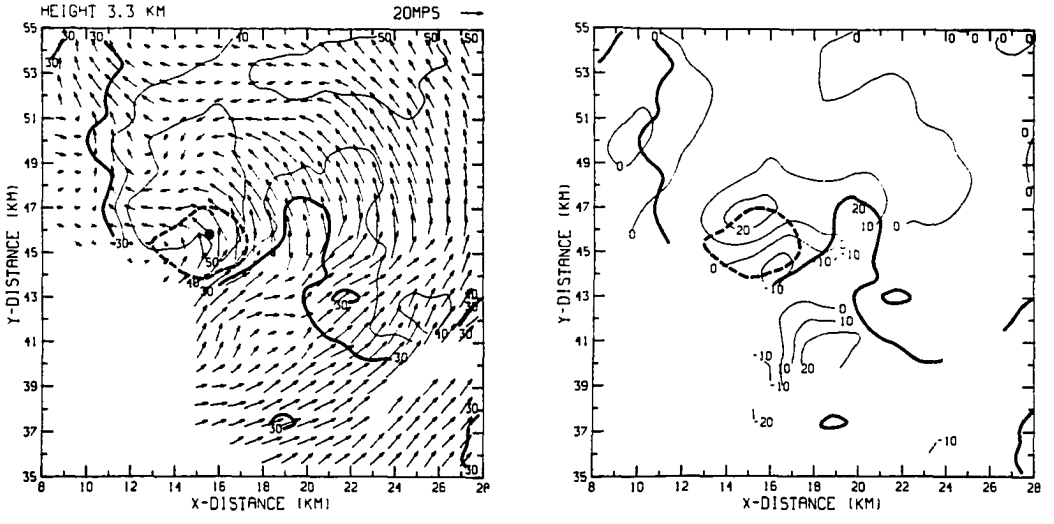

Figure 46. (Continued)

and 48). A closed wind circulation is discernable to 4 km elevation. Principal updraft have strengthened (c.f., Figs. 46 and 37, z=3.3 km) and rainy downdraft in trailing portions of the reflectivity core have become more organized and have intensified slightly (x=11, y=45-53, z=0.3 km). Interaction between sinking and inflow air from the storm's right flank could account for the increase in updraft north of the mesocyclone.

A larger volume of air is entrained into the rear downdraft; note the stronger horizontal flow at x=16, y=40, z=0.3 km and the pronounced erosion of radar reflectivity adjacent to the elevated vortex (z=3.3 km). The subsiding air generally possesses anticyclonic vertical vorticity. The coarse sampling density and smoothing in the analyzed wind fields cause the tornado to be positioned slightly within the rear downdraft at z=0.3 km. In reality the updraft to the north must extend to the tornado.

Horizontal vorticity still can not be calculated to the right of the gust front. However, local concentrations are situated northwest and southeast of the mesocyclone (Fig. 49). Twisting term vorticity generation in the southeastern half of the mesocyclone has jumped to 40×10^{-6} s^{-2} (Fig. 50). This surge relates to both a sharper wind gradient across the mesocyclone and local enhancement of horizontal vorticity. Dissipation occurs to the northwest where flow turns opposite the vertical wind gradient.

Near ground the convergence mechanism amplifies vertical vorticity in central and northern portions of the mesocyclone and had intensified since 1409 (maximum rates are $>75 \times 10^{-6}$ s^{-2}, Fig. 51).

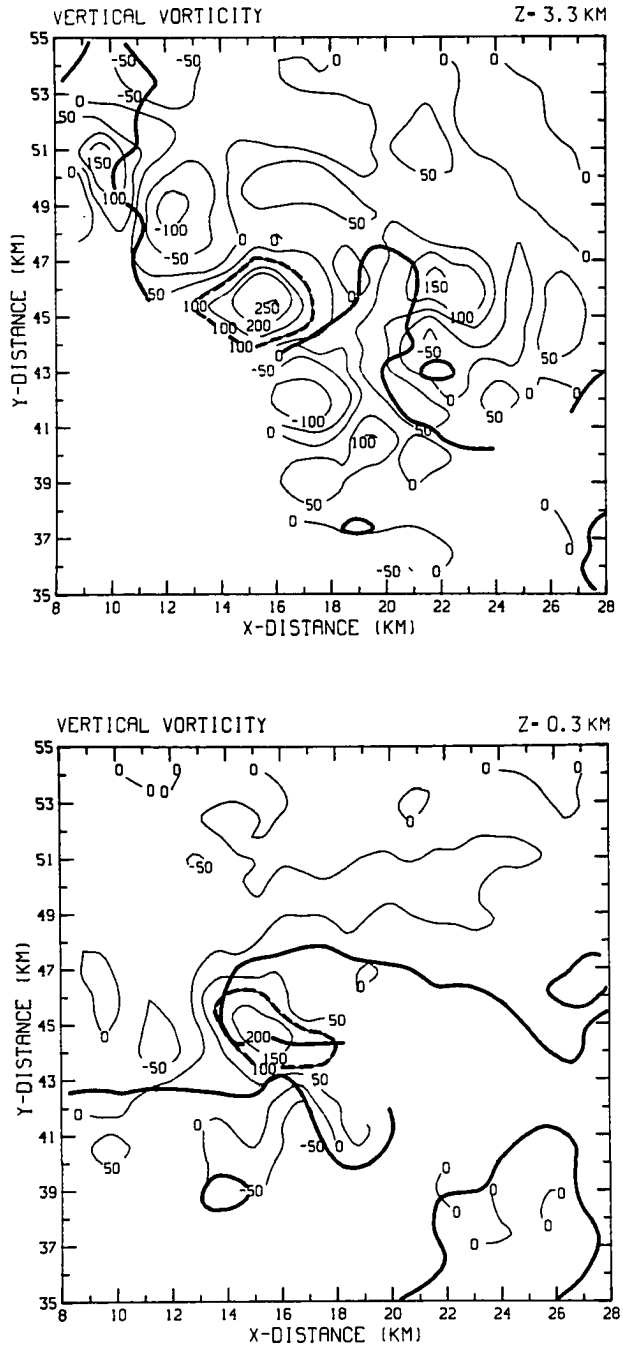

Figure 47. Vertical vorticity, as in Fig. 33, except for tornadic stage in Oklahoma City storm (1420 CST).

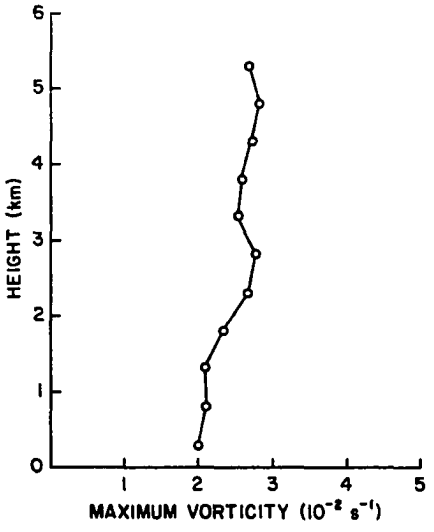

Figure 48. Vertical distribution of maximum vertical vorticity during tornadic stage in Oklahoma City mesocyclone (1420 CST).

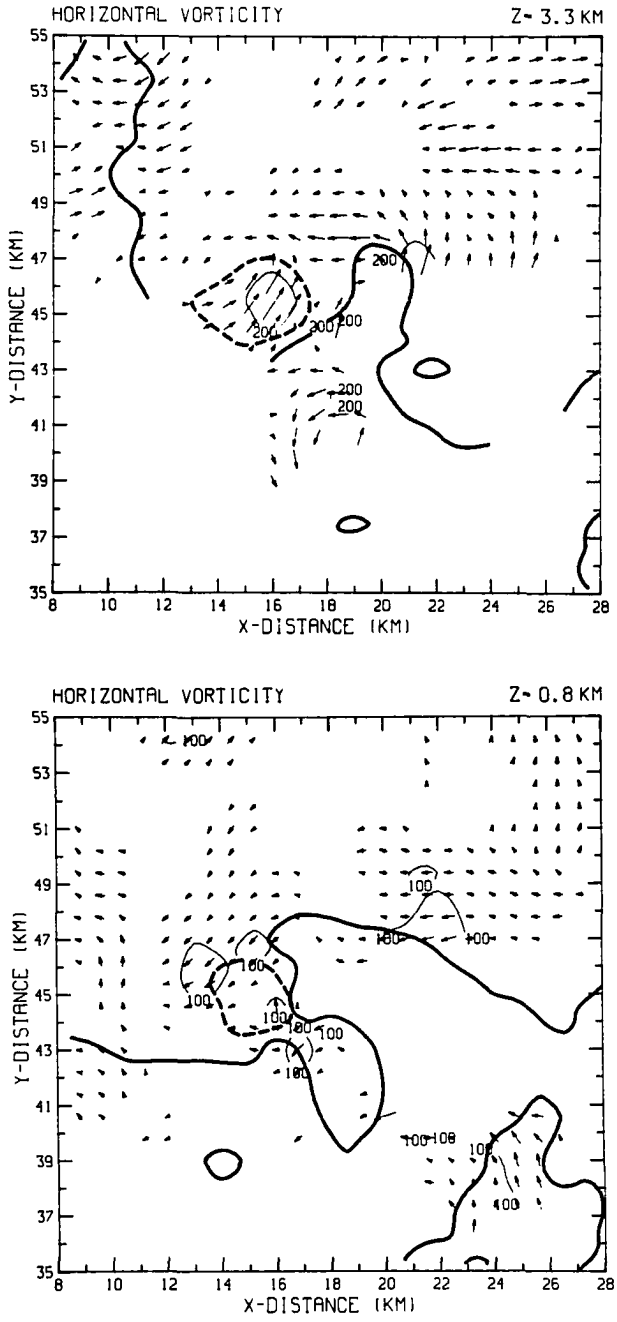

Figure 49. Horizontal vorticity, as in Fig. 34, except for tornadic stage in Oklahoma City thunderstorm (1420 CST). (z=0.8, 3.3 km)

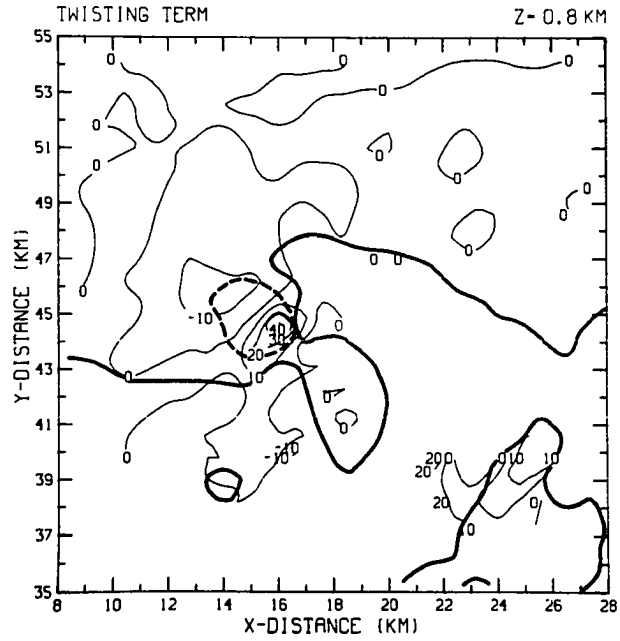

Figure 50. Vertical vorticity generation by twisting term, as in Fig. 35, except for tornadic stage in Oklahoma City thunderstorm (1420 CST). (z=0.8 km)

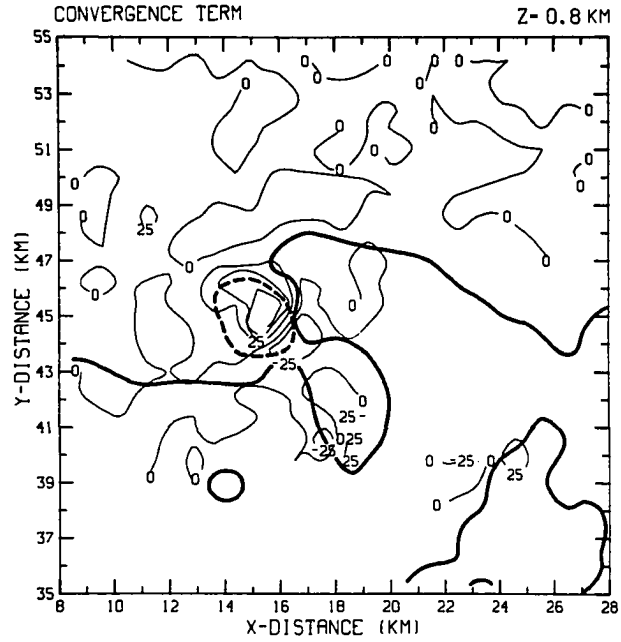

Figure 51. Vertical velocity amplification by the convergence term, as in Fig. 36, except for tornadic stage (1420 CST) in Oklahoma City thunderstorm. (z=0.8 km)

Trajectories show the mesocyclone at 0.3 km now contains approximately equal proportions of parcels from low levels ahead of the gust front and from slightly higher elevations on the storm's rear (e.g., Fig. 52). Hence, a greater flux of air into the mesocyclone from the lower right flank accompanied tornadogenesis. Moreover, it is these parcels that reach the mesocyclone core and pass through the region of strong convergence term vorticity production. Parcels entrained behind the gust front and descending in the rear downdraft are swept farther eastward. Downdraft parcels begin with negligible vertical vorticity which becomes positive through the tilting of weak horizontal vorticity (x=15, y=43, z=0.8 km).

Summarizing, the tornadic stage exhibits increased mean mesocyclone flow convergence at low levels and in general greater local convergence (Fig. 53). Mean vorticity amplification by the convergence mechanism is greatly accelerated, while the mean generation of vorticity by twisting and the turbulent diffusion of vorticity remains unchanged (Fig. 54). The increased production associates with enhanced convergence between subsiding rainy downdraft air and inflow air from the right flank. Twisting term vorticity production dominates at higher levels and is comparable in magnitude and distribution to the Del City storm. Production relates to colocation of the vertical wind gradient and locally concentrated horizontal vorticity. Although Storm Data (Environmental Data Service, 1974) reports indicate this tornado is the most intense of those studied, mesocyclone maximum vertical vorticity, mean convergence term amplification and local (grid point) convergence term vorticity amplification are considerably less than in other storms studied herein.

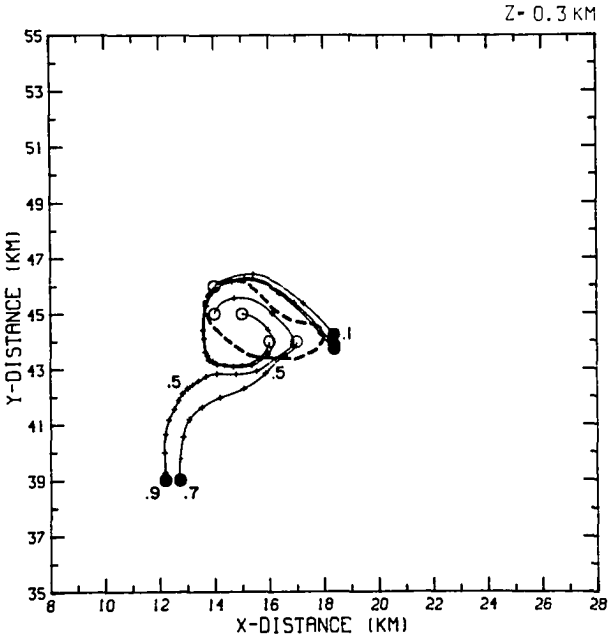

Figure 52. Parcel trajectories, as in Fig. 40, except for tornadic stage (1420 CST) in Oklahoma City thunderstorm. (z=0.3 km)

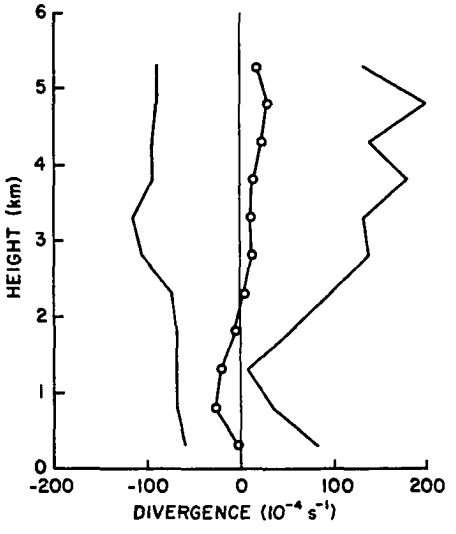

Figure 53. Vertical distribution of mean divergence and range in values, as in Fig. 44, except for tornadic stage (1420 CST) in Oklahoma City thunderstorm.

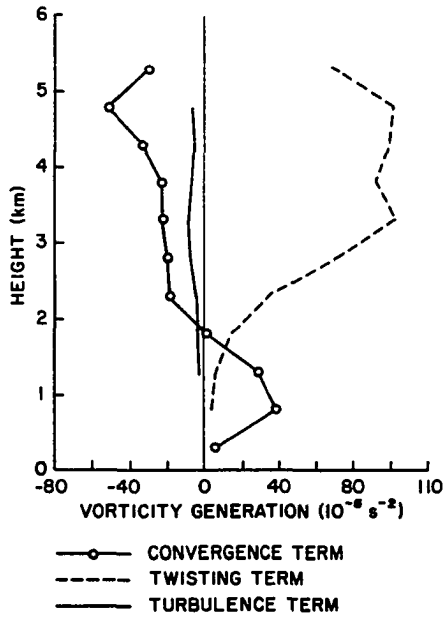

Figure 54. Vertical distribution of mean mesocyclone vertical vorticity production by the convergence, twisting, and turbulence terms, as in Fig. 45, except for the tornadic stage (1420 CST).

4. 1432 CST: Mesocyclone Decline

The storm was last sampled shortly after tornado dissipation. A closed flow pattern was evident only near ground where mesocyclone vertical vorticity and areal coverage were greatest (Figs. 55 and 56). Updraft and vertical vorticity zones have the more typical arc shape and several maxima are indicated. The close association between vorticity and updrafts of earlier times is ending. In fact, major updraft are ~3 km north of the mesocyclone center. The mesocyclone now slopes westward with height and vertical vorticity falls below the 10^{-2} s^{-1} threshold at ~2 km elevation. At all levels air parcels within the mesocyclone begin on the storm's rear. Parcels from the right flank are either lifted by intensifying gust front updraft or are swept farther to the right and ascend in updraft north of the mesocyclone.

Horizontal vorticity northeast through southeast of the mesocyclone can now be computed. Vorticity exceeds that in earliest stages (1315) and results from both wind veering and speed increases with height (Fig. 57). Inflow air horizontal vorticity tilts to the east of the mesocyclone (Fig. 58; x=30, y=48 km), but the vorticity produced is not available to the mesocyclone.

Convergence term vorticity production within the mesocyclone is primarily negative due to rear downdraft infiltration (Fig. 59). Except at 0.3 km, mesocyclone mean flow is divergent and the mean contribution to vorticity production by convergence is dissipative (Figs. 60 and 61). Mean twisting term generation, negligible at 0.8 km, becomes positive and grows with height but is insufficient to sustain the mesocirculation.

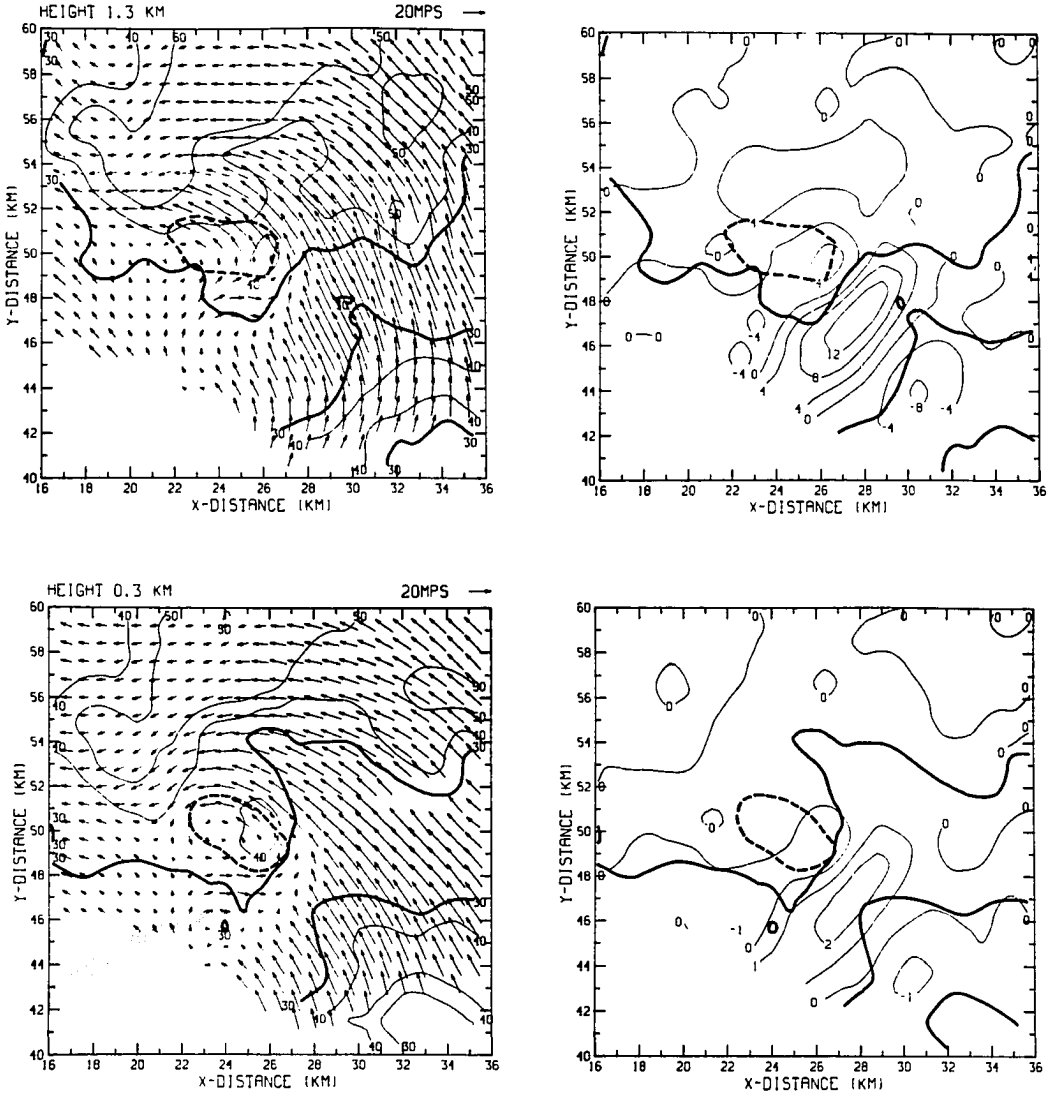

Figure 55. Storm flow, as in Fig. 32, except for post-tornadic stage (1432 CST). (z=0.3, 1.3, 3.3 km)

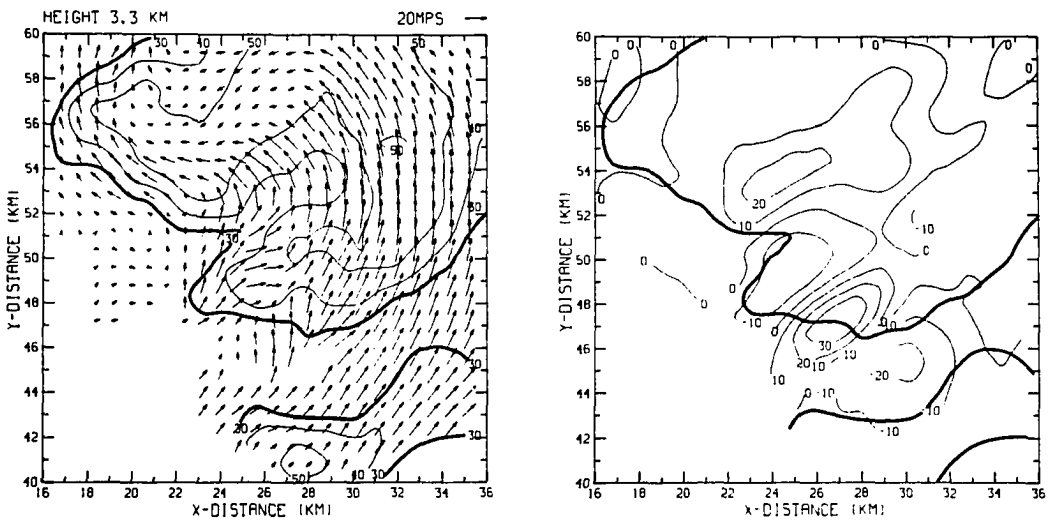

Figure 55. (Continued)

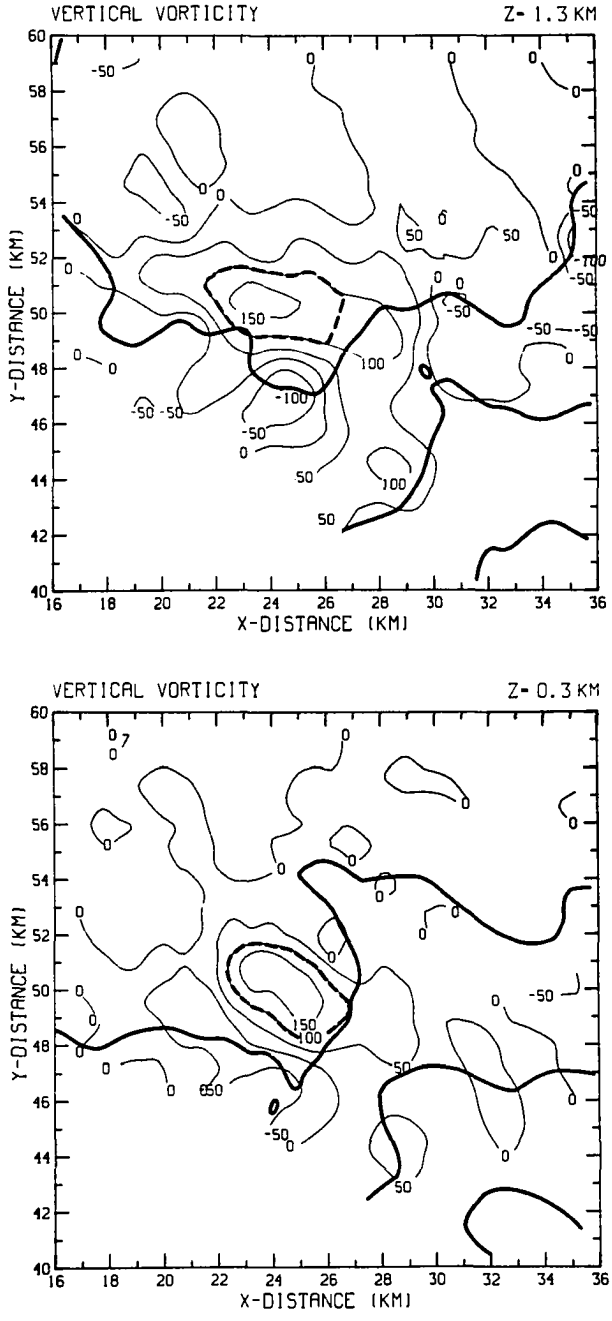

Figure 56. Vertical vorticity, as in Fig. 33, except for post-tornadic stage (1432 CST) in Oklahoma City thunderstorm. (z=0.3, 1.3, 3.3 km)

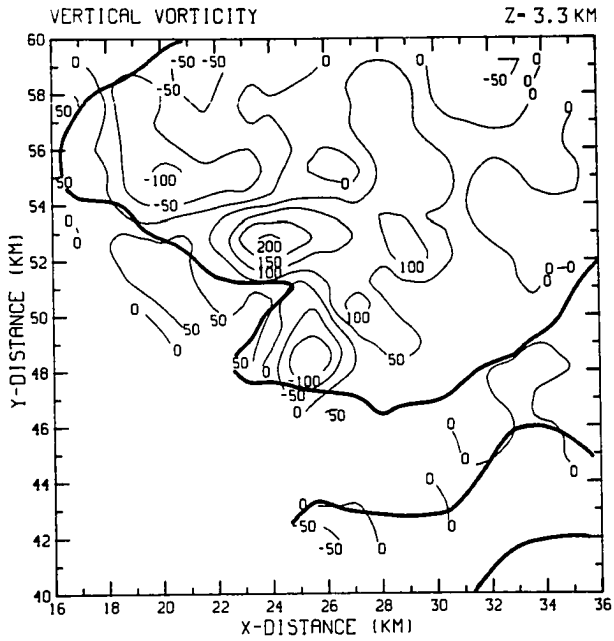

Figure 56. (Continued)

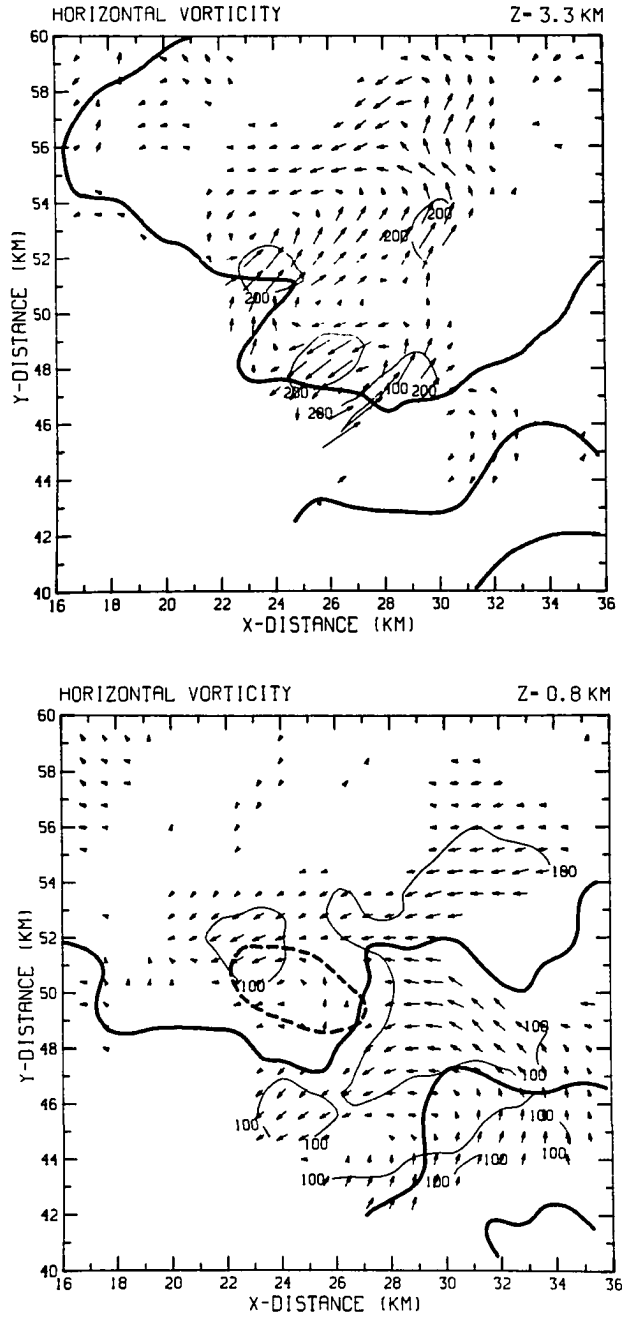

Figure 57. Horizontal vorticity, as in Fig. 34, except for post-tornadic stage (1432 CST). (z=0.8, 3.3 km)

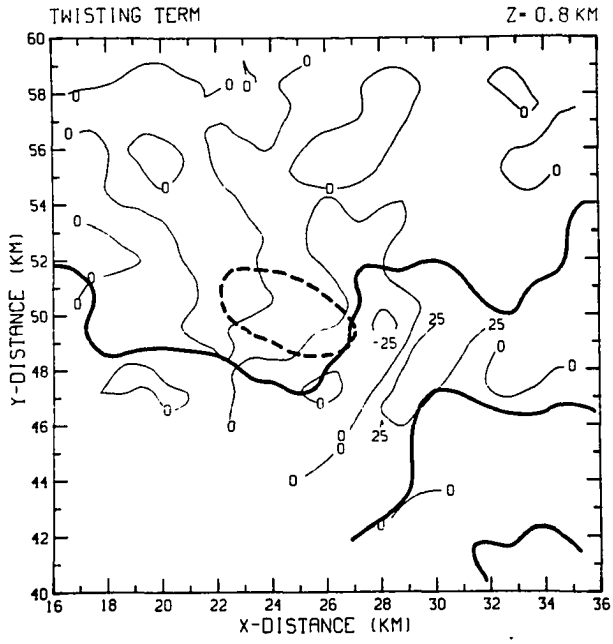

Figure 58. Vertical vorticity generation by the twisting term, as in Fig. 35, except for the post-tornadic stage (1432 CST) in the Oklahoma City thunderstorm. (z=0.8 km)

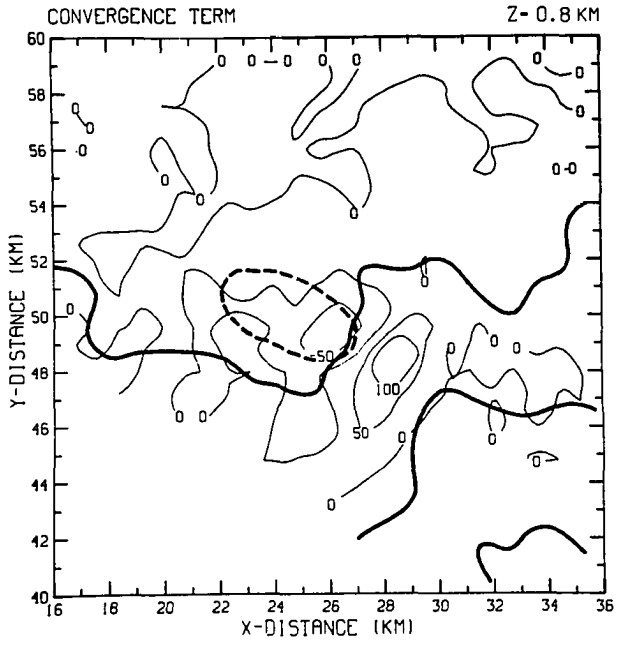

Figure 59. Vertical vorticity amplification by the convergence term, as in Fig. 36, except for the post-tornadic stage (1432 CST) in the Oklahoma City thunderstorm. (z=0.8 km)

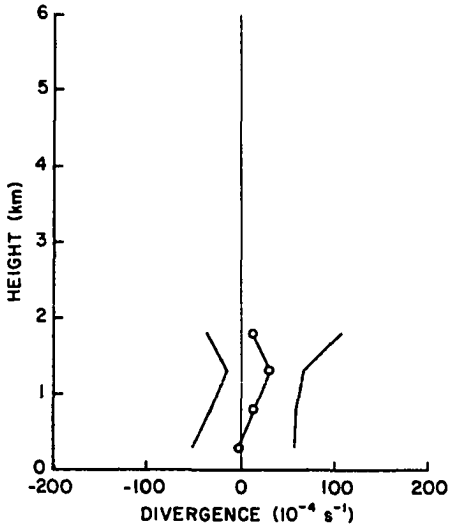

Figure 60. Vertical distribution of mean divergence and range in values, as in Fig. 44, except for the post-tornadic stage in the Oklahoma City thunderstorm (1432 CST).

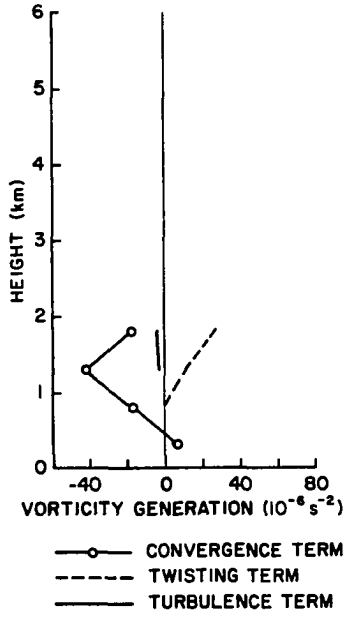

Figure 61. Vertical distribution of mean mesocyclone vertical vorticity production by the convergence, twisting, and turbulence terms, as in Fig. 45, except for the post-tornadic stage in the Oklahoma City thunderstorm (1432 CST).

Mesocyclone proximity to the edge of the data domain and the heretofore absence of scatterers to the right of the low level mesocyclone makes the Oklahoma City storm a poor candidate for thermodynamic retrieval. Of the four observational periods, the present data are thought best suited for such an analyses (Fig. 62).

Near ground a weak low pressure center coincides with the mesocyclone. High pressure is located beneath the storm interior (x=28, y=56 km) and in vicinity of the gust front (x=28, y=47, z=0.8 km). The latter region associates with strong convergence that causes the strain terms e_{11}^2 and e_{22}^2 (Chapter II) to be very large. With height the mesocyclone slopes westward and rapidly dissipates, but the mesolow tilts northward toward an elevated mesocirculation (x=24, y=52, z=3.3 km; also Fig. 56). Horizontal pressure gradient forces accelerate rear downdraft air horizontally toward the low level mesocyclone (x=26.5, y=48, z=0.8 km). Flow to the east and north is also accelerated toward the mesocyclone, but upward pressure accelerations prevent that air from every reaching the mesocyclone. Downward gradients of perturbation pressure exist within the mesocyclone and in neighboring portions of the rear downdraft. These pressure forces maintain the rear downdraft.

Temperatures at 0.8 km indicate western sections of the mesocyclone are relatively cool and the rear downdraft to be slightly cool. The region of large temperature variance near x=32, y=50 km is suspect. At higher levels temperatures appear too warm (>12°C) and indicate updraft speeds and associated gradients may be overestimated. Relative to the environment the rear downdraft is warm. Air parcel buoyancy is overcome by the vertical perturbation pressure gradient. Note also the association

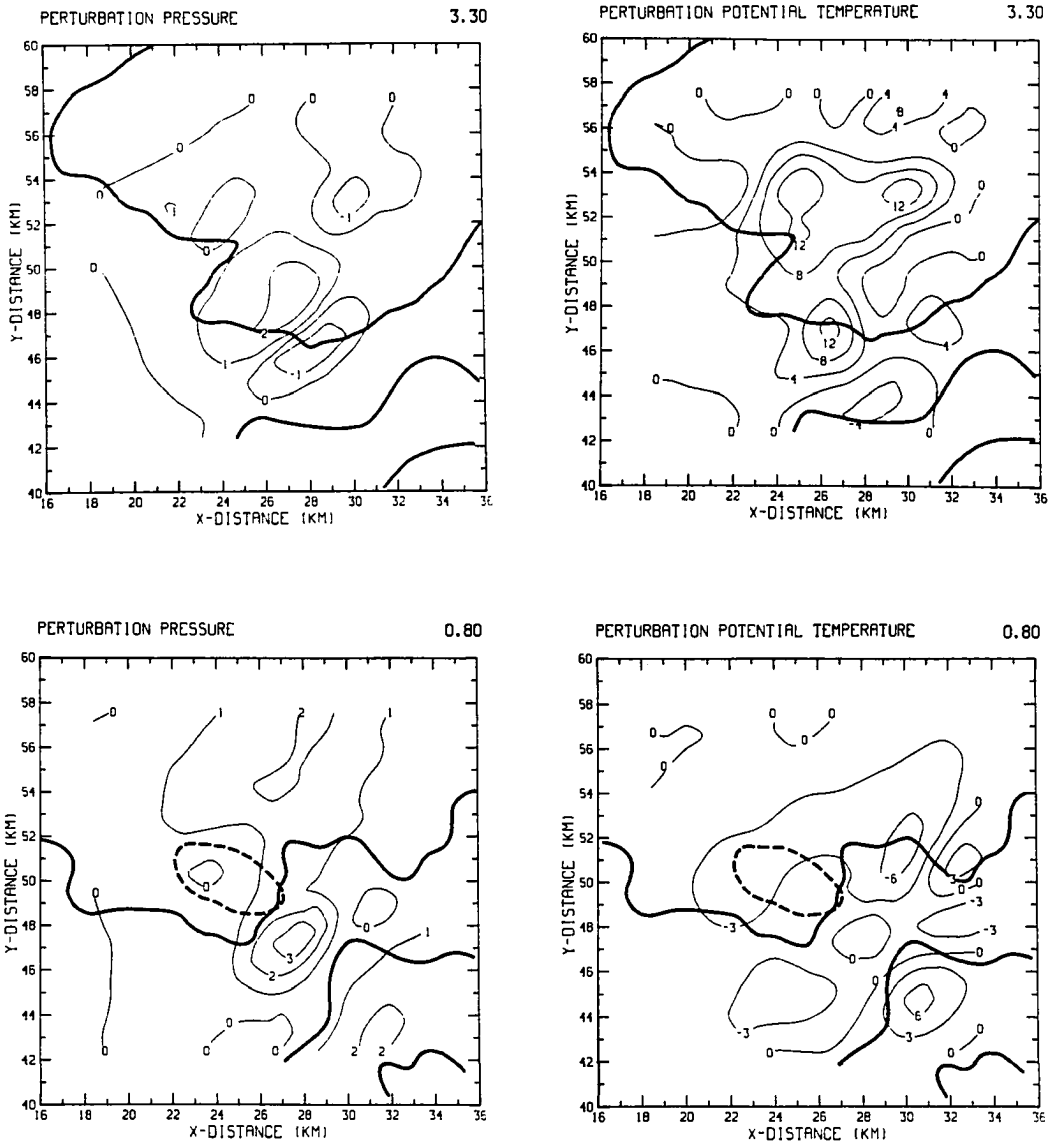

Figure 62. Retrieved perturbation potential temperature in °C and perturbation pressure in mb at 0.8 and 3.3 km elevation for the post-tornadic stage in the Oklahoma City thunderstorm (1432 CST). Heavy line denotes 30 dBZ radar reflectivity contour and heavy dashed line denotes the mesocyclone.

between cyclonic turning horizontal vorticity vectors (z=3.3, Fig. 57) and warm temperature deviations.

5. Oklahoma City Storm Summary

In the earliest stages, horizontal vorticity in right hand (inflow) quadrants of the storm exceeded maximum vertical vorticity. Horizontal vorticity was tilted into vertical vorticity at the storm's edge, and the vorticity generated was further amplified by the convergence mechanism as the inflow air encountered stronger updraft.

Mesocyclone kinematic properties computed just prior to formation of the major tornado undoubtedly were influenced by the presence of the gust front tornado and the rear downdraft behind the gust front. Curiously, air parcels from the rear downdraft filled even the lowest levels of the mesocyclone. A weak downward transport of vertical vorticity was noted. Low level vertical vorticity production was primarily by the subsequent stretching of vertically transported vorticity and vorticity generated by tilting in the rear downdraft.

During tornadogenesis, mesocyclone vorticity intensified at all levels; but maximum vertical vorticity remained aloft. Low level vertical vorticity amplification by convergence doubled. The observational evidence suggests this production resulted from greater interaction between subsiding air from more organized rainy downdraft and updraft air from the storm's lower right flank. Trajectory analyses show low level air parcels in vicinity of the tornado originated ahead of the gust front and passed through the region of vorticity amplification by

convergence. Subsiding air parcels from the storm's rear were swept to the east and through the region of strong twisting term vorticity generation.

Following tornado dissipation, mesocyclone rotation (vertical vorticity) was most intense near ground. The mesocyclone was entirely filled by air parcels that had descended on the storm's rear. Downward perturbation pressure gradients, due to mesocyclone slope and vorticity decline with height, existed within the mesocyclone and adjacent regions. The pressure gradient appeared to drive the downdraft and was necessary to force buoyant lower middle level air (3.3 km) downward. Nearer ground the mesocyclone and the rear downdraft were relatively cool.

C. The Harrah Storm of 8 June 1974

The observational record began well before and continued until well after dissipation of the single tornado produced by this 8 June thunderstorm (Fig. 63). The data have been used previously to study severe storm evolution and vertical vorticity distribution (Ray, 1976; Heymsfield, 1978; Brandes 1977b and 1978). Emphasis here is on vertical vorticity production and on the distribution of thermodynamic variables.

The long volumetric sampling period (~5 min), poor spatial sampling density (similar to the Oklahoma City thunderstorm) and small angle between the radar beams after tornado dissipation introduce some uncertainty in the analyses. Parameters most affected include the horizontal vorticity twisting term production and retrieved thermodynamic fields. Thus, only a small number of these fields, generally those from low levels and those that exhibit persistent features, are presented.

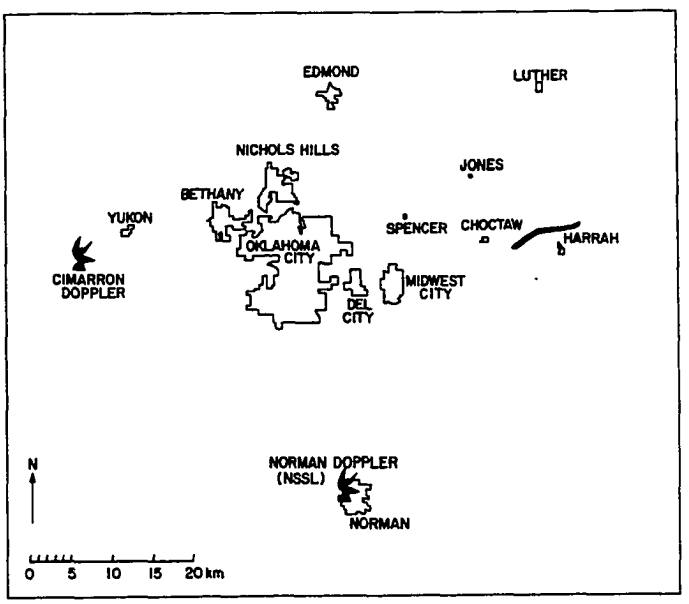

Figure 63. Map showing location of two Doppler radars and damage track of Harrah tornado, 8 June 1974.

1. 1515 CST: Early Mesocyclone Development

The initial data collection, ~30 min before tornado touchdown, sampled only trailing portions of the storm. The data show a weak developing mesocyclone where south-southwesterly flow from the storm's right rear flank converges with easterly flow from the right forward flank (x=-2.5, y=13, z=1.3 km; Fig. 64).

Vertical vorticity is predominately positive in inflow regions and, as might be expected for this early stage, relatively weak (Figs. 65 and 66). In fact, peak values fall below the threshold for defining the mesocirculation near ground. Vorticity increases with height to ~3.5 km where vertical vorticity and updrafts concentrate in arc-like zones. As in the Del City and Oklahoma City storms, the mesocyclone is displaced slightly behind (to the left of) the updraft at low levels and is displaced upwind of the updraft at higher levels.

The data also show that substantial horizontal vorticity, associated with a veering wind, exists on the storm's right rear flank (Fig. 67). Maximum values, ~300x10^{-4} s^{-1}, exceed both mesocyclone vorticity and the environmental vertical wind shear (Fig. 68) by approximately threefold. Horizontal vorticity is tilted into positive vertical vorticity to the right of the low level mesocyclone (x=-1, y=12, z=1.3 km; Fig. 69); but because the mesocyclone lies to the rear of strong updraft, vorticity generation inside the mesocyclone is mostly negative. Low level vorticity amplification by convergence (Fig. 70) is predominately positive in inflow regions. Maximum vorticity amplification occurs within and slightly ahead of the mesocyclone and exceeds upwind twisting term generation by more than a factor of two.

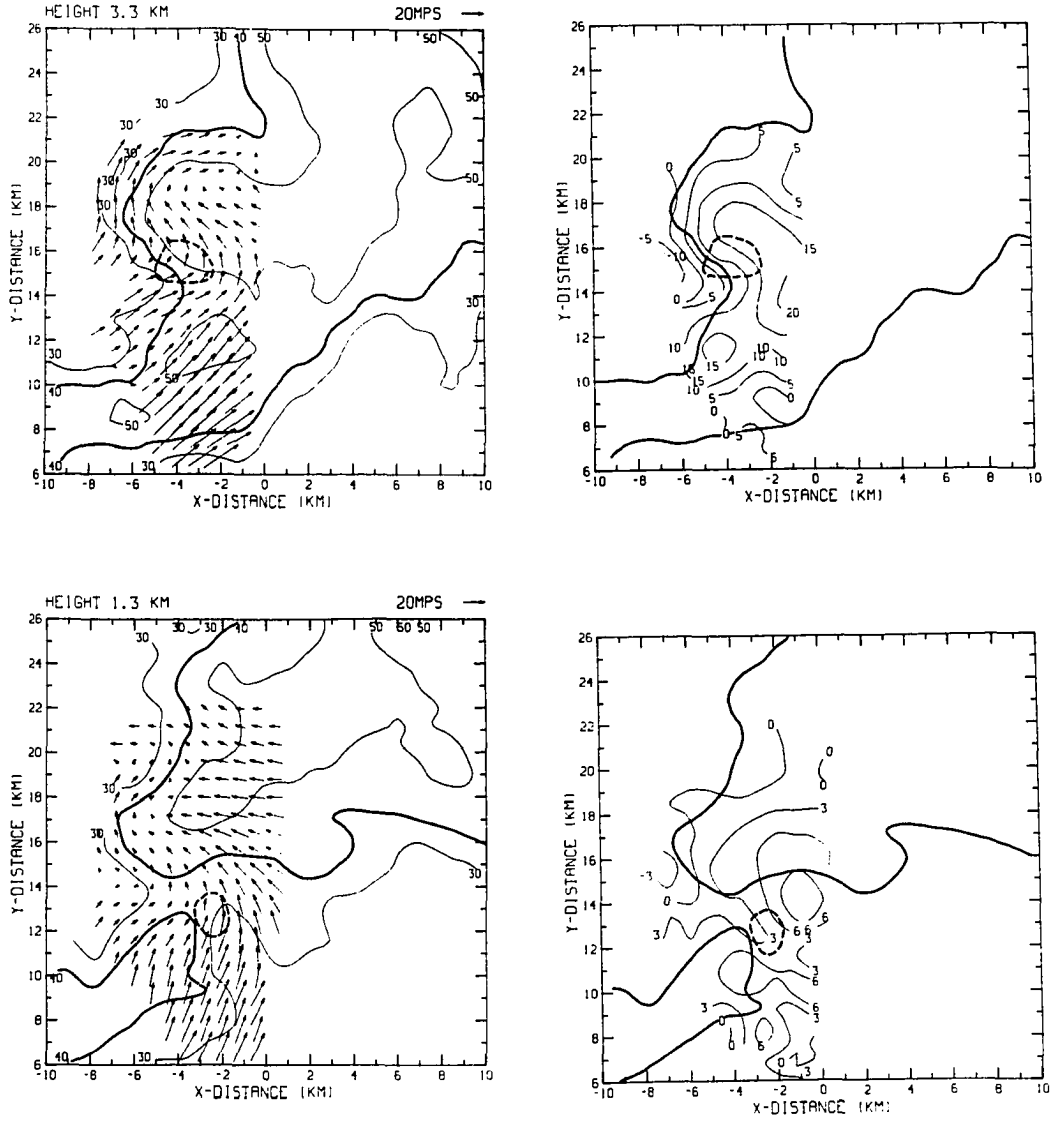

Figure 64. Wind fields early in Harrah thunderstorm (1515 CST). Left hand panels show horizontal wind (vectors) relative to the storm [Cimarron radar reflectivity (dBZ) superimposed and 40 dBZ contour accentuated]. Right hand panels show vertical wind distribution with the 40 dBZ reflectivity contour superimposed. Distances are from the Norman radar and heights (upper left) are AGL. A horizontal wind vector 1 km in length equals 20 m s^{-1}. The mesocyclone is indicated by a heavy dashed line. Storm motion is from 230° at 18 m s^{-1}. (z=1.3, 3.3 km)

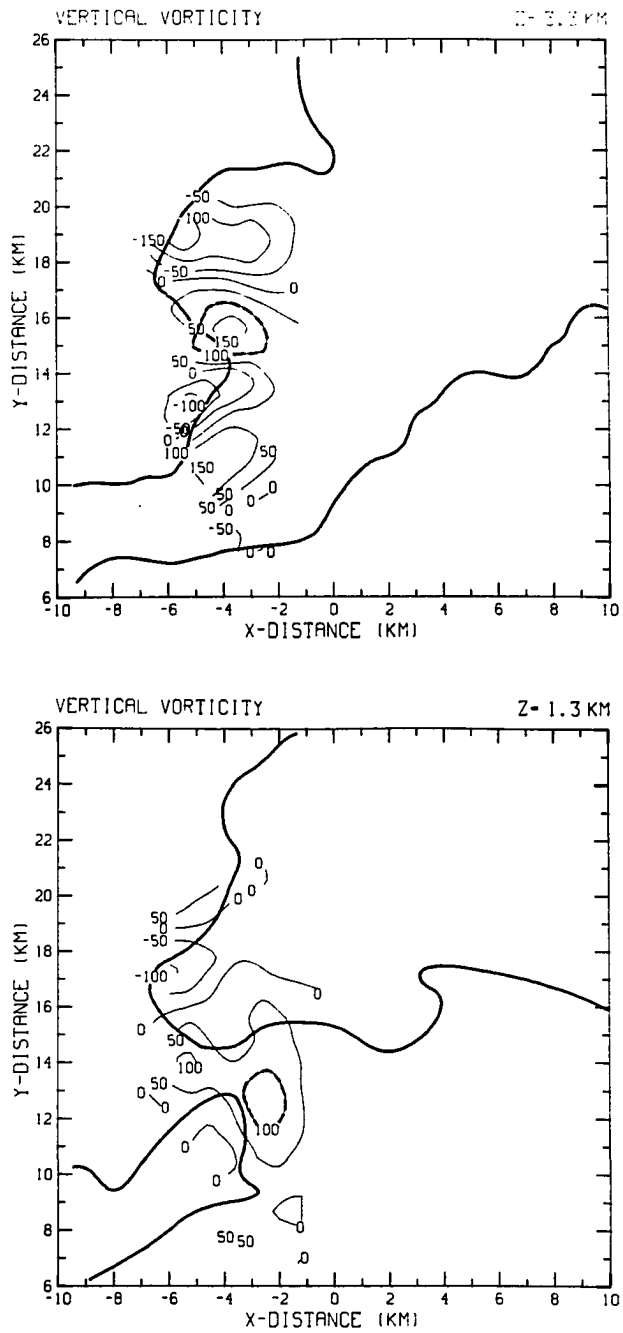

Figure 65. Vertical vorticity at 1.3 and 3.3 km elevation early in Harrah thunderstorm (1515 CST). Contouring interval is 50×10^{-4} s^{-1}. Heavy line denotes 40 dBZ radar reflectivity contour and heavy dashed line denotes the mesocyclone.

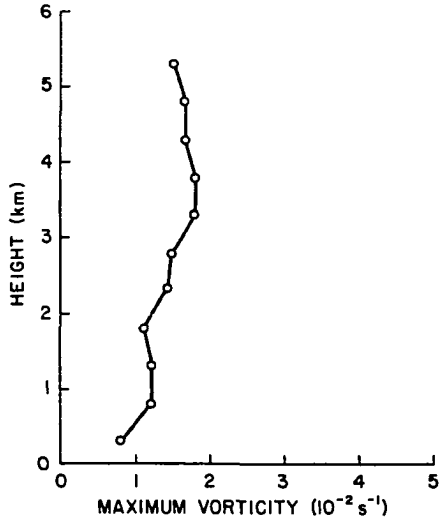

Figure 66. Vertical distribution of maximum vertical vorticity early in Harrah mesocyclone (1515 CST).

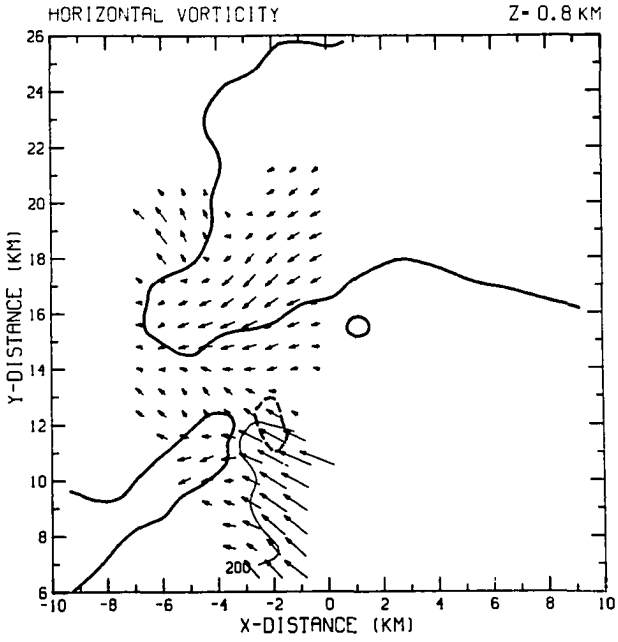

Figure 67. Horizontal vorticity at 0.8 km early in Harrah thunderstorm (1515 CST). Local rotation axis in plane shown vectorally. Only vorticity values $\geq 50 \times 10^{-4}$ s^{-1} plotted. Contouring interval 200×10^{-4} s^{-1}. Heavy line denotes 40 dBZ radar reflectivity contour and heavy dashed line denotes mesocyclone.

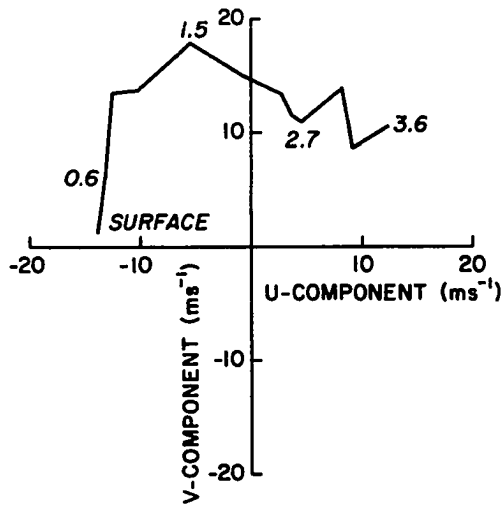

Figure 68. Storm relative hodograph for environmental sounding released at Norman, Oklahoma (1537 CST) on 8 June 1974. Heights are above mean sea level (MSL), ground height is 0.36 km. Winds are plotted at 300 m increments with select heights in km indicated.

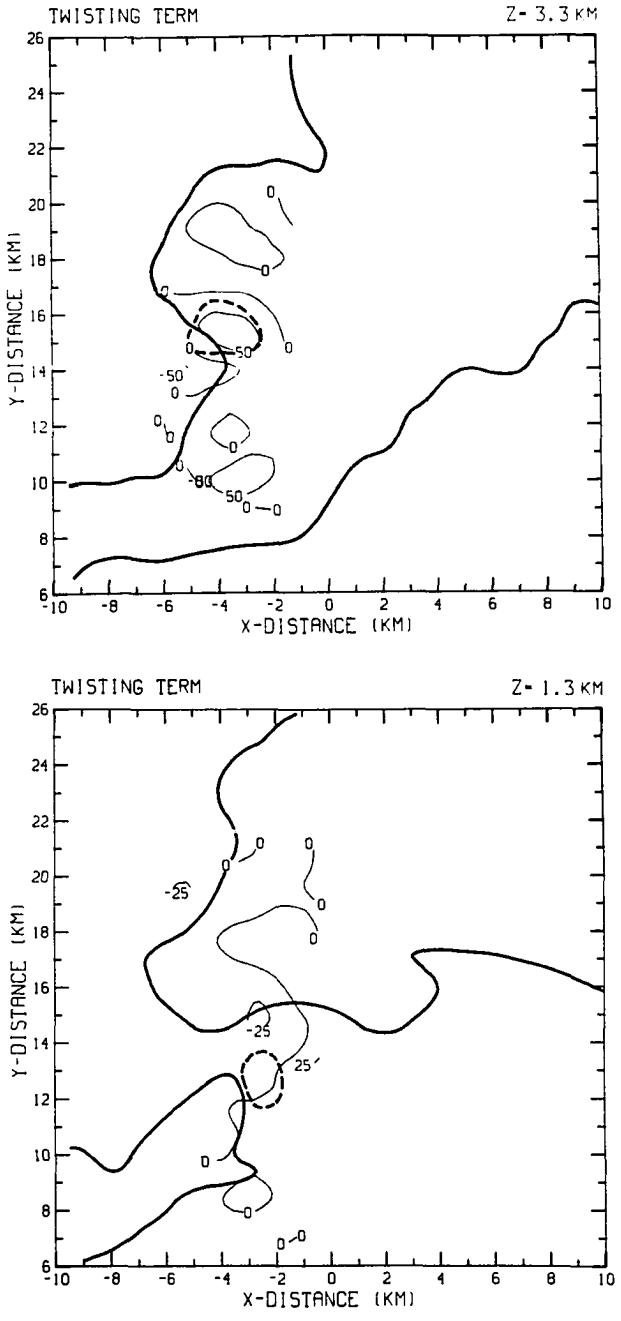

Figure 69. Vertical vorticity generation by twisting term at 1.3 and 3.3 km elevation early in Harrah thunderstorm (1515 CST). Contouring intervals are 25 and 50x10^{-6} s^{-2}. Heavy line denotes 40 dBZ radar reflectivity contour and heavy dashed line indicates mesocyclone.

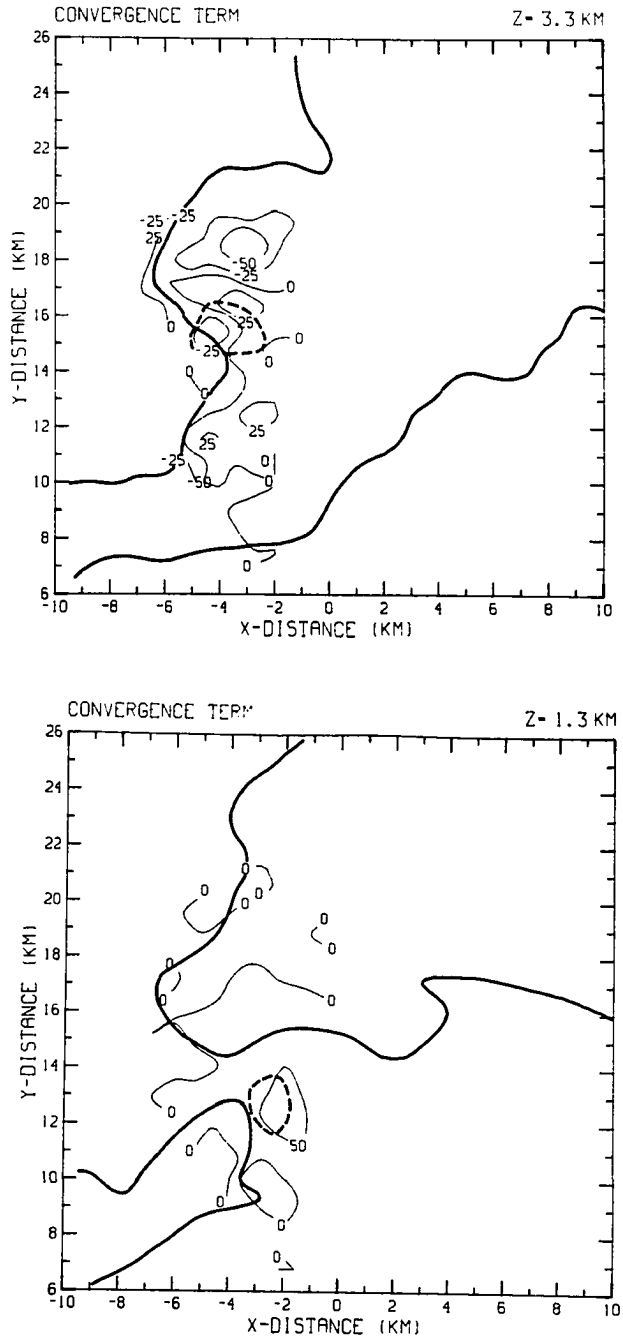

Figure 70. Vertical vorticity amplification by the convergence term at 1.3 and 3.3 km elevation early in Harrah thunderstorm (1515 CST). Contour intervals are 25 and 50x10-6 s^{-1}. Heavy lines denotes 40 dBZ contour and dashed line denotes mesocyclone.

Thus, in all storms studied the twisting mechanism is important upwind of developing mesocyclones; but it is the convergence term acting on tilted vorticity that largely determines the location of the mesocyclone.

Horizontal vorticity vectors turn cyclonically above 1.3 km and are tilted by the vertical wind gradient across the mesocyclone into positive vorticity. Convergence term vorticity amplification in the elevated mesocyclone is weak. Thus, twisting maintains the middle level circulation.

Mesocyclone grid point convergence is entirely negative (convergent) near ground (Fig. 71). Relative to later developmental stages, the range in values is small. Mean vertical vorticity production by twisting and convergence and the turbulent diffusion of vorticity are summarized in Fig. 72.

2. 1530 CST: Mesocyclone Intensification and Appearance of the Incipient Tornado

Between 1515 and 1530 the mesocyclone intensified (Figs. 73 and 74) and a closed wind pattern with a southward-extending gust front (approximately in vicinity of the 40 dBZ contour, z=1.3 km) evolved. Low level updraft and vertical vorticity were concentrated in similar arcs near the front. Unsmoothed radial velocity measurements gathered between 1.5 and 3 km elevation bespeak a developing tornado near the mesocyclone center.

Radar scatterers are insufficient in eastern storm quadrants at low levels to resolve the three-dimensional wind flow. Consequently, there is some uncertainty concerning kinematic properties of inflow air;

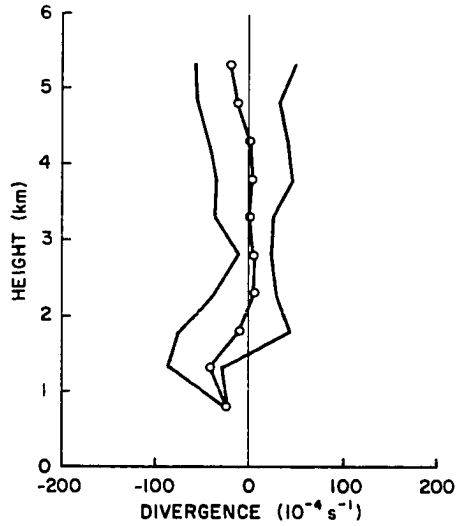

Figure 71. Vertical distribution of mean mesocyclone divergence (central curve) and range in grid point values (outer curves) early in Harrah thunderstorm (1515 CST).

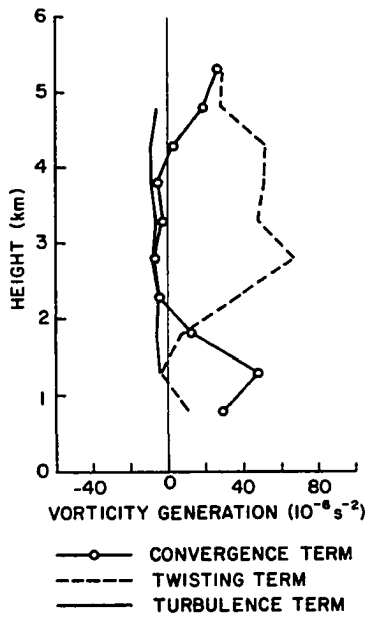

Figure 72. Vertical distribution of mean mesocyclone vertical vorticity production by the convergence, twisting, and turbulence terms, early in Harrah thunderstorm (1515 CST).

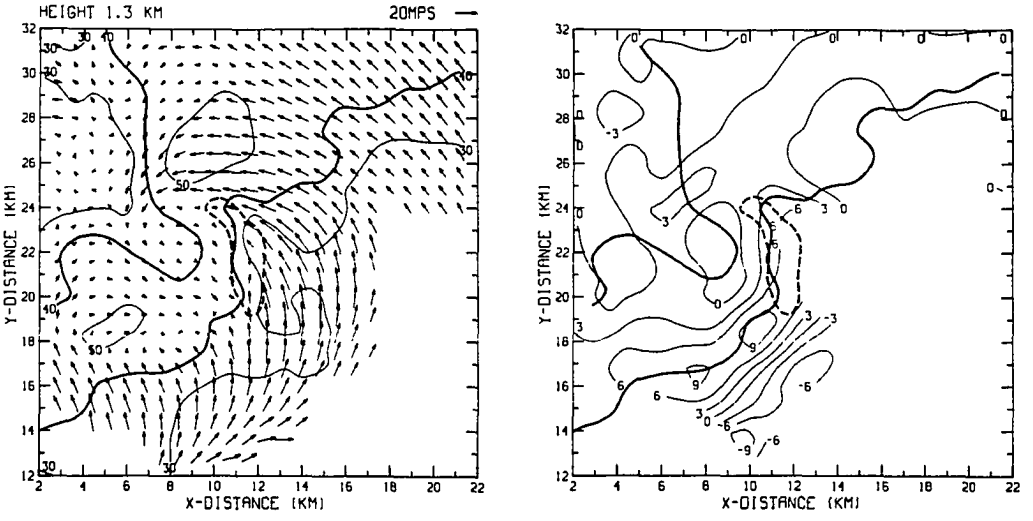

Figure 73. Storm flow, as as in Fig. 64, early in Harrah thunderstorm (1530 CST). (z=1.3 km)

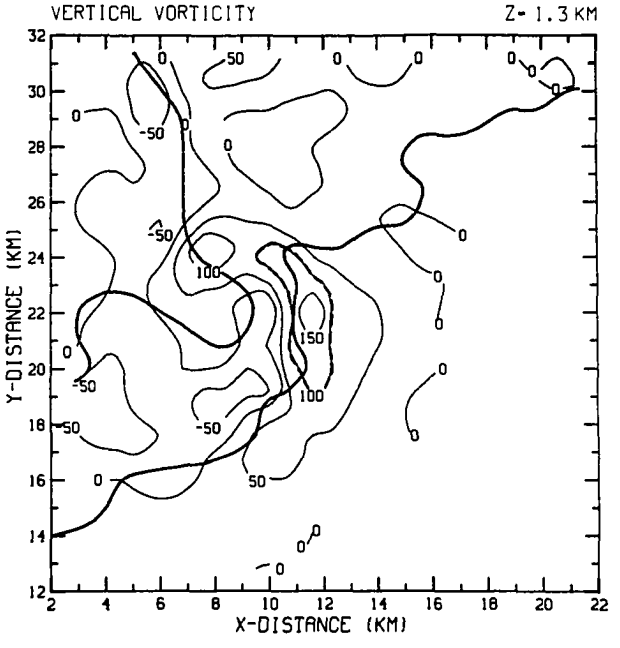

Figure 74. Vertical vorticity, as in Fig. 65, early in Harrah thunderstorm (1530 CST). (z=1.3 km)

and the spatial distribution of the mechanisms affecting vertical vorticity are not presented. Observations do show that mesocyclone vertical vorticity had intensified at all levels and that vorticity still increases with height (Fig. 75). Mesocyclone wind flow is entirely convergent below 2 km and stays convergent in the mean to ~4 km (Fig. 76). The range in grid point values continues to be small. Mean vertical vorticity amplification by convergence has multiplied with the strengthening of updraft in vicinity of the mesocyclone, but vorticity generation by twisting has diminished (Fig. 77). Hence, the growth of mesocyclone vertical vorticity is most readily attributed to the convergence term.

3. 1543 CST: Further Mesocyclone Intensification

Prominent morphological changes observed just prior to tornado touchdown include an enlargement of the mesocirculation and continued growth of vertical vorticity (Figs. 78 and 79).[8] Radar reflectivity has increased and widespread rainy downdrafts have developed in the storm's interior (near x=20, y=33, z=1.3 km). Unsmoothed radial velocity measurements indicate that the incipient tornado had intensified and now extended from 1 to 5 km.

Horizontal vorticity in inflow areas to the right of the mesocyclone has declined from 1515 values to 150×10^{-4} s^{-1} (Fig. 80). Weak horizontal vorticity in western portions of the mesocyclone (x=19, y=28, z=1.3 km) implies that air parcels there have lost much of their initial

[8] A cursory damage survey suggests the tornado touched ground between 1546 and 1559.

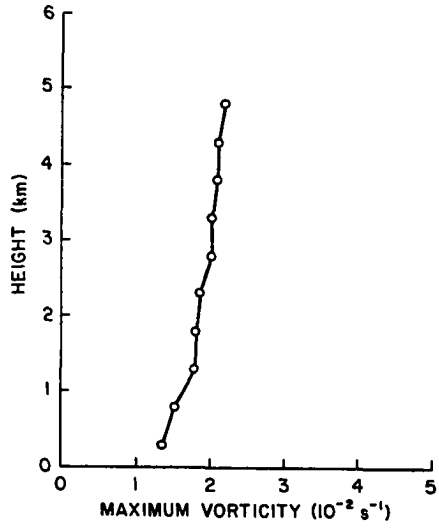

Figure 75. Vertical distribution of maximum vertical vorticity in Harrah mesocyclone at 1530 CST.

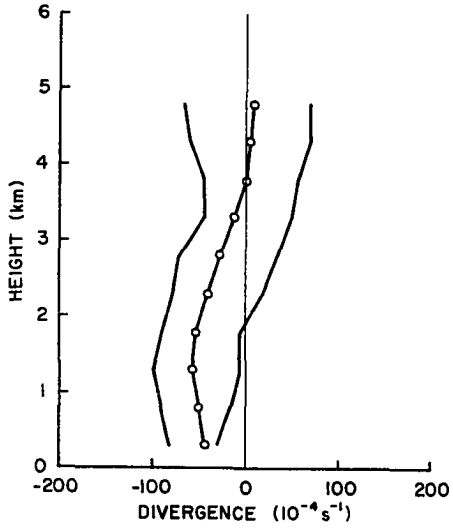

Figure 76. Vertical distribution of mean divergence and range in values, as in Fig. 71, except for 1530 CST in Harrah thunderstorm.

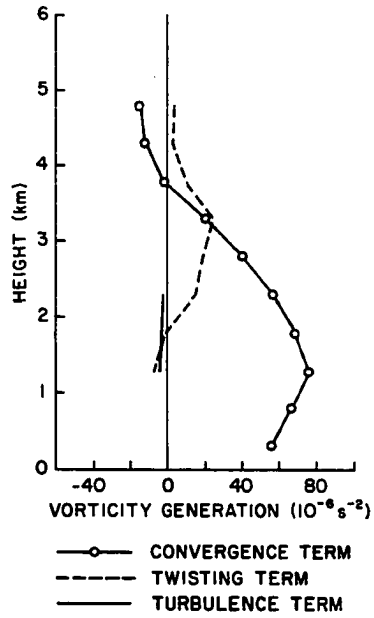

Figure 77. Vertical distribution of mean mesocyclone vertical vorticity production by the convergence, twisting, and turbulence terms, as in Fig. 72, except for 1530 CST in Harrah thunderstorm.

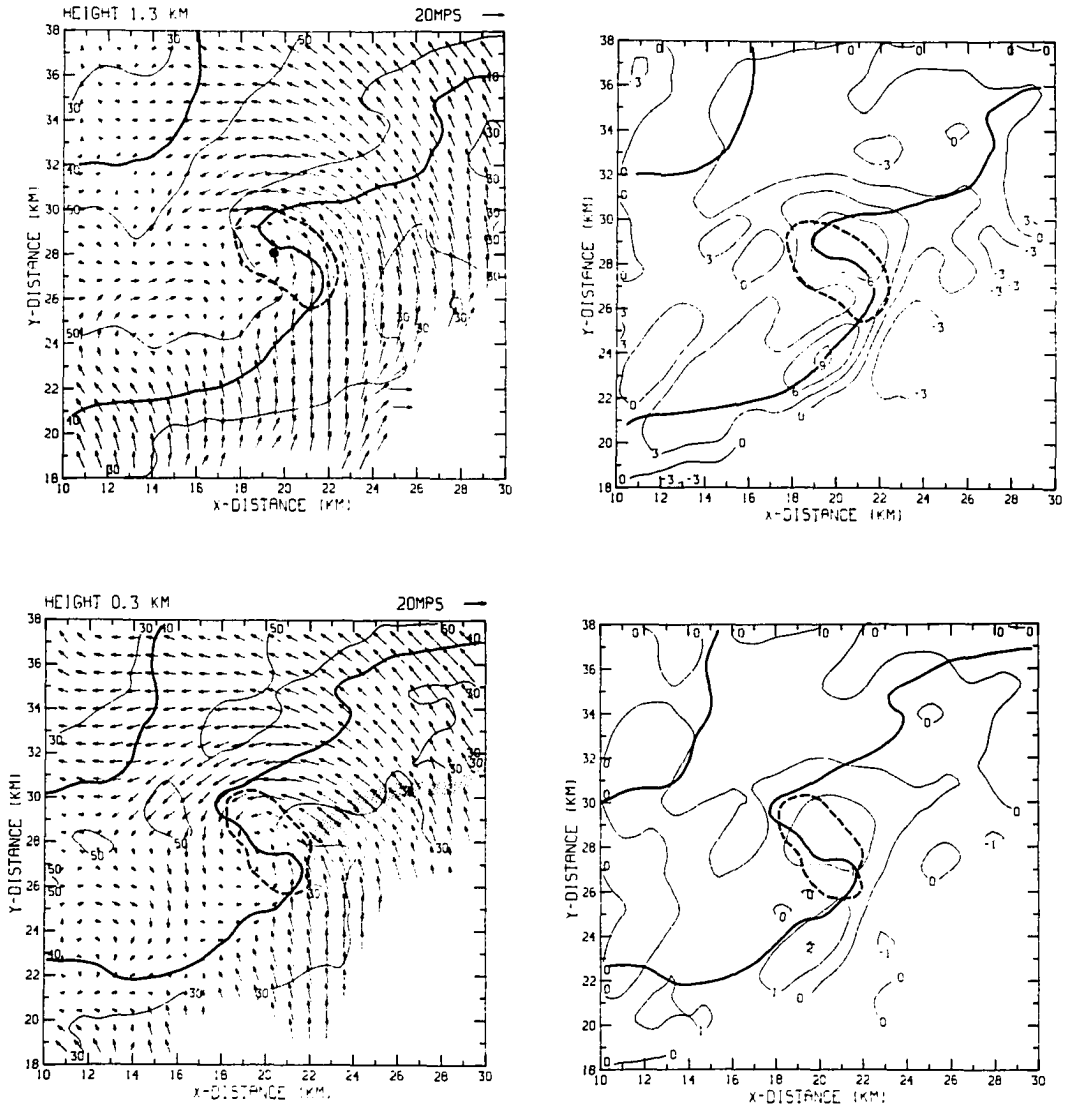

Figure 78. Storm flow, as in Fig. 64, except for pretornadic stage in Harrah thunderstorm (1543 CST). Tornado damage path stippled. Incipient tornado shown by dot. (z=0.3, 1.3, 3.3 km)

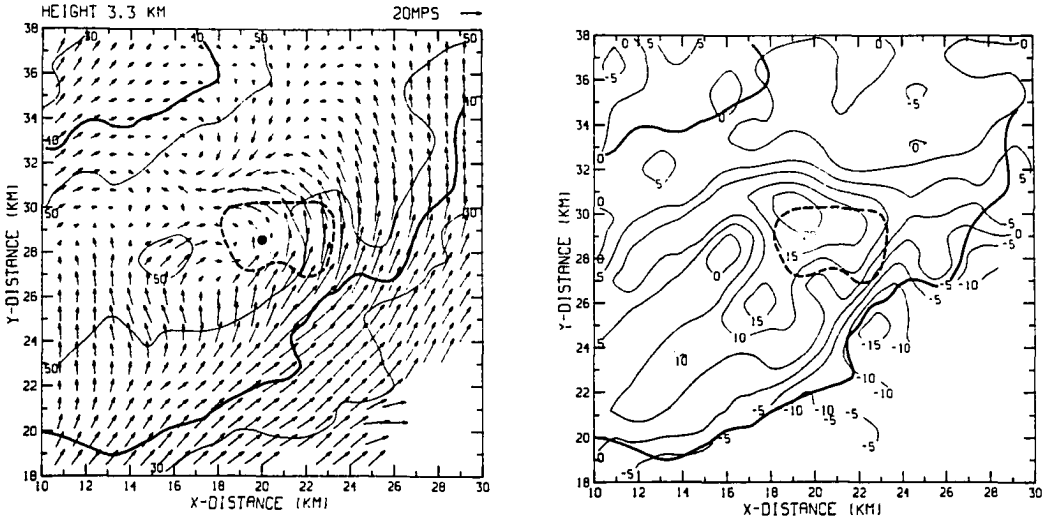

Figure 78. (Continued)

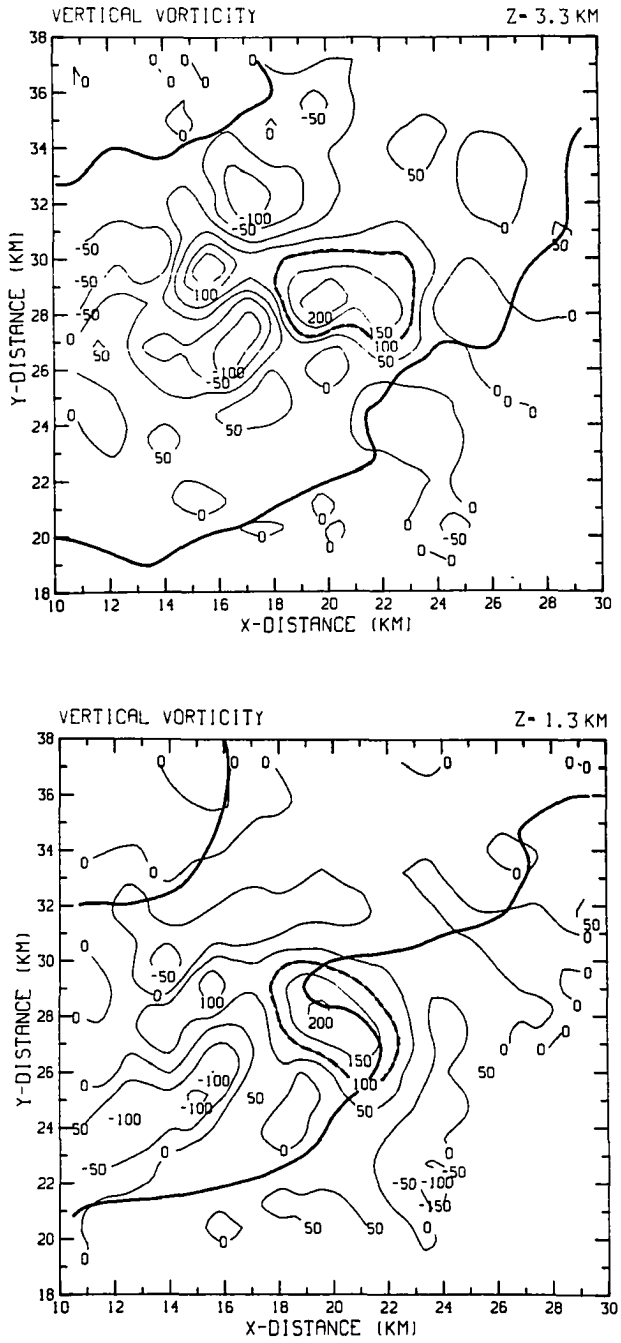

Figure 79. Vertical vorticity, as in Fig. 65, except for pretornadic stage in Harrah thunderstorm (1543 CST).

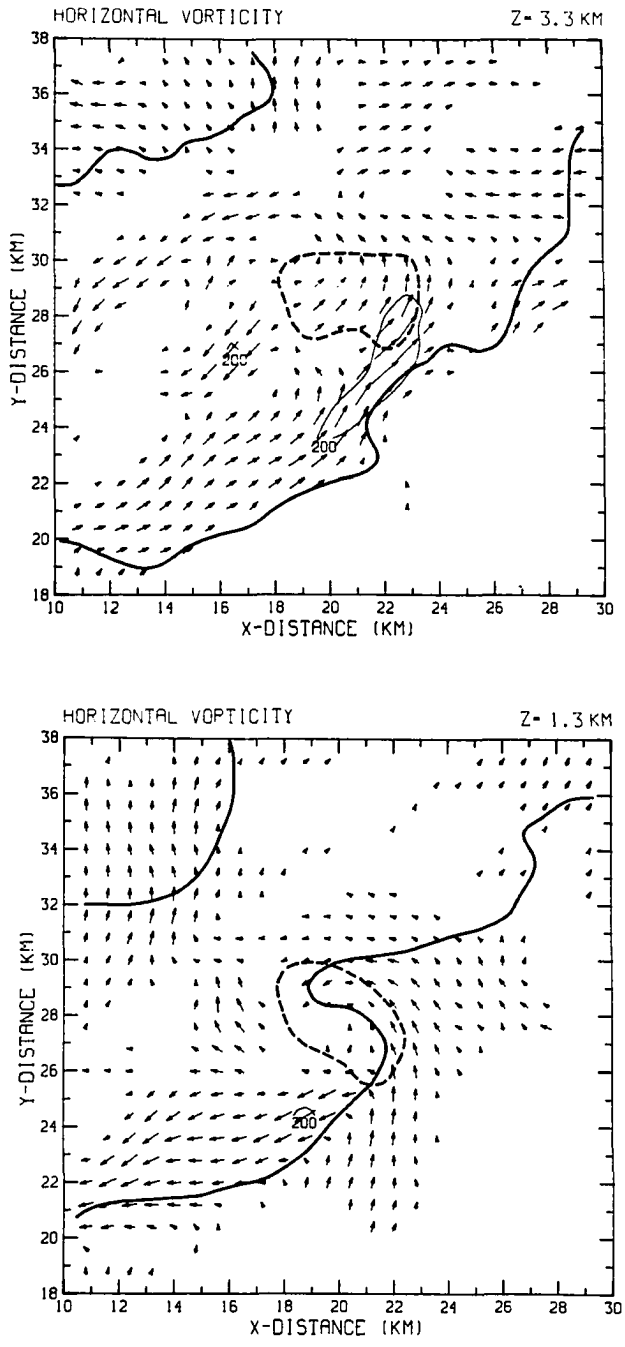

Figure 80. Horizontal vorticity, as in Fig. 67, except for pretornadic stage in Harrah thunderstorm (1543 CST). (z=1.3 and 3.3 km)

horizontal vorticity. Horizontal vorticity tilts into positive vertical vorticity in the southeastern half of the mesocyclone (z=1.3 km, Fig. 81); but strongest generation, rates to 35×10^{-6} s^{-2}, extends from 3 km to the right of the mesocyclone core southwestward ahead of the gust front. Convergence term vorticity amplification at low levels is a maximum near the incipient tornado and continues weakly within the gust front updraft (Fig. 82). In general, vorticity concentration by convergence is shifted downwind from the maximum twisting region. Vorticity amplification by convergence within the mesocyclone exceeds upwind twisting term generation by approximately threefold. Moreover, it is only within the mesocyclone that significant amplification of vorticity occurs.

The history of select air parcels in vicinity of the mesocyclone at 1.3 km is shown in Fig. 83. Parcels close-by the mesocyclone core originate at lower elevations on the right flank. All parcels in vicinity of the mesocyclone pass through the elongated region of strong twisting.

Between 1.3 and 3.3 km, the principal updraft slopes northwestward and concentrated horizontal vorticity is rapidly tilted into vertical vorticity over all but northern sections of the mesocyclone. Peak production roughly coincides with the incipient tornado. The data also show rapid vorticity amplification by convergence just to the left of the proto-tornado. While twisting seems to explain the growth of vertical vorticity at the southern edge of the elevated mesocyclone, both twisting and convergence are deemed important for tornado development.

The vertical distribution of maximum vertical vorticity (Fig. 84) shows continued strengthening, particularly below 4 km (c.f., Fig. 75).

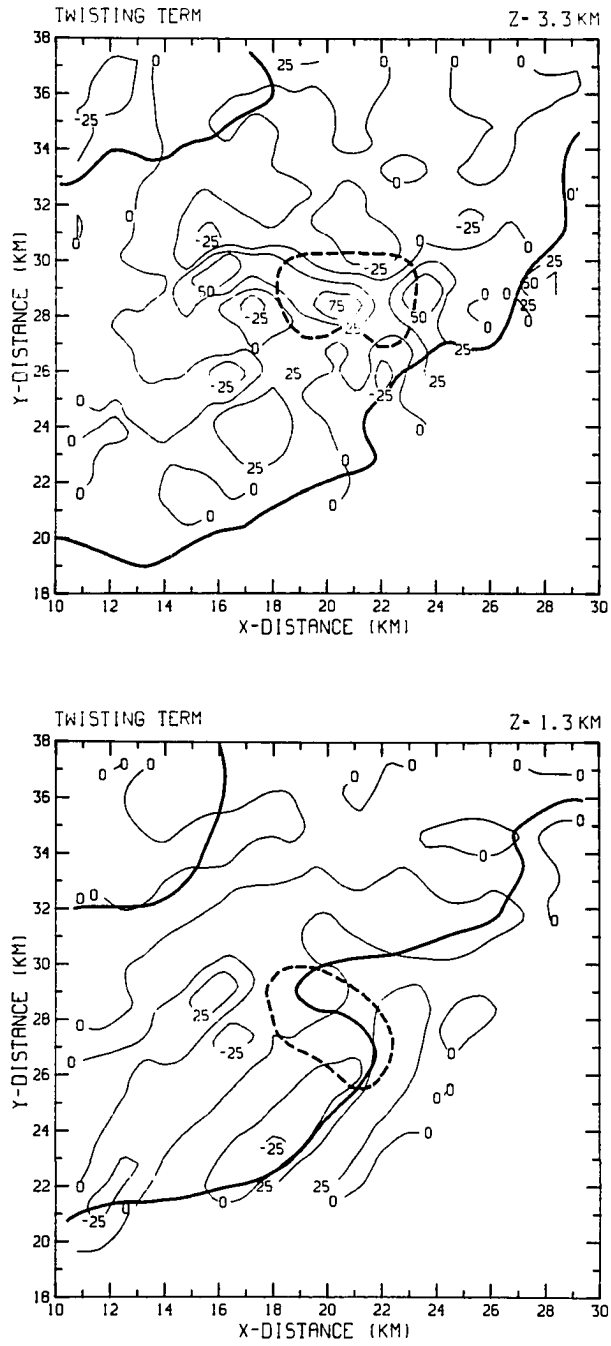

Figure 81. Vertical vorticity generation by twisting term, as in Fig. 69, except for pretornadic stage in Harrah thunderstorm (1543 CST).

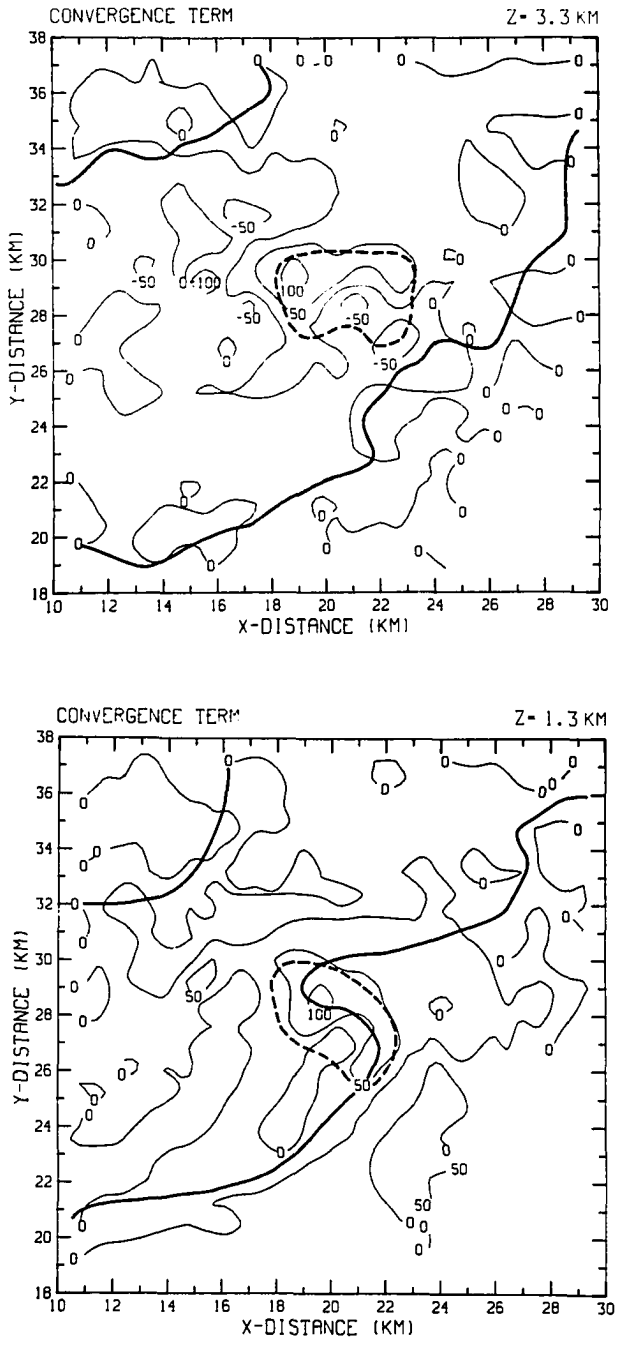

Figure 82. Vertical vorticity amplification by the convergence term, as in Fig. 70, except for pretornadic stage in Harrah thunderstorm (1543 CST).

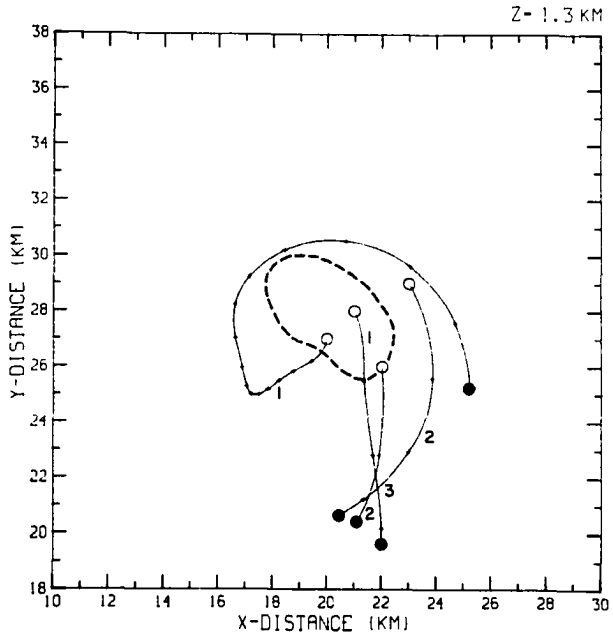

Figure 83. Parcel trajectories in the Harrah storm computed from synthesized wind fields prior to tornadogenesis (1543 CST). Initial parcel locations shown by dots and final locations (all Z=1.3 km) shown by circles. Parcel motion projected on a horizontal plane. Tick marks give positions at 2 min intervals. Select parcel heights (km) and location of mesocyclone at 1.3 km shown by heavy dashed line.

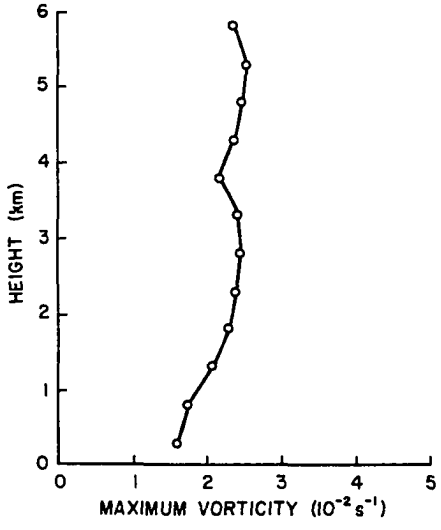

Figure 84. Vertical distribution of maximum vertical vorticity prior to tornadogenesis in Harrah mesocyclone (1543 CST).

Clearly, the low level growth of vorticity does not result from lowering of strong upper level vertical vorticity but represents production of new vorticity. Mesocyclone flow is convergent in the mean at all heights (Fig. 85). However, a small region of divergent flow, behind the gust front, now exists at all levels in the mesocyclone and has widened the range in grid point divergence values. The vertical distribution of mean mesocyclone vorticity production by twisting is much like that at 1530 (Fig. 86). The convergence term has become positive throughout the vertical depth considered and remains the dominant factor in vertical vorticity growth near ground.

Retrieved thermodynamic variables for this pretornadic stage are displayed in Fig. 87. Cool temperatures at 1.3 km elevation reside downwind of the principal updraft, within the mesocyclone and behind the gust front (x=20, y=25 km). A strong temperature gradient exists in vicinity of the gust front. "Noisy" temperatures in poorly sampled inflow regions on the right flank (x=26, y=30 km) are suspect. The storm interior (i.e., the mesocyclone and the principal updraft) becomes warm at 3.3 km. Updraft error accumulation and neglect of water vapor perturbations probably accounts for some of this warming; note particularly the region between gust front updraft and the downdraft at x=23, y=25 km.

Retrieved pressures show a mesolow (<-1.5 mb) that lies in the southeastern quadrant of the mesocyclone and a low pressure trough that extends along the vortical zone ahead of the gust front. Pressure gradients, particularly to the northeast and the southeast, accelerate flow from the right flank toward the mesocyclone and the major updraft.

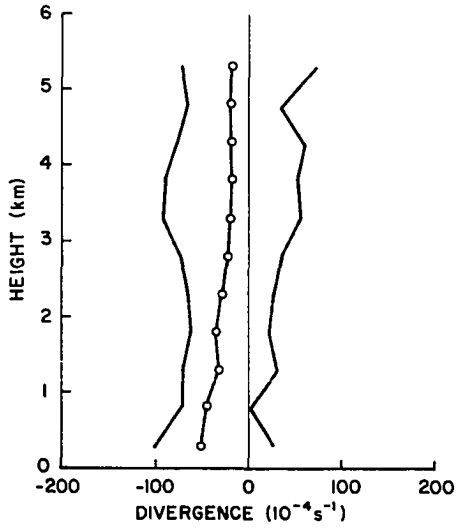

Figure 85. Vertical distribution of mean divergence and range in values, as in Fig. 71, except for pretornadic stage in Harrah thunderstorm (1543 CST).

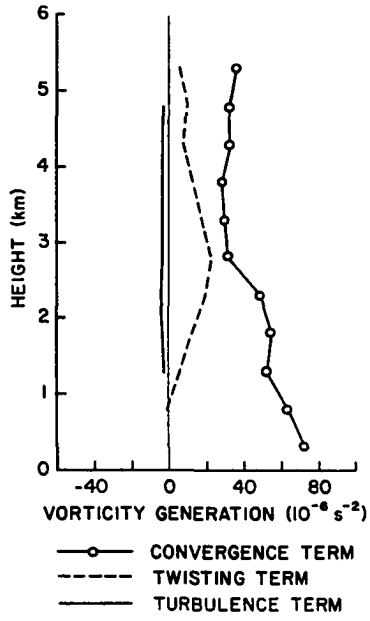

Figure 86. Vertical distribution of mean mesocyclone vertical vorticity production by the convergence, twisting, and turbulence terms, as in Fig. 72, except prior to tornadogenesis in Harrah thunderstorm (1543 CST).

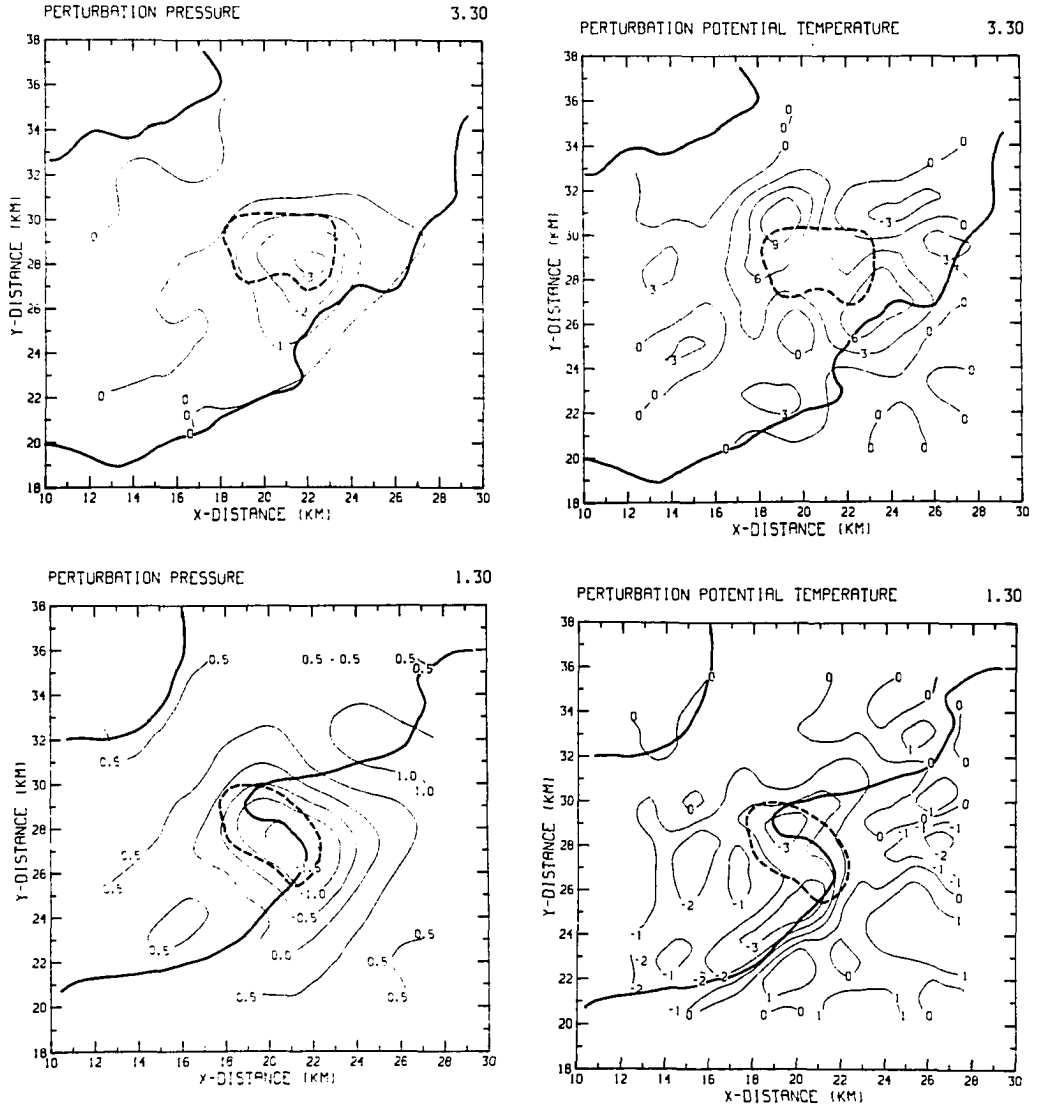

Figure 87. Retrieved perturbation potential temperature (°C) and perturbation pressure (mb) at 1.3 and 3.3 km elevation prior to tornadogenesis in the Harrah thunderstorm (1543 CST). Heavy line denotes 40 dBZ radar reflectivity contour and dashed line denotes mesocyclone.

The pressure deficit decreases to <-3 mb at 3.3 km--approximately the height at which vertical and three-dimensional vorticity were a maximum. As in the Del City storm, the vertical gradient of perturbation pressure provides the lift for nonbuoyant air at 1.3 km.

4. 1553 CST: Tornadic Stage

Conspicuous changes in storm flow, vorticity distribution and vertical vorticity production occurred during the transition to the tornadic state. Updraft north of the tornado (x=24, y=33 km; Fig. 88), where inflow air from the right flank merges with outflow air from an intense rainy downdraft (near x=22, y=35 km), and mesocyclone vorticity below 4 km (Figs. 89 and 90) have increased abruptly. Updraft and vertical vorticity zones are more elongated and perturbed than earlier. The tornado lies within the vertical wind gradient between the principal updraft and the downdraft that is developing behind the gust front (x=25, y=31, z=1.3 km). The perturbed updraft and vertical vorticity zones are nearly wrapped about the downdraft. The complex structure of these features introduces scales not well resolved with the coarse Doppler measurements.

Disruption of the low level flow has rearranged and increased horizontal vorticity components in northern sections of the mesocyclone and on the storm's right flank (maximum values 240×10^{-4} s^{-1}, Fig. 91). Horizontal vorticity becomes negligible near the tornado and is small at the terminus of the rear downdraft.

The transformation to the tornadic state has increased the complexity of vorticity generation by twisting. Rapid vorticity

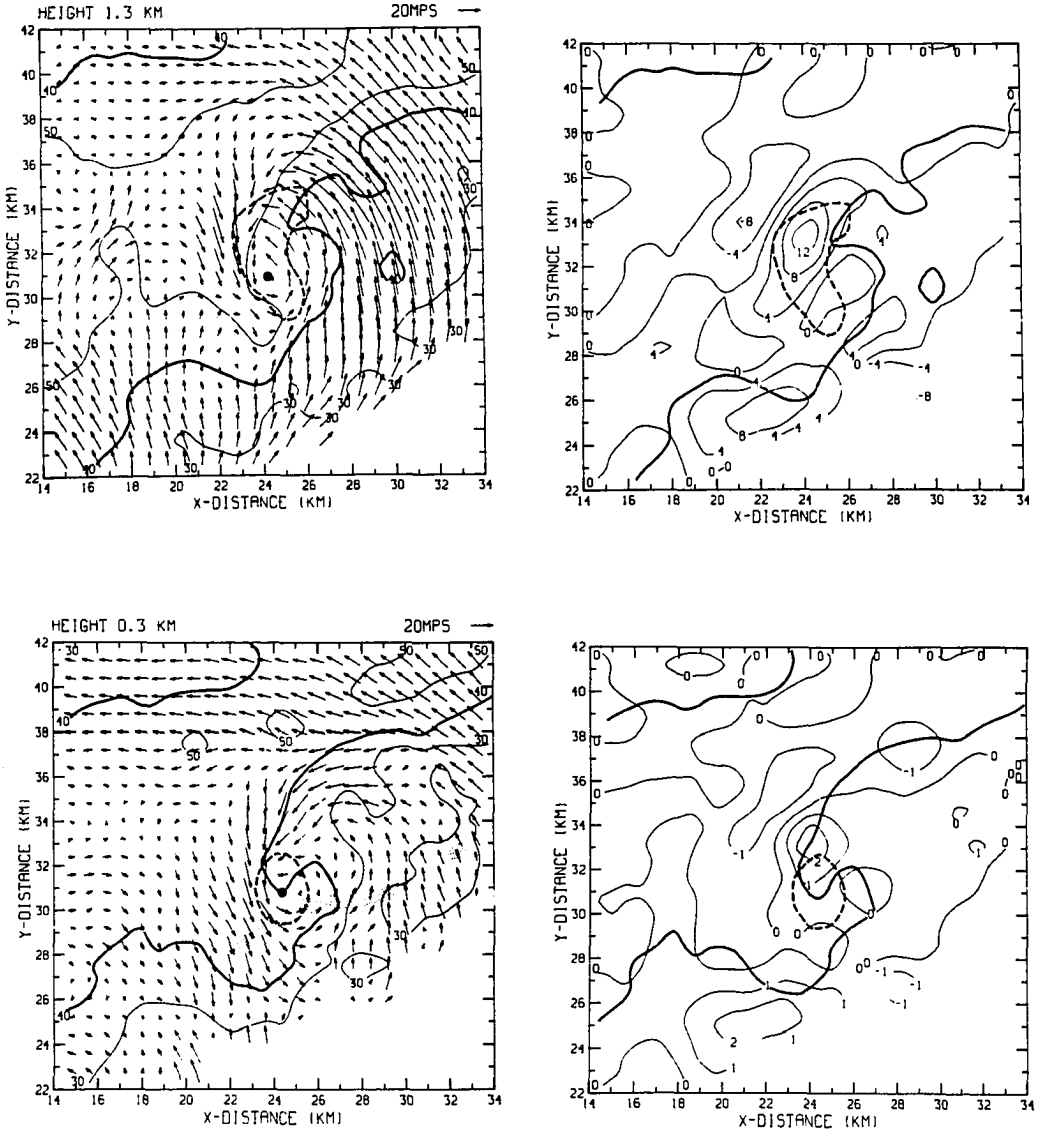

Figure 88. Storm flow, as in Fig. 64, except for tornadic stage in Harrah thunderstorm (1553 CST). Tornado shown by dot. (z=0.3, 1.3, 3.3 km)

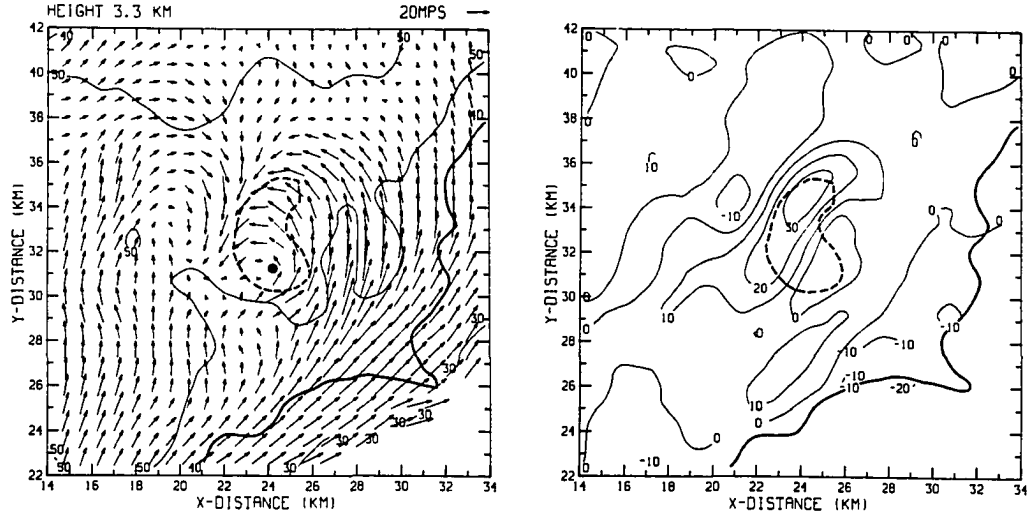

Figure 88. (Continued)

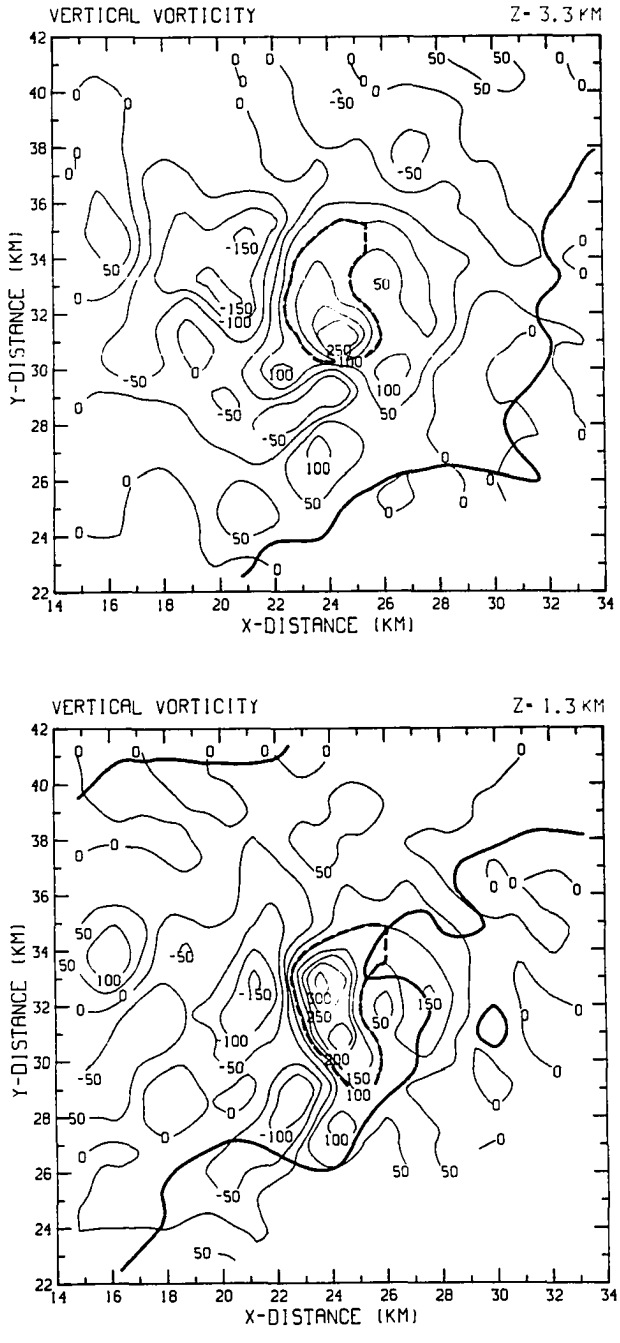

Figure 89. Vertical vorticity, as in Fig. 65, except for tornadic stage in Harrah thunderstorm (1553 CST).

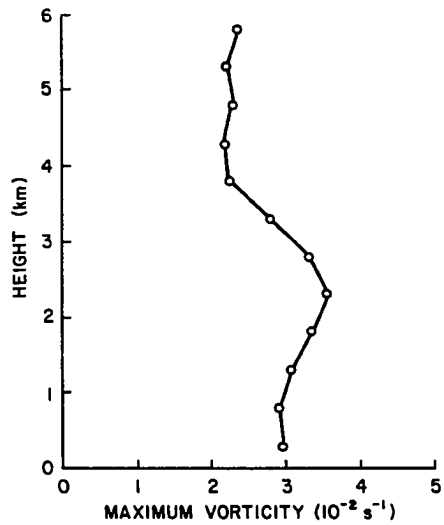

Figure 90. Vertical distribution of maximum vertical vorticity for tornadic stage in Harrah mesocyclone (1553 CST).

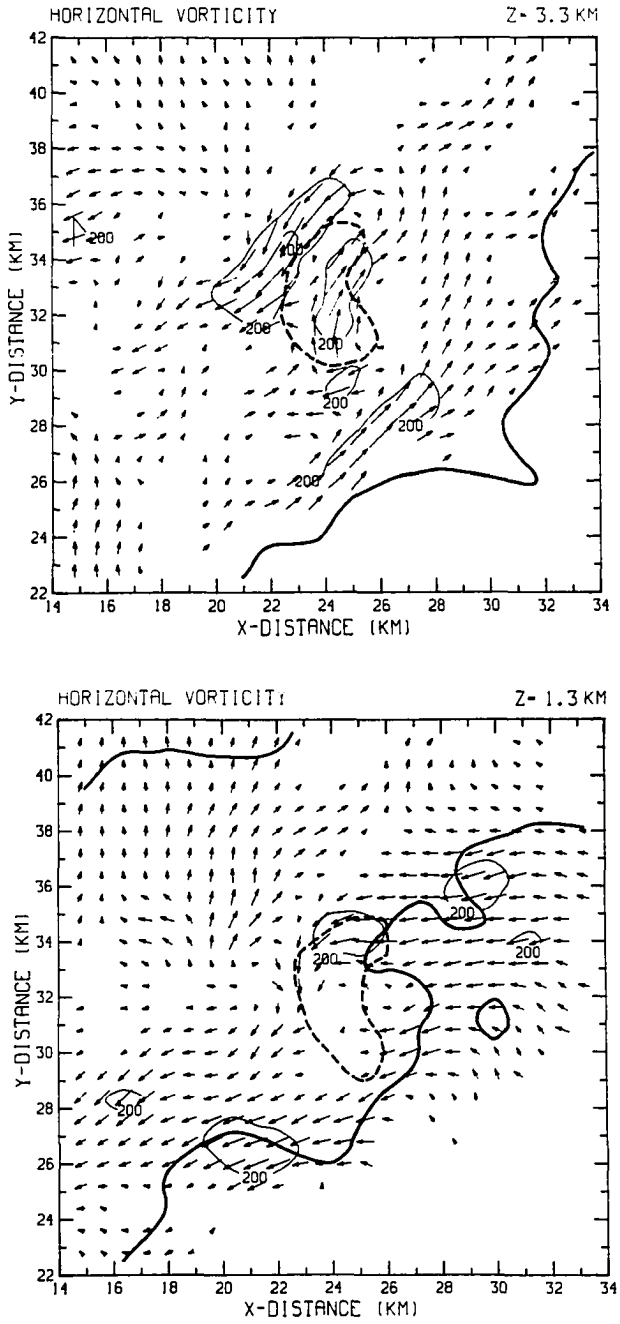

Figure 91. Horizontal vorticity, as in Fig. 67, except for tornadic stage in Harrah thunderstorm (1553 CST). (z=1.3 and 3.3 km)

generation takes place in northern sections of the mesocyclone where strong horizontal vorticity coincides with a strong vertical wind gradient (z=1.3 km, Fig. 92). Peak production, at rates comparable to those in the Del City storm, occurs several kilometers distant from the tornado. A secondary vorticity generation area exists where rainy downdraft air merges with inflow. Air parcels entering the mesocyclone (Fig. 93) have long and complex histories in which horizontal and vertical vorticity is gained and lost. The large horizontal vorticity in northern sections of the mesocyclone is locally generated and involves flow turned about the mesocyclone. Air parcels close by the tornado (e.g., x=25, y=31, z=1.3 km) start from slightly lower levels to the right of the mesocyclone. The horizontal vorticity of these parcels increases as they enter the mesocyclone from the north and then decreases. This vorticity is weakly tilted into cyclonic and anticyclonic vertical vorticity in western and central sections of the mesocyclone. The explosive growth of vertical vorticity experienced is almost entirely by the convergence term (Fig. 94). Whether any parcels actually make the complete journeys shown for two parcels from the storm's rear is doubtful.

Mesocyclone regions filled by downdrafts at z=1.3 km exhibit strong convergence term vorticity dissipation and weak vorticity generation by twisting. At 3.3 km, the twisting mechanism is very strong in vicinity of the tornado but the convergence term has turned dissipative. Flow near the elevated tornado (z=3.3 km, Fig. 93) is a mixture of air parcels from disparate regions on the storm's rear and the right flank.

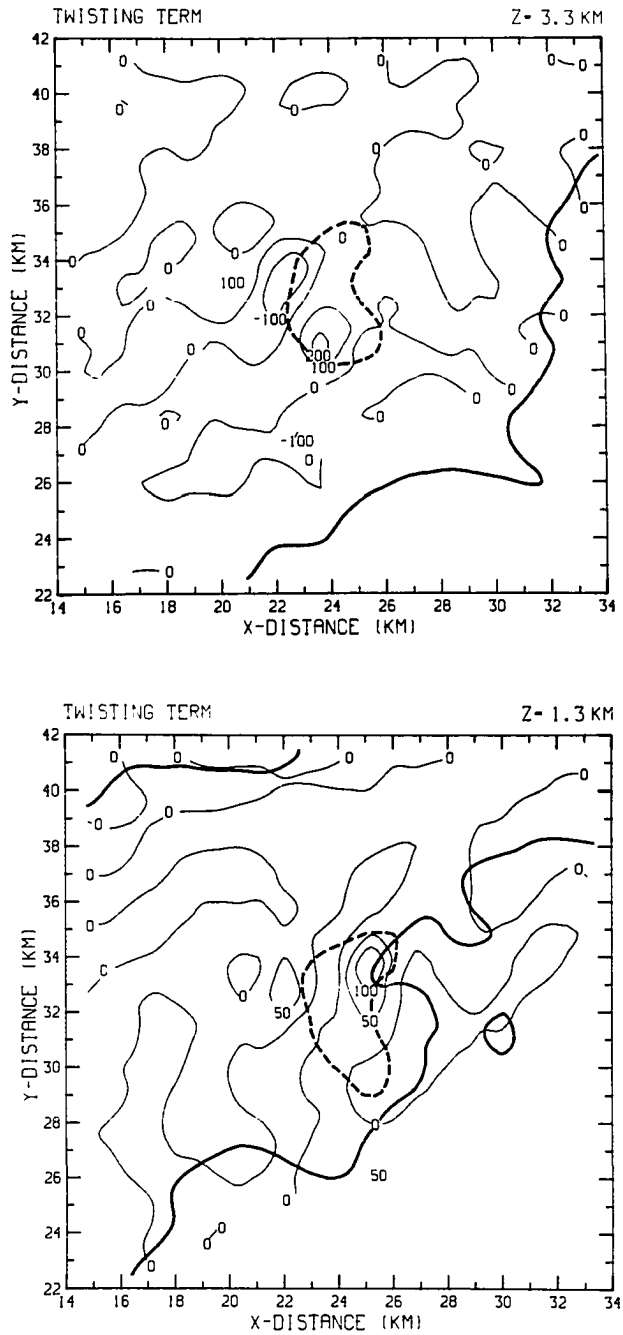

Figure 92. Vertical vorticity generation by twisting term, as in Fig. 69, except for tornadic stage in Harrah thunderstorm (1553 CST).

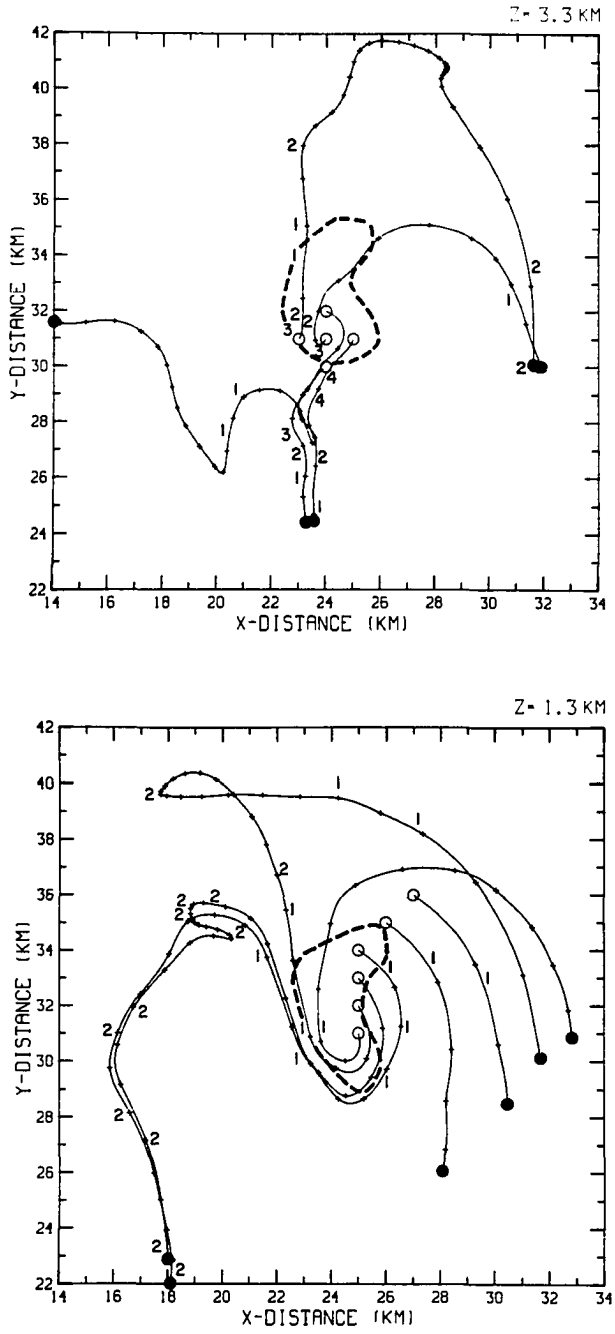

Figure 93. Parcel trajectories, as in Fig. 83, except for tornadic stage in Harrah thunderstorm (1553 CST). Histories shown for select parcels at 1.3 and 3.3 km elevation.

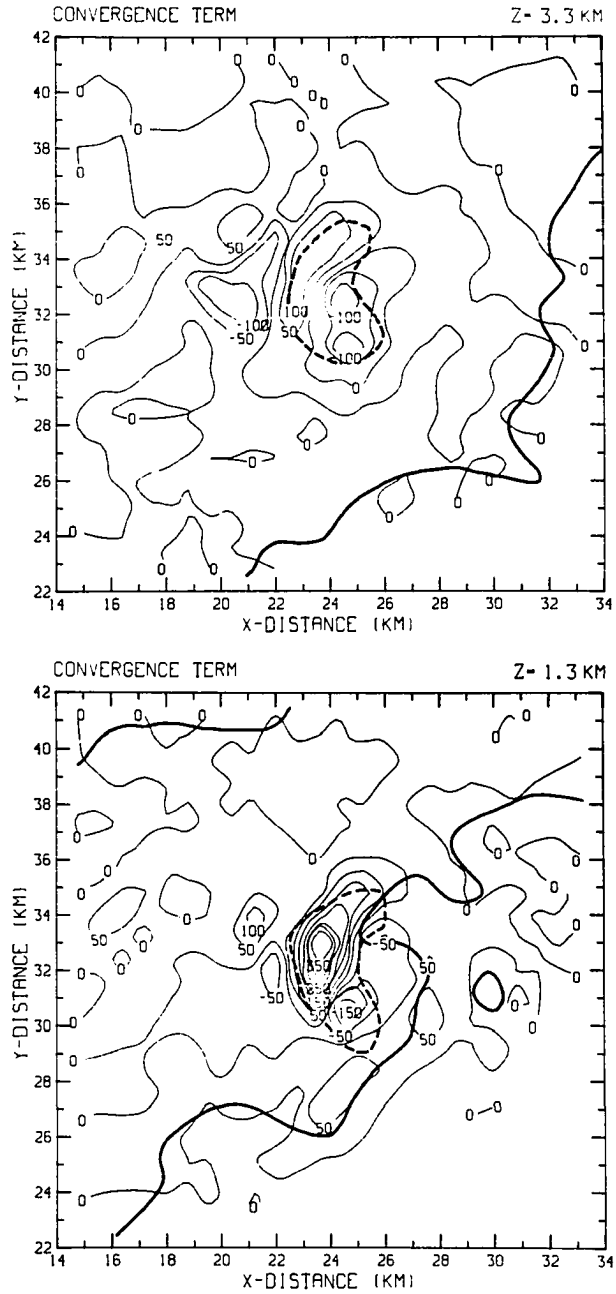

Figure 94. Vertical vorticity amplification by the convergence term, as in Fig. 70, except for tornadic stage in Harrah thunderstorm (1553 CST).

Mesocyclone kinematic properties are summarized in Figs. 95 and 96. The wider spread in computed divergence follows from updraft intensification and rear downdraft formation. Enhanced convergence between rainy downdraft and inflow air greatly augments vorticity amplification by the convergence term. Vorticity generation by twisting above 3 km has roughly tripled with rear downdraft development and more than offsets convergence term dissipation. No clear pattern for mean twisting generation is evident below 3 km.

Error growth in the analyzed wind fields caused middle level retrieved temperature deviations to be entirely too warm (>20°C). Hence, thermodynamic fields are only presented for low levels where the error build-up is small (Fig. 97). Comparison with Fig. 87 reveals a general cooling has taken place in regions surrounding the mesocyclone. Warm temperatures exist in northern mesocyclone sections where flow, having cycled about the mesocyclone and passing through the downdraft, rises in the updraft. Lowest pressures are 3 km east of the mesocyclone. The mesolow has been displaced from the mesocyclone by large wind field strain in the region between the rainy downdraft and the tornado.

5. 1603 CST: Tornado Dissipation

Mesocyclone rotation continued to intensify below 2 km between 1553 and 1603 (Figs. 98 and 99); and a more simple arc of strong vertical vorticity, much like that of earlier stages (c.f., Fig. 74), evolved. Tornado-like wind damage ceased, but several anomalous shear zones (not shown) persisted along the elongated (horizontal) axis of the mesocyclone.

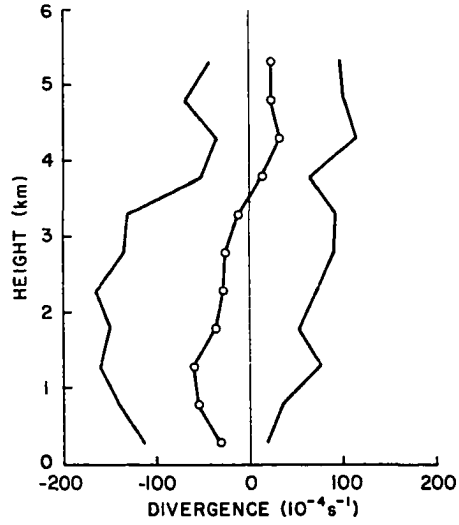

Figure 95. Vertical distribution of mean divergence and range in values, as in Fig. 71, except for tornadic stage (1553 CST).

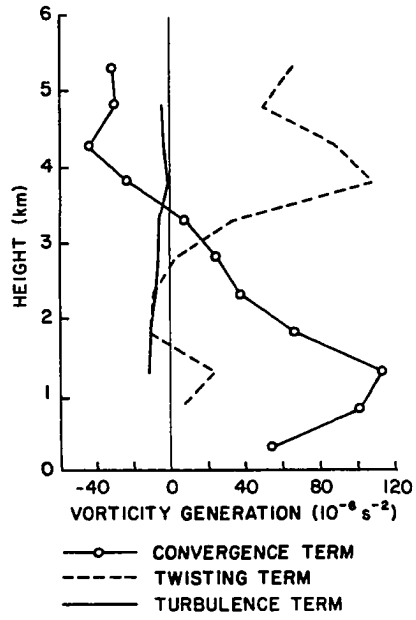

Figure 96. Vertical distribution of mean mesocyclone vertical vorticity production by the convergence, twisting, and turbulence terms, as in Fig. 72, except for tornadic stage in Harrah thunderstorm (1553 CST).

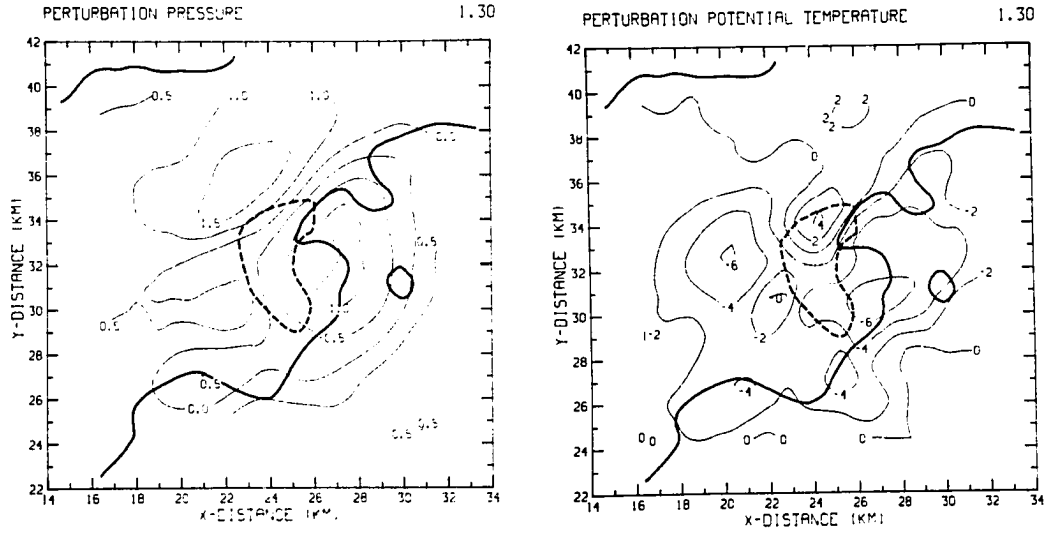

Figure 97. Retrieved perturbation potential temperature and perturbation pressure, as in Fig. 87, except during the tornadic stage in the Harrah thunderstorm (1553 CST). (z=1.3 km)

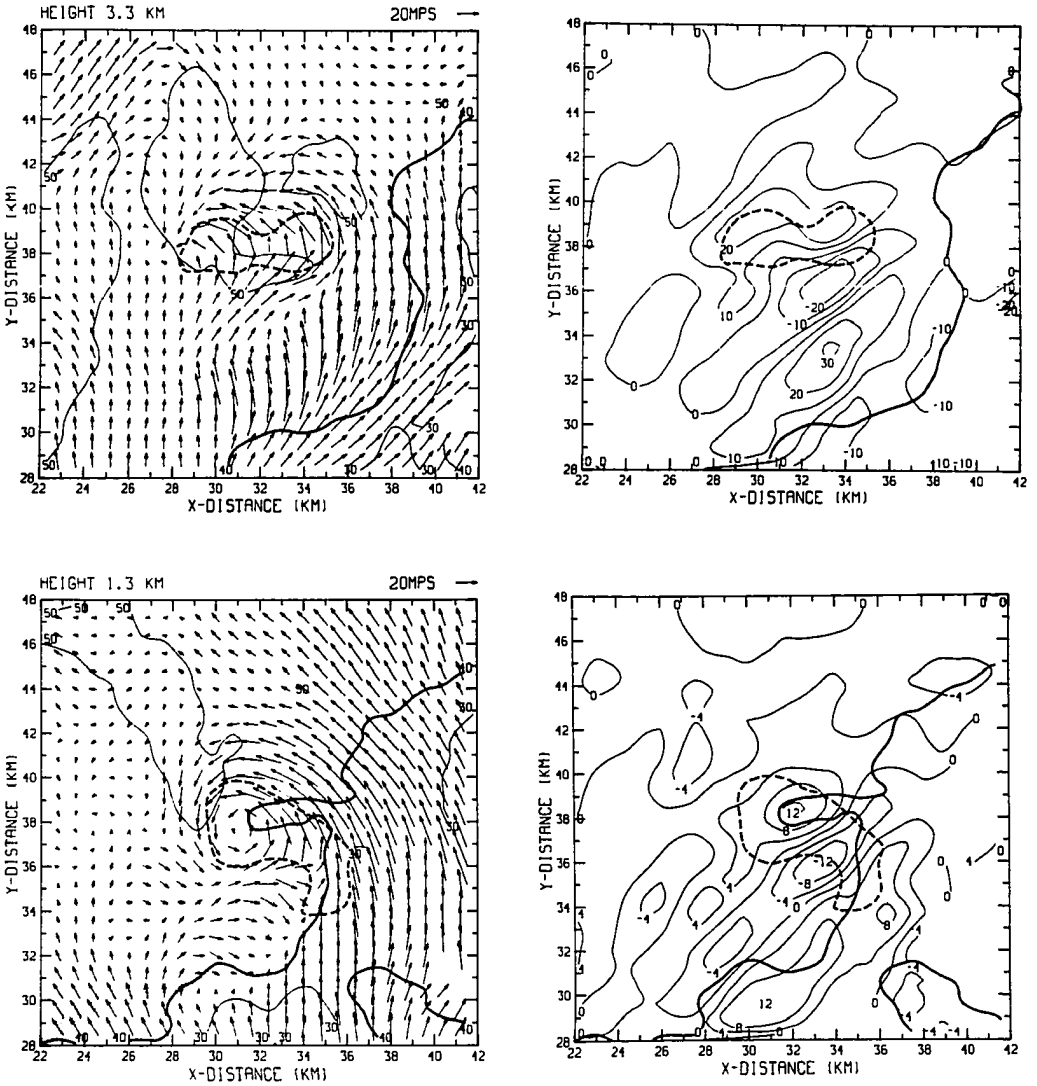

Figure 98. Storm flow, as in Fig. 64, except for post-tornadic stage in Harrah thunderstorm (1603 CST).

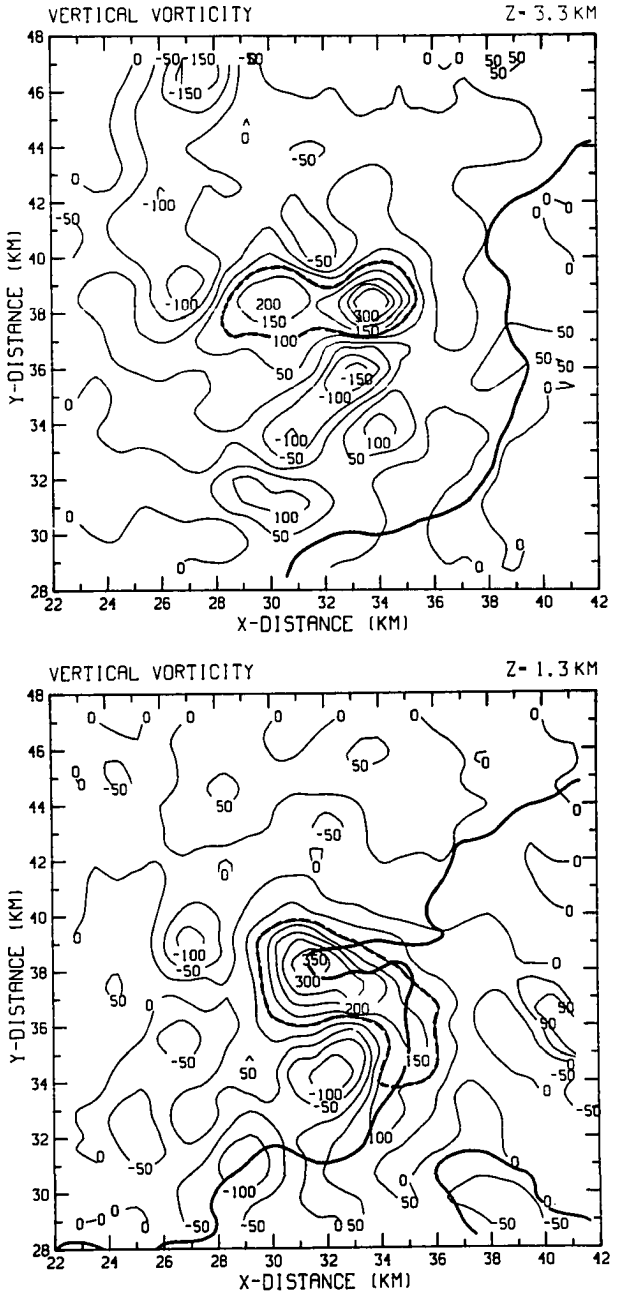

Figure 99. Vertical vorticity, as in Fig. 65, except for post-tornadic stage in Harrah thunderstorm (1603 CST).

Virtually all evidence points to storm decline. The principal updraft has weakened and is noticeably split at 3.3 km (note maxima at x=30, y=39 and x=33, y=39 km). The intensity of the tornado spawning vertical vorticity center decreases from ground to ~2 km (Fig. 100) whereupon a second center appeared within eastern portions of the mesocyclone. (The magnitude of the second center is plotted above 2 km). The rainy downdraft has weakened, but the rear downdraft has grown to become a prominent storm feature.

The large region of strong horizontal vorticity east of the mesocyclone at 1553 has shrunken considerably (Fig. 101). Positive vertical vorticity is generated by twisting 2-3 km east of the mesocyclone center (Fig. 102), but the horizontal vorticity now tilted associates with flow entrained from the storm's rear (Fig. 103). Flow at the mesocyclone core, composed of parcels from the rear downdraft and from the right flank, has strong horizontal vorticity. However, the vorticity vector is opposite the vertical velocity gradient and vertical vorticity is dissipated.

Convergence term amplification of vertical vorticity at low levels concentrates near the vorticity maxima (Fig. 104). Production rates exceed 500×10^{-6} s^{-2} at 0.3 km but decline rapidly with height. It is difficult with the present data to ascertain why the tornado dissipated during a period in which the low level mesocyclone was intensifying and being subjected to large vorticity amplification by the convergence mechanism. Trajectory analyses (e.g., Fig. 103) show air parcels are exposed to these extreme rates only for short periods. Apparently vorticity production is insufficient to intensify the existing shear anomalies beyond the embryonic stage.

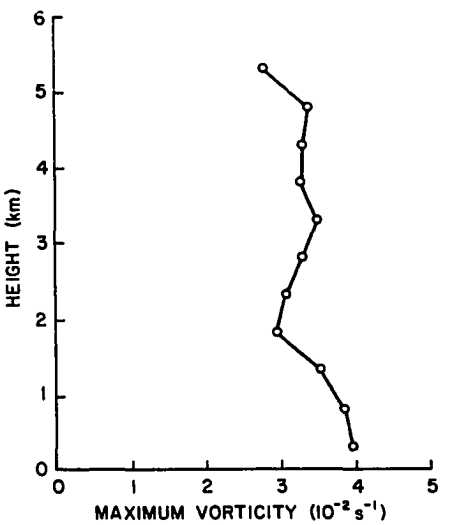

Figure 100. Vertical distribution of maximum vertical vorticity for post-tornadic stage in Harrah mesocyclone (1603 CST).

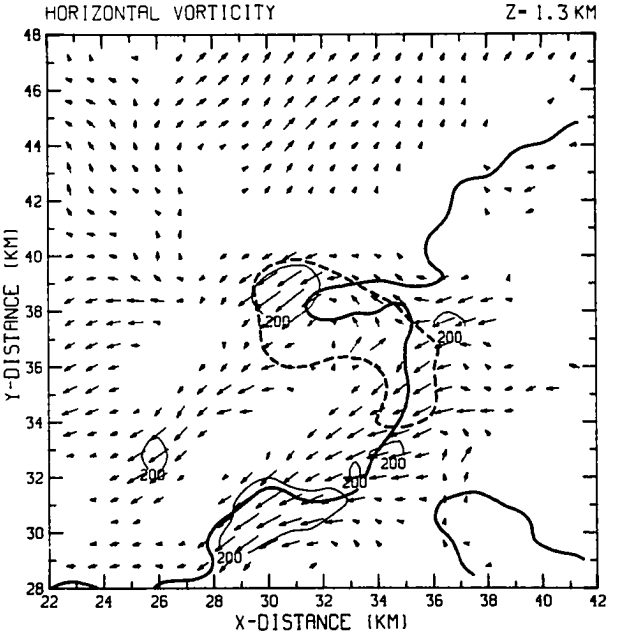

Figure 101. Horizontal vorticity, as in Fig. 67, except for post-tornadic stage in Harrah thunderstorm (1603 CST). (z=1.3 km)

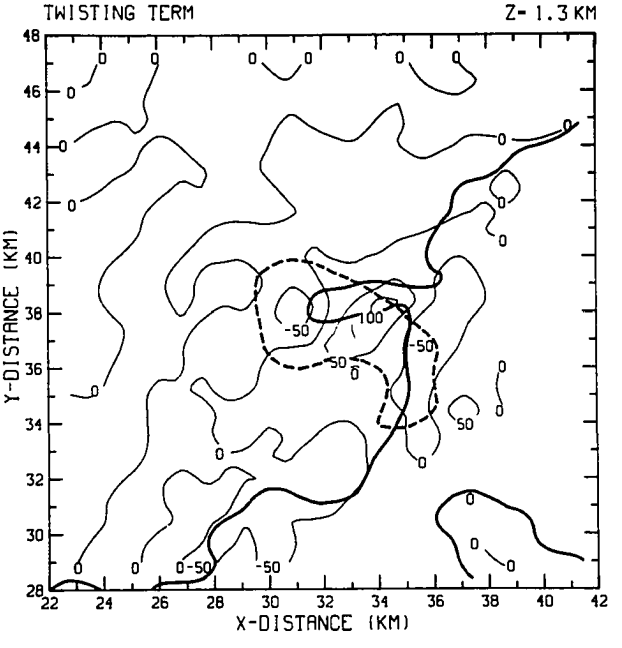

Figure 102. Vertical vorticity generation by twisting term, as in Fig. 69, except for post-tornadic stage in Harrah thunderstorm (1603 CST). (z=1.3 km)

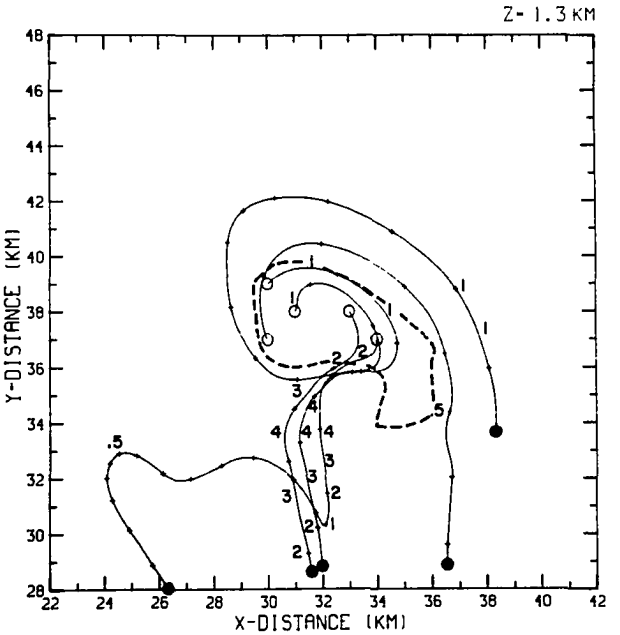

Figure 103. Parcel trajectories, as in Fig. 83, except for post-tornadic stage in Harrah thunderstorm (1603 CST). Histories shown for select parcels at 1.3 km elevation.

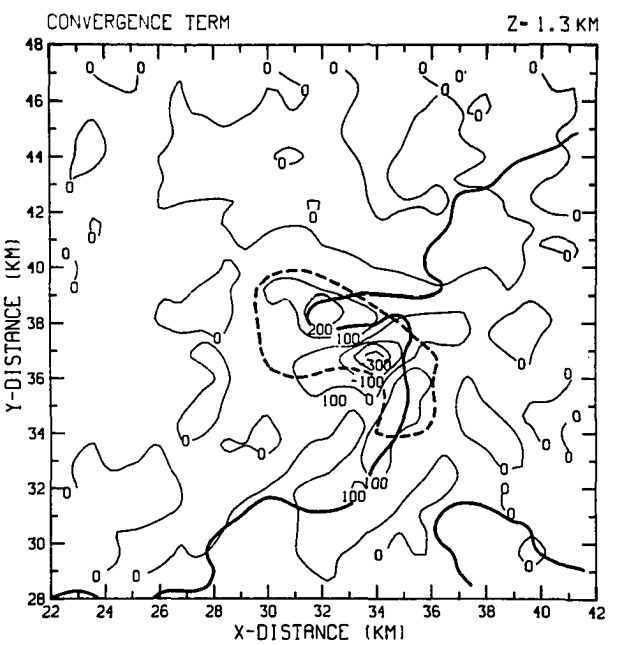

Figure 104. Vertical vorticity amplification by the convergence term, as in Fig. 70, except for post-tornadic stage in Harrah thunderstorm (1603 CST). (z=1.3 km)

Mesocyclone divergence and mean vorticity production are given in Figs. 105 and 106. Data above 2 km are more representative of the second vorticity center. No doubt the build-up of wind field error contributes to the extreme spread in divergence values. Increased twisting term generation of vorticity is a consequence of rear downdraft intensification.

Retrieved thermodynamic variables are shown only for 1.3 km (Fig. 107). Cool temperatures east of the mesocyclone persist from 1553 but are suspicious nonetheless because of missing observations near ground. Greater confidence is placed in cool temperatures behind the gust front and in relatively warm temperatures within central portions of the mesocyclone. The latter could represent the adiabatic warming of air that descended in the rear downdraft. Low level vorticity now far exceeds the magnitude of the strain terms and lowest pressures nearly coincide with the mesocyclone. Pressure gradients south of the mesolow promote the influx of rear downdraft air into the mesocyclone.

6. 1611 CST: Mesocyclone Decline

When last sampled, mesocyclone rotation had weakened and low level flow was becoming increasingly divergent (Fig. 108). Principal updraft (~4 km north of the mesocyclone) and the rear downdraft had declined. At ground, weak updraft persisted only in western portions of the mesocyclone. As in the dissipative stage of the Oklahoma City storm, the mesocyclone at all levels is filled by air parcels that originated on the storm's rear (Fig. 109). Inflow from the right flank now ascends in updraft to the north of the mesocyclone and is no longer caught by the rotational flow.

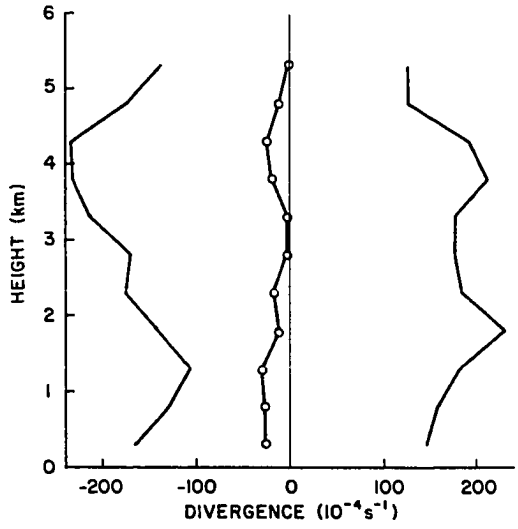

Figure 105. Vertical distribution of mean divergence and range in values, as in Fig. 71, except for post-tornadic stage in Harrah thunderstorm (1603 CST).

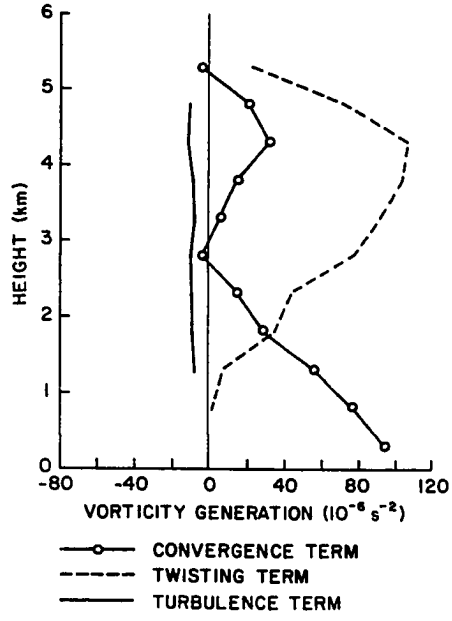

Figure 106. Vertical distribution of mean mesocyclone vertical vorticity production by the convergence, twisting, and turbulence terms, as in Fig. 72, except for post-tornadic stage in Harrah thunderstorm (1603 CST).

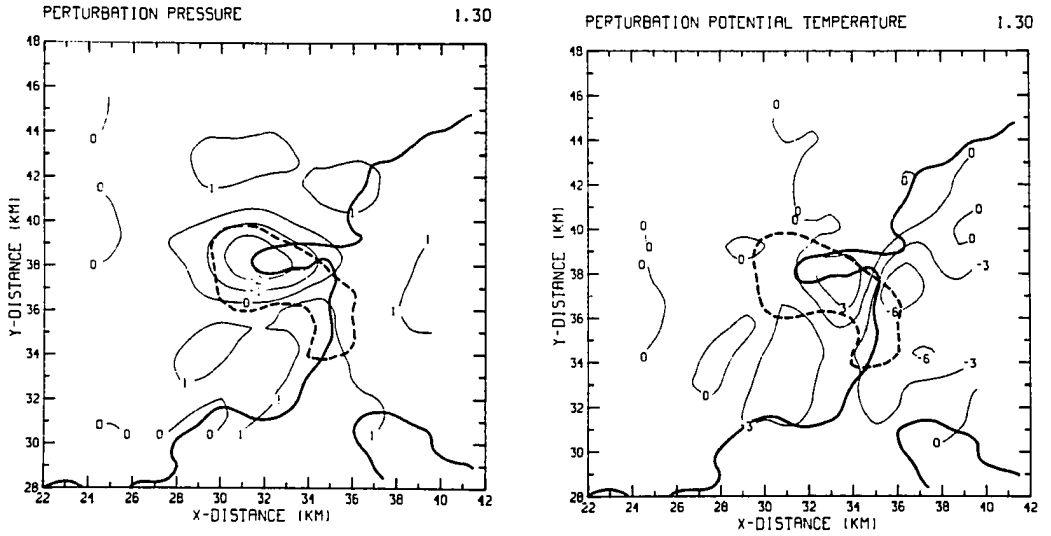

Figure 107. Retrieved perturbation potential temperature and perturbation pressure, as in Fig. 87, except during the post-tornadic stage in Harrah thunderstorm (1603 CST). (z=1.3 km)

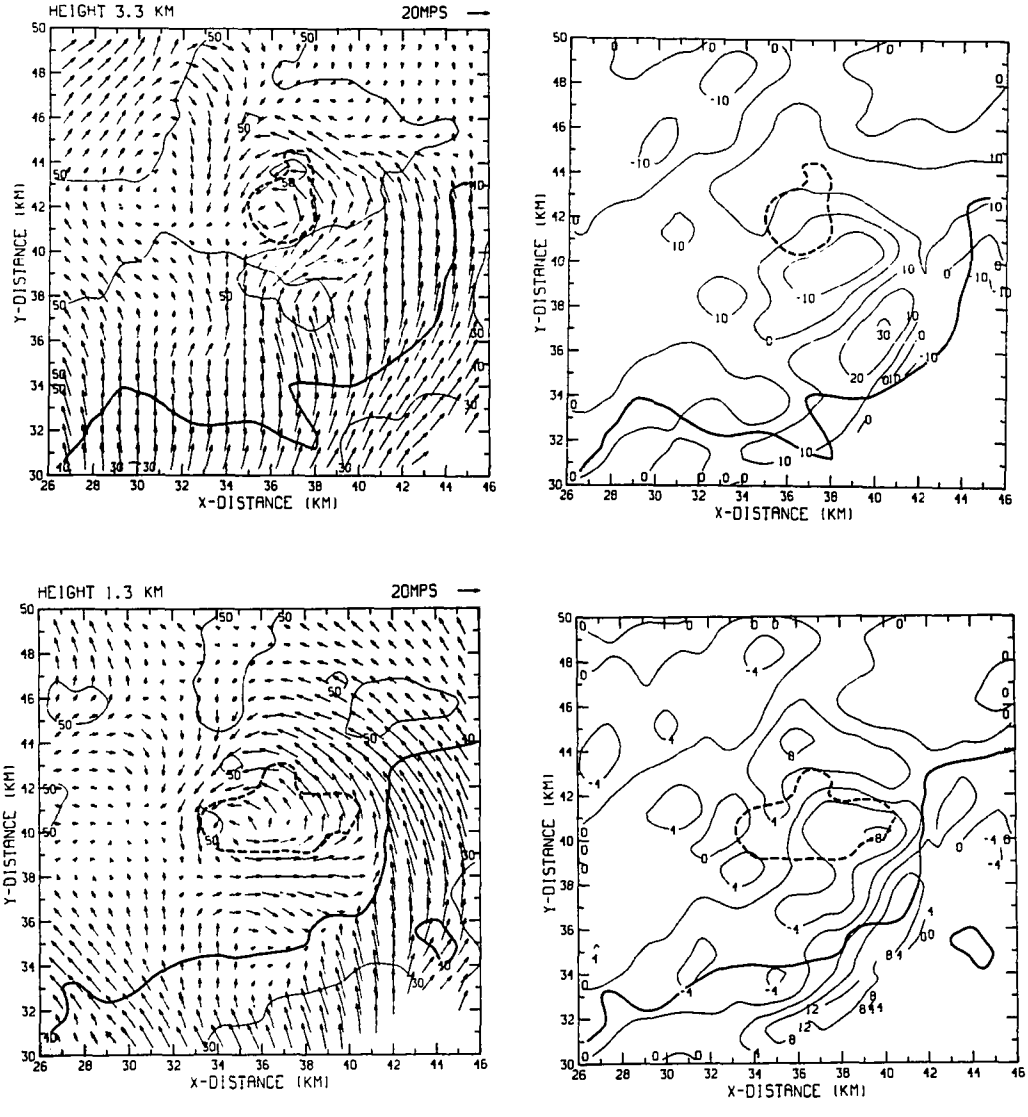

Figure 108. Storm flow, as in Fig. 64, except for dissipation stage in Harrah thunderstorm (1611 CST).

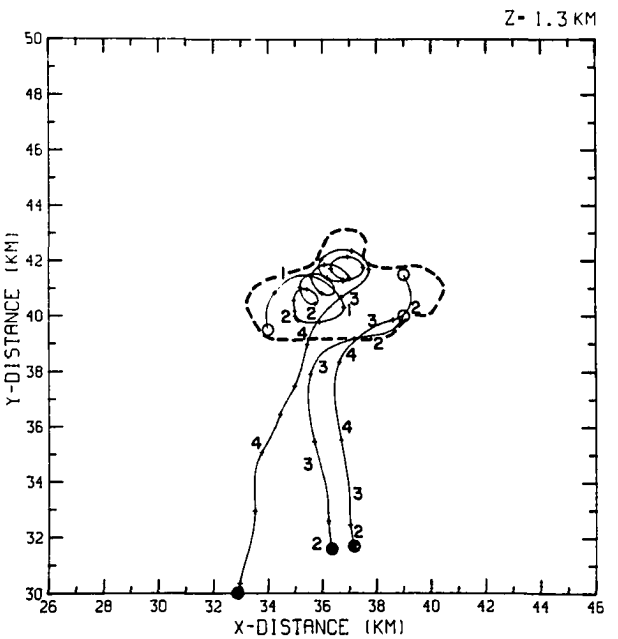

Figure 109. Parcel trajectories, as in Fig. 83, except for dissipation stage (1611 CST). Histories shown for select parcels at 1.3 km elevation.

Decline of the tornado producing vorticity maxima in western portions of the mesocyclone is portrayed in Fig. 110. Vorticity has fallen to 325×10^{-4} s^{-1} near ground and decreases rapidly to 175×10^{-4} s^{-1} at 1.8 km, whereupon the center could no longer be identified. Twisting term vorticity generation (Fig. 111), like vertical motion, has declined. Spreading downdrafts cause the convergence term to be negative and vertical vorticity to be dissipated in all but extreme northwestern portions of the mesocyclone (Fig. 112). The dissipation overwhelms generation by twisting.

Mesocyclone-updraft separation and rear downdraft decline have reduced the range of computed divergence within the mesocyclone (Fig. 113). Downdraft infiltration causes the mean flow throughout the vertical depth in which the vorticity maximum could be identified to be divergent. The combined mean vorticity production by convergence, twisting and turbulence is predominantly dissipative in the lowest 2 km (Fig. 114); and further mesocyclone decline is anticipated.

The significant feature in the retrieved thermodynamic fields is the high pressure center in the region of shearing deformation (strain) where the environmental wind on the storm's rear interacts with mesocyclone flow (x=33, y=38, z=1.3 km; Fig. 115). Rate of strain forcing decreases more slowly with height than vortical forcing; consequently, the mesohigh slopes over declining portions of the mesocyclone. Strong downward perturbation pressure gradients, much like in tornadic and dissipative stages of the two other storms, are created both in the rear downdraft and in the dissipating vorticity center (also Fig. 116). The pressure gradient forces buoyant air in upper regions of the rear downdraft downward.

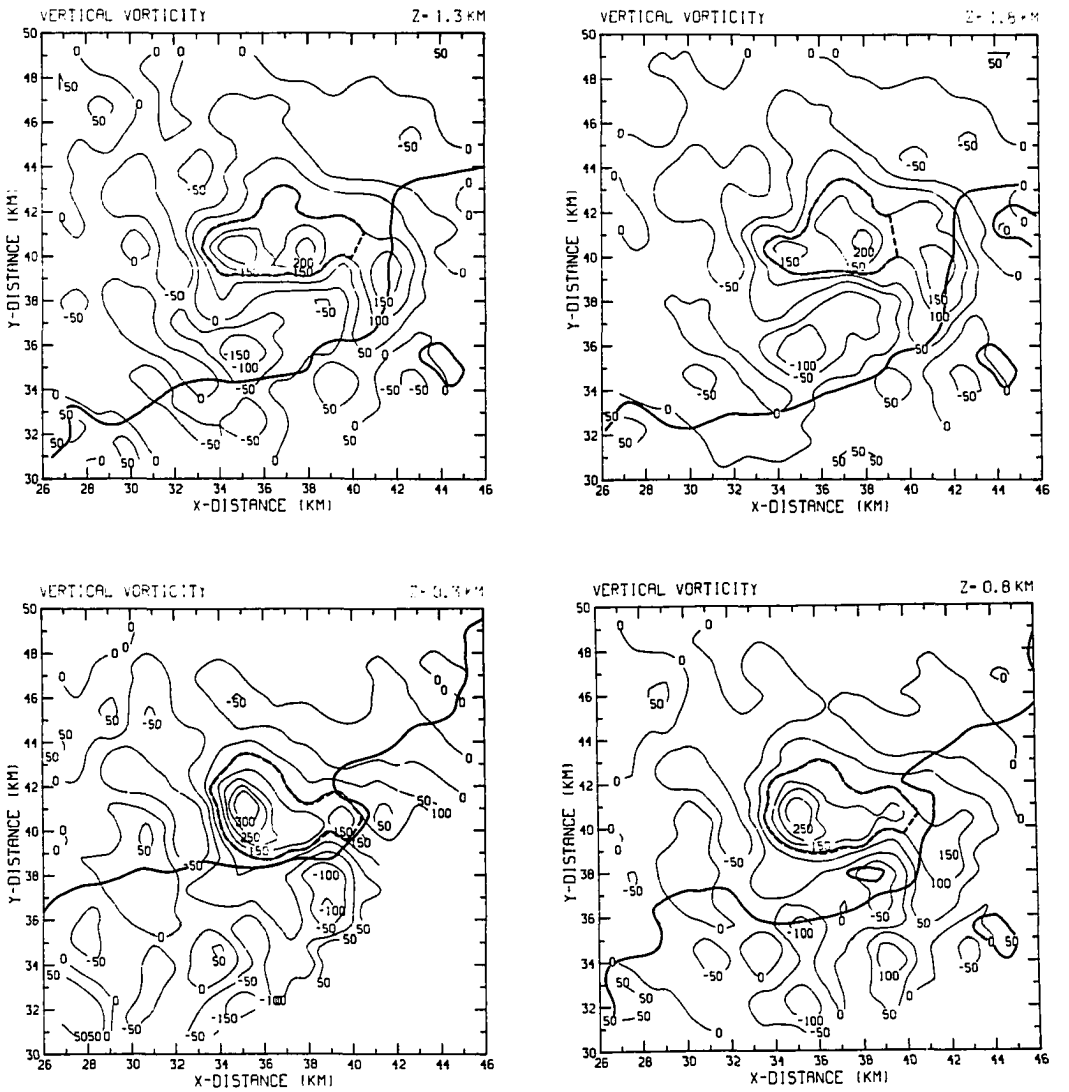

Figure 110. Vertical vorticity, as in Fig. 65, except for dissipation stage in Harrah thunderstorm (1611 CST). (z=0.3 0.8, 1.3, 1.8 km)

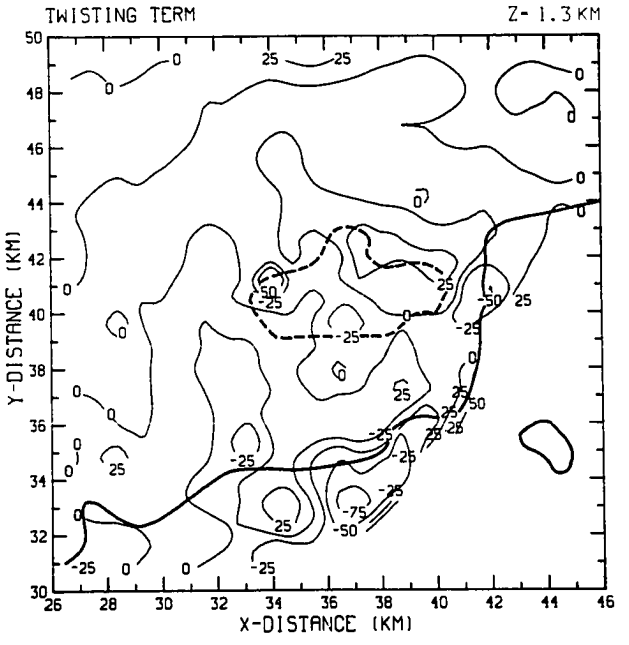

Figure 111. Vertical vorticity generation by twisting term, as in Fig. 69, except for dissipation stage in Harrah thunderstorm (1611 CST). (z=1.3 km)

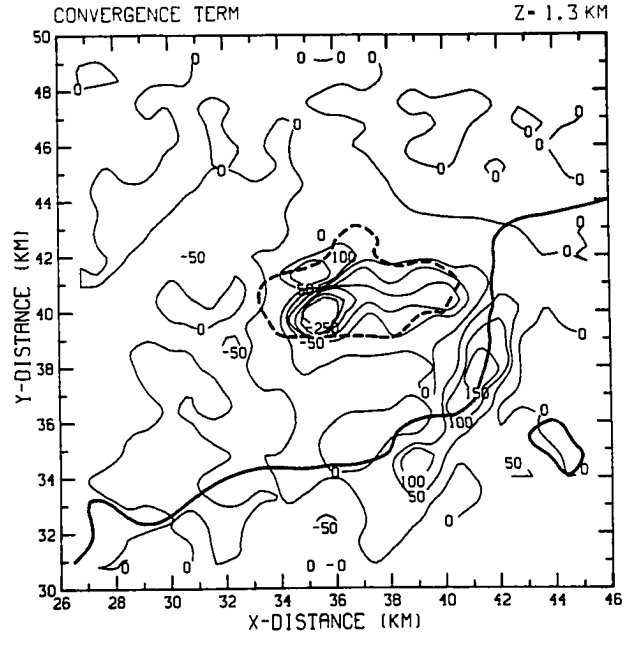

Figure 112. Vertical vorticity amplification by the convergence term, as in Fig. 70, except for dissipation stage in Harrah thunderstorm (1611 CST). (z=1.3 km)

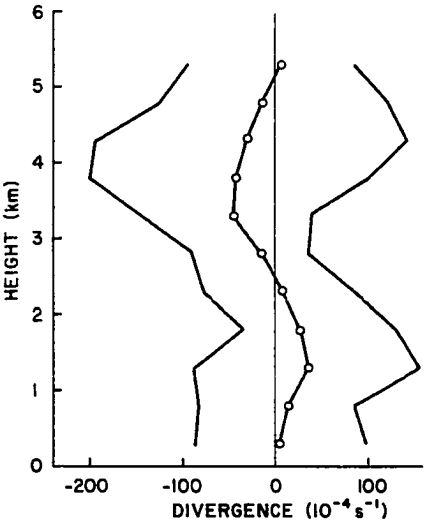

Figure 113. Vertical distribution of mean divergence and range in values, as in Fig. 71, except for dissipation stage in Harrah thunderstorm (1611 CST).

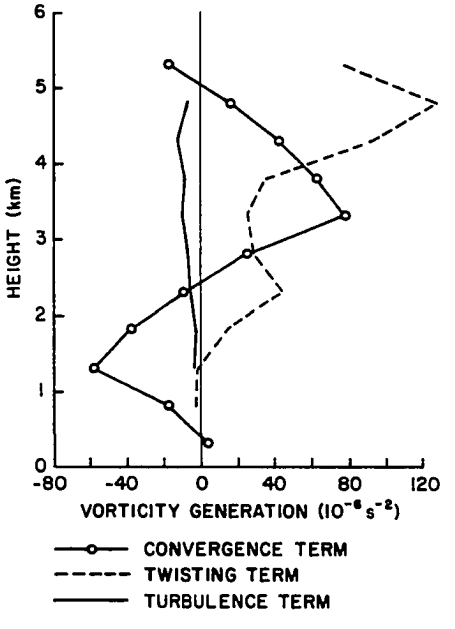

Figure 114. Vertical distribution of mean mesocyclone vertical vorticity production by the convergence, twisting, and turbulence terms, as in Fig. 72, except for dissipation stage in Harrah thunderstorm (1611 CST).

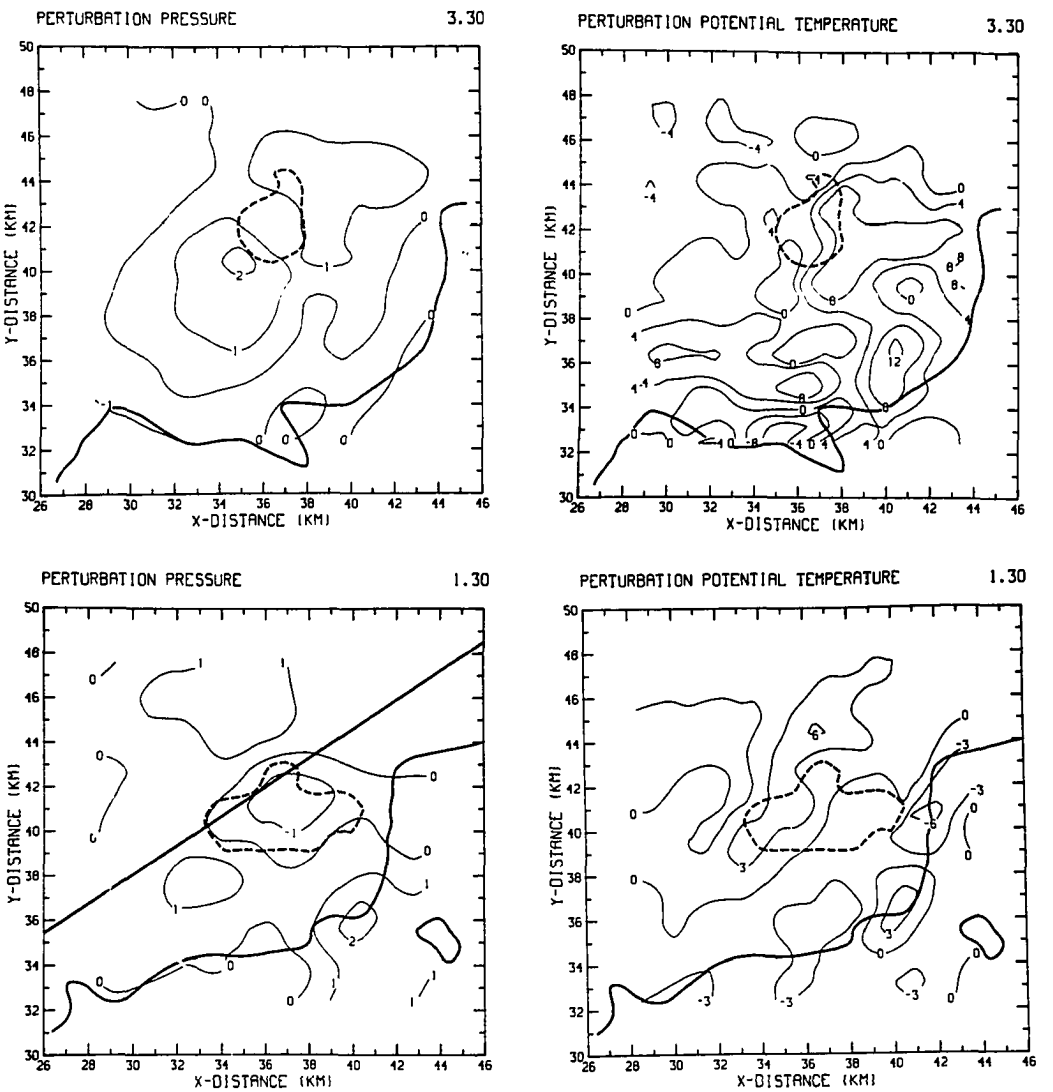

Figure 115. Retrieved perturbation potential temperature and perturbation pressure, as in Fig. 87, except for dissipation stage in Harrah thunderstorm (1611 CST).

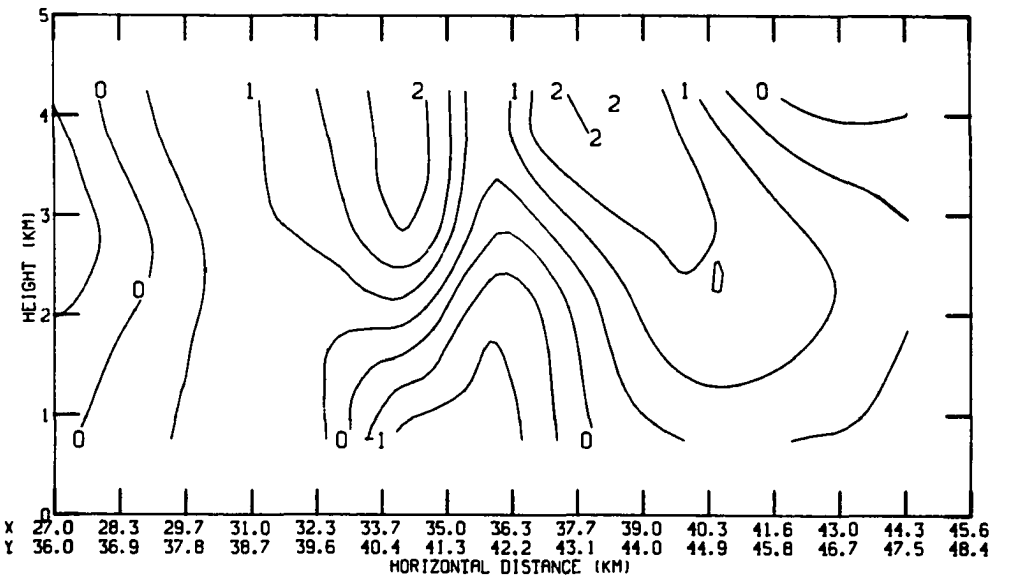

Figure 116. Vertical cross-section of perturbation pressure in mb for dissipation stage in Harrah thunderstorm (1611 CST). See Fig. 115 (z=1.3 km) for location.

7. Harrah Storm Summary

Vertical vorticity production in the Harrah storm began upwind of the mesocyclone as strong horizontal vorticity was tilted into vertical vorticity. The tilted vorticity and pre-existing vertical vorticity were subsequently amplified to mesocyclone intensity by the convergence mechanism. In early stages, vertical vorticity increased with height and updrafts filled the mesocyclone. Minimum perturbation pressure, like maximum vorticity, was aloft. As in the Del City storm, vertical pressure gradients caused negatively buoyant air at the base of updraft to be transported upward.

During tornadogenesis, rapid vertical vorticity intensification and accelerated convergence term amplification of vorticity occurred below 4 km. Vorticity growth was attributed to strong interaction between outflow from a rainy downdraft and inflow air from the storm's right flank. Air parcels swept about the tornado passed through the region of strong convergence term production. Vertical vorticity generation by twisting, about a factor of 3 less than that by convergence, involved locally enhanced horizontal vorticity associated with the intensification of three-dimensional vorticity in vicinity of the tornado. At this stage the mesolow separated from the mesocyclone as strong shearing deformation (rate of strain) developed between the rainy downdraft and the principal updraft. Also, at this stage a rear downdraft began to form. The rear downdraft became most intense when peak vertical vorticity was at ground (1603), i.e., when the vertical gradient of vorticity in vicinity of the tornado remnants reversed.

In final stages, the close relationship between strong vorticity and low pressure was restored. Vorticity weakened and decreased rapidly with height. As a result, downward pressure gradients existed in the mesocyclone and in adjacent regions. Flow from the ensuing downdraft filled the mesocyclone.

V. COMPARISON WITH NUMERICAL SIMULATIONS OF SEVERE THUNDERSTORMS

Klemp and Rotunno (1982) have studied the tornadic region of severe thunderstorms by nesting fine resolution grids within the Klemp and Wilhelmson thunderstorm model. Results for a simulation of the Del City storm are presented in Fig. 117. Windflow, vertical vorticity, convergence term vorticity production and twisting term vorticity production are all remarkable reproductions of corresponding fields in the observed storm (c.f., Figs. 18, 19, 21, and 23). Note that the twisting term is a maximum at the vorticity center in left hand portions of the vorticity arc, that the updraft and region of maximum convergence term vorticity amplification are displaced upwind from the vorticity center and that the convergence term is about four times greater in magnitude than the twisting term.

Vertical vorticity generation in simulated thunderstorms begins at middle storm levels as horizontal vorticity associated with the vertical shear of the environmental wind is tilted toward the vertical by updraft (Klemp and Rotunno, 1983). Formation of rainy downdrafts then causes strong convergence to develop along gust fronts between subsiding rain-cooled air and inflow air. Low level vorticity grows rapidly as vorticity tilted into the vertical is amplified by the convergence mechanism. Klemp and Rotunno hypothesize that the maximum vertical vorticity produced is sensitive to added horizontal vorticity

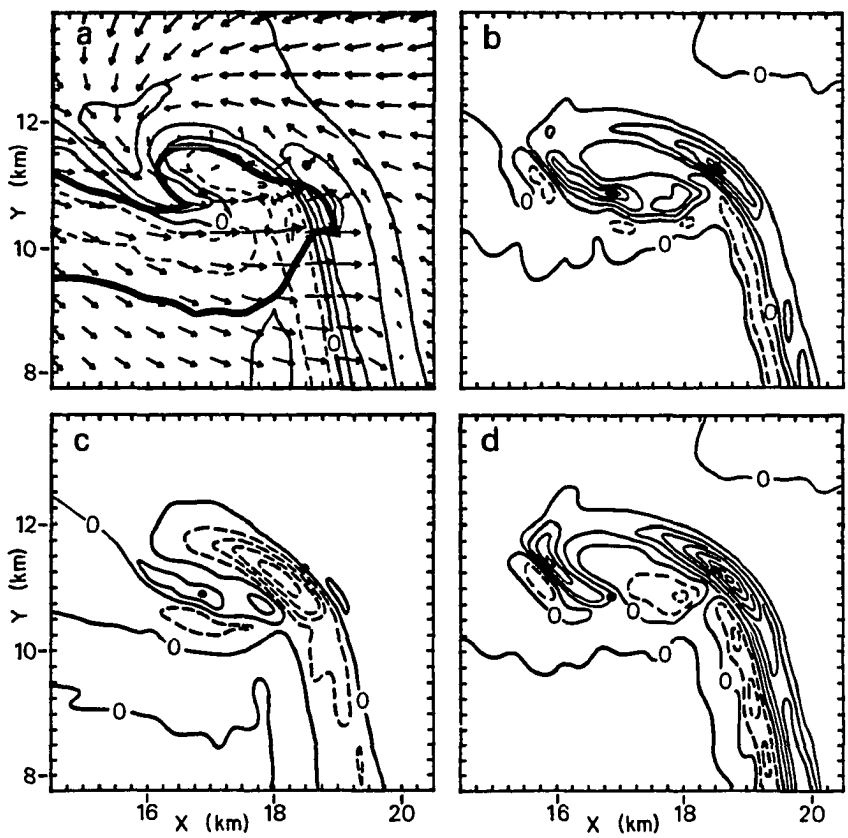

Figure 117. High resolution simulation of the Del City thunderstorm showing (a) horizontal flow field (one grid interval equals 20 m s^{-1}), vertical velocity (1 m s^{-1} contour intervals) and .5 g kg^{-1} rainwater contour; (b) vertical vorticity (0.5×10^{-2} s^{-1} contour intervals); and vertical vorticity production by (c) the twisting term (10^{-5} s^{-2} contour intervals) and (d) the convergence term (2×10^{-5} s^{-2} contour intervals). (z=0.25 km) From Klemp and Rotunno, 1982.

generated in inflow areas by developing temperature gradients, i.e., through the thermal forcing $g\vec{\nabla}x\vec{k}\frac{\theta'}{\theta_o}$ in (4). They present data for a coarse grid simulation corresponding to the pretornadic stage in the Del City storm. Air parcels approaching the vertical vorticity center originate on the right forward flank and are subjected to a temperature gradient created by rain cooled air spreading from beneath the storm core on the right (looking downwind). A vector component of horizontal vorticity in the direction of motion is produced which adds to the horizontal vorticity associated with vertical wind shear. When the enhanced horizontal vorticity is tilted and stretched by updraft, vertical vorticity intensifies.

Vertical vorticity production in observed storms also begins with the tipping of horizontal vorticity associated with the environmental wind. The vorticity produced is subsequently amplified by convergence as the flow passes through the updraft. Tornadogenesis occurs during a period in which updraft and rainy downdraft are both increasing and vorticity amplification by the convergence mechanism is rapidly accelerated by enhanced convergence at gust fronts.

A qualitative evaluation of horizontal vorticity generation by thermal gradients in the observed Del City storm can be made by superposing air parcel trajectories on the retrieved temperature fields. During pretornadic stages, flow entering the low level mesocyclone (z=1.3 km) begins from the right of the mesocyclone--much like trajectories portrayed in Fig. 12. Along the route traversed by this flow, relatively warm air tends to lie to the left and relatively cool air tends to lie to the right (Fig. 16). This configuration is nearly identical to that

presented by Klemp and Rotunno (1983); and in the absence of other effects, rotation (horizontal vorticity) develops in which the vorticity vector points downwind. As low level vorticity intensifies by the convergence mechanism (1845), the source of the inflow air shifts slightly toward the storm's rear (Fig. 22, z=1.3 km); and inflow passes to the right of warm air near and behind the gust front (Fig. 29). The temperature gradient experienced is the same as at 1826 and the vector of the horizontal vorticity produced remains in the direction of the flow.

An entirely different situation exists in the Harrah storm (e.g., Figs. 83 and 87). Cold air resides behind the gust front and within the mesocyclone. Temperature gradients seen by air parcels spiraling toward the mesocyclone from the storm's right rear are reversed from that in the Del City storm, and the vector of horizontal vorticity produced is opposite the direction of motion. Anticyclonic vertical vorticity would be created as this vorticity encounters updraft. These observations suggest the importance of horizontal vorticity generated by temperature gradients varies among storms and could change during a storm's lifetime. Hence, horizontal vorticity produced by thermal buoyancy is not likely to be a major factor in mesocyclone intensification or in tornadogenesis.

VI. SUMMARY AND CONCLUSIONS

Vortical and thermodynamic properties of the parental circulations (mesocyclones) which spawn tornadoes have been documented with Doppler radar observations. The data show that vertical vorticity generation begins during early storm development as low level wind shear (horizontal vorticity) possessed by environmental air is tipped toward the vertical at the leading edge of updraft (Fig. 118). Mesocyclones form as the flow progresses into the principal updraft and the tilted vertical vorticity plus pre-existing background vorticity is further amplified by the convergence term. In the earliest stages, convergence and twisting term vorticity production at low levels were comparable in magnitude; but it is the convergence term that largely determines the location of the mesocyclone and that develops most rapidly in time.

In pretornadic stages maximum vertical vorticity and maximum mesocyclone areal coverage are found aloft. Middle level mesocyclones were positioned upwind from major updraft and were sustained primarily by the tilting of horizontal vorticity.

Tornadogenesis, as noted in previous studies, is accompanied by a multiplicative growth of mesocyclone vorticity at low levels (Fig. 119). Gust fronts between outflow and inflow air intensify and are accelerated forward; attendant positive vorticity and updraft zones become markedly perturbed and arc-shaped. Tornadoes typically reside between the storm updraft and a downdraft that develops on the storm's rear.

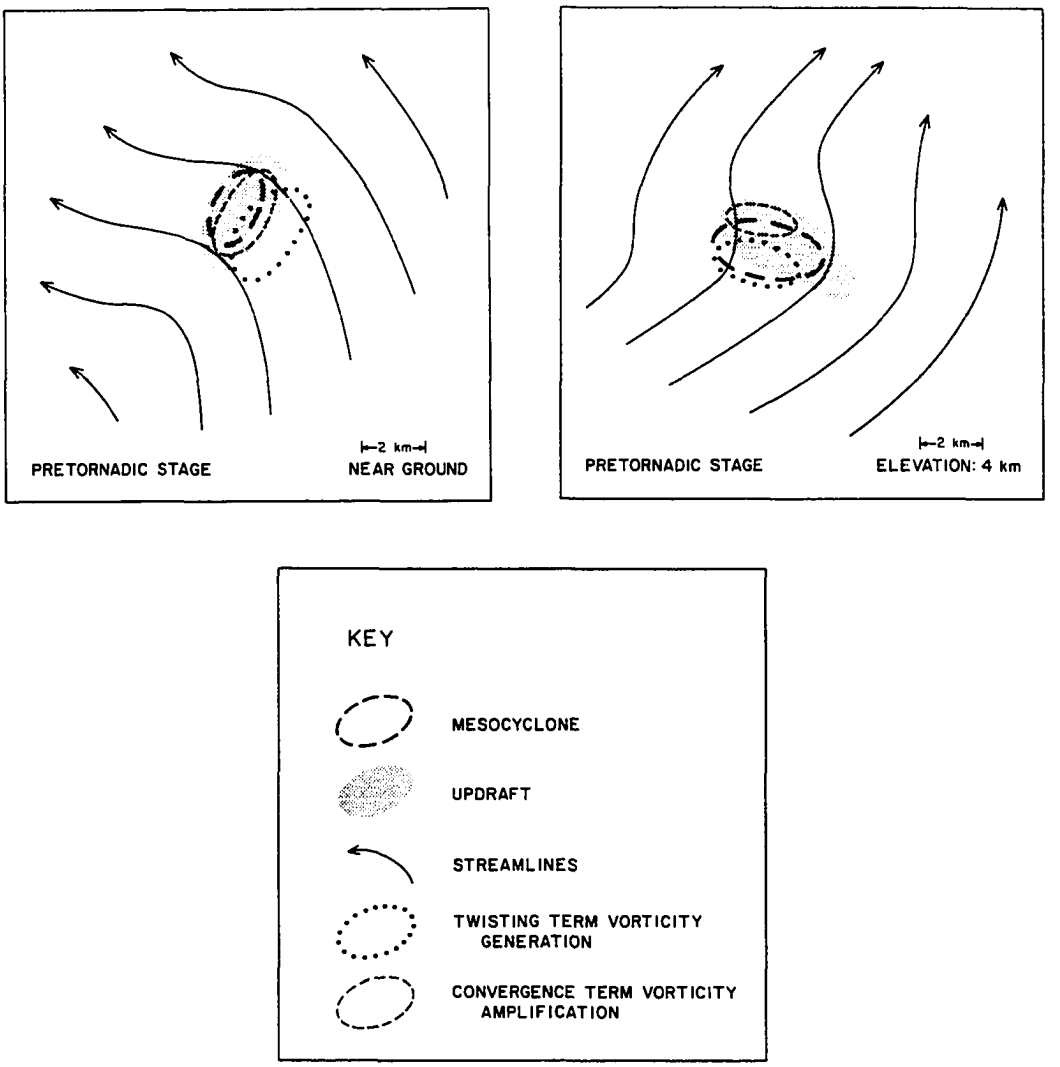

Figure 118. Schematic presentation of key thunderstorm features in vicinity of the low and mid level mesocyclone prior to tornadogenesis. Horizontal flow shown by streamlines and updraft stippled. The mesocyclone indicated by a heavy dashed line. Regions of vertical vorticity production by twisting and convergence mechanisms shown respectively by dotted and thin dashed lines. Storm motion is toward the upper right.

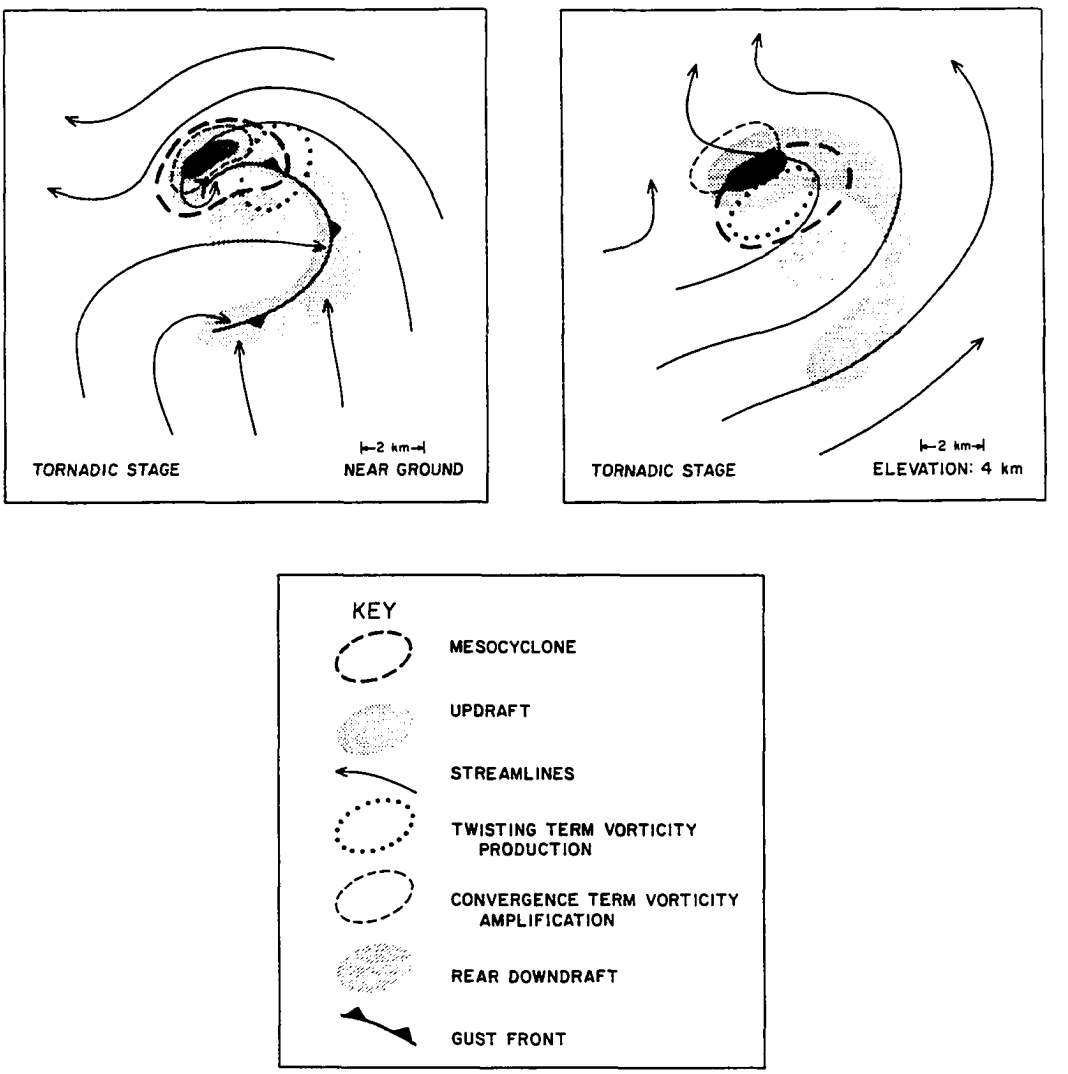

Figure 119. Pictoral summarization, as in Fig. 118, except for tornadic stage. Gust front, concentrated rear downdraft (hatched) and intense updraft (heavily stippled) added. The tornado (T) is located at the left hand tip of the gust front.

What causes mesocyclones to intensify? Klemp and Rotunno (1983) suppose that horizontal vorticity generated by thermal buoyancy could be important for intensifying mesocyclones when this vorticity is tilted along with ambient horizontal vorticity and stretched in updrafts. However, wind flow and temperature distributions varied considerably among observed storms suggesting this mechanism is not essential for mesocyclone intensification. No compelling observational evidence was uncovered for a rear downdraft transport of vertical vorticity and its subsequent stretching in updraft as postulated by Davies-Jones (1982). Instead, downdrafts were most often distinguished by anticyclonic vertical vorticity and weak horizontal vorticity. Strong vorticity generation by twisting occurs in tornadic mesocyclones; however, the horizontal vorticity tilted seems tied to the general build-up of vorticity and associates with subsiding air from the storm's rear. The common conspicuous characteristic observed during mesocyclone intensification is the rapid vorticity amplification by the convergence mechanism. The large vorticity production apparently stems from increased rainy downdraft-updraft interaction and occurs while both updraft and downdraft are intensifying. The enhanced low level convergence causes convergence term vorticity production to be 2-3 times that due to twisting at cloud base and even greater near ground. The ultimate source of mesocyclone vorticity appears to be the horizontal vorticity associated with the vertical shear of the environmental wind.

Computed mesocyclone properties did not readily explain tornado intensity. However, the close tie between mesocyclones and tornadoes makes it unlikely that mechanisms strongly affecting the parental

circulation would be unimportant and unrelated to tornadogenesis. Because the convergence term is the dominant vorticity producing mechanism during mesocyclone intensification and because air parcels in vicinity of the tornado pass through the region of maximum convergence term amplification, the data favor the hypothesis that tornadoes are triggered by the convergence mechanism.

Mesocyclone intensification at ground lowers the associated pressure deficit. Upward vertical perturbation pressure gradients in vicinity of the mesocyclone are reduced and eventually reversed by the vorticity build-up. The interpretation here is that the sudden formation of concentrated rear downdrafts in tornadic storms and the vertical velocity gradient across mesocyclones results from low level mesocyclone intensification and the ensuing pressure reduction at ground. Hence, rear downdrafts do not cause mesocyclone excitation but respond to it, i.e., the two-cell axial flow represents a fundamental change in mesocyclone dynamical properties. This explanation differs from that of Lemon and Doswell (1979) in which rear downdrafts result from pressure gradients associated with high pressure created at upper storm levels as strong tropospheric winds impinge upon the storm. The explanation given here is consistent with Klemp and Rotunno (1983) who found dynamically induced downdrafts in simulations of the tornadic region in severe thunderstorms.

Following tornado dissipation (Fig. 120), mesocyclone vertical vorticity and areal coverage diminished rapidly with height. Downdrafts spread throughout the mesocyclone which even in the lowest levels contains parcels from the storm's rear. Mesocyclone flow becomes increasingly divergent in the mean and the convergence term becomes dissipative.

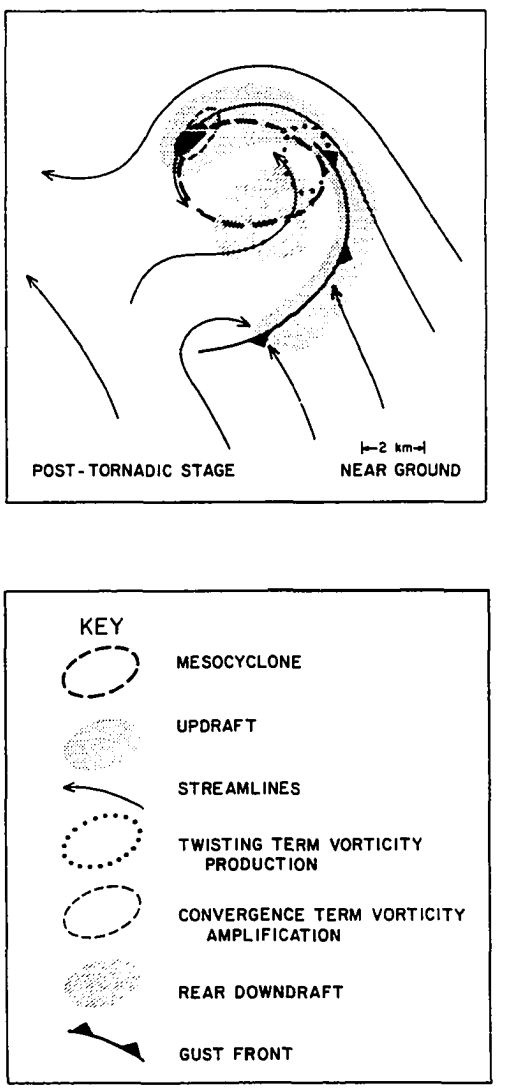

Figure 120. Pictoral summarization, as in Figs. 118 and 119, except for mesocyclone dissipation.

The data suggest that mesocyclone intensification may precipitate its decline. The lowering of the surface pressure deficit reduces the pressure gradient force that normally lifts nonbuoyant air at the base of updraft. Simultaneously, a large volume of environmental air, aided by horizontal pressure gradients, is entrained into the mesocyclone from the storm's rear. The entrained air typically has low equivalent potential temperature and therefore is potentially cold. When mixed with updraft air, updraft buoyancy is reduced. Thus, in final stages the mesocyclone fills with downdrafts, weakens and "separates" from the updraft.

Recapitulating, the principal findings and conclusions of this research are:

1) Low level vertical vorticity in tornadic thunderstorms seems to begin with the tilting of ambient vertical wind shear (horizontal vorticity) at the leading edge of the updraft and culminates with the subsequent amplification of this vorticity by the convergence term.

2) During tornadogenesis, vorticity amplification by the convergence term multiplies. The increased production, which results from the interaction between strengthening updraft and rainy downdraft, intensifies the mesocyclone and probably triggers tornadoes.

3) Rear downdrafts are produced by--rather than cause--mesocyclone intensification. Downdrafts are driven by vertical perturbation pressure forces that relate to the build-up of vorticity at low levels and foretell mesocyclone decline.

VII. REFERENCES

Abramowitz, M., and I. A. Stegun, 1964: Handbook of mathematical functions. National Bureau of Standards, Appl. Math. Ser. 55, U.S. Government Printing Office, Washington, D.C., p. 438.

Barnes, S. L., 1964: A technique for maximizing details in numerical weather map analysis. J. Appl. Meteor., 3, 396-409.

_____, 1970: Some aspects of a severe, right-moving thunderstorm deduced from mesonetwork rawinsonde observations. J. Atmos. Sci., 27, 634-648.

_____, 1978a: Oklahoma thunderstorms on 29-30 April 1970. Part I: Morphology of a tornadic storm. Mon. Wea. Rev., 106, 673-684.

_____, 1978b: Oklahoma thunderstorms on 29-30 April 1970. Part II: Radar-observed merger of twin hook echoes. Mon. Wea. Rev., 106, 685-696.

Bates, F. C., 1962: Tornadoes in the central United States. Transactions of the Kansas Academy of Science, 65, 215-246.

Blechman, J. B., 1981: Vortex generation in a numerical thunderstorm model. Mon. Wea. Rev., 109, 1061-1071.

Bonesteele, R. G., and Y. J. Lin, 1978: A study of updraft-downdraft interaction based on perturbation pressure and single-Doppler radar data. Mon. Wea. Rev., 106, 62-68.

Bradshaw, P., and Y. M. Koh, 1981: A note on Poisson's equation for pressure in a turbulent flow. Phys. Fluids, 24, p. 777.

Brandes, E. A., 1977a: Flow in severe thunderstorms observed by dual-Doppler radar. Mon. Wea. Rev., 105, 113-120.

_____, 1977b: Gust front evolution and tornado genesis as viewed by Doppler radar. J. Appl. Meteor., 16, 333-338.

_____, 1978: Mesocyclone evolution and tornadogenesis: Some observations. Mon. Wea. Rev., 106, 995-1011.

_____, 1981: Finestructure of the Del City-Edmond tornadic mesocirculation. Mon. Wea. Rev., 109, 635-647.

Brooks, E. M., 1949: The tornado cyclone. Weatherwise, 2, 32-33.

Browning, K. A., 1964: Airflow and precipitation trajectories within severe local storms which travel to the right of the winds. J. Atmos. Sci., 21, 634-668.

_____, 1968: The organization of severe local storms. Weather, 23, 429-434.

Burgess, D. W., 1976: Single Doppler radar vortex recognition: Part I - Mesocyclone signatures. Preprints, 17th Conf. Radar Meteor., Seattle, Amer. Meteor. Soc., 97-103.

_____, L. R. Lemon and R. A. Brown, 1975: Tornado characteristics revealed by Doppler radar. Geophys. Res. Lett., 2, 183-184.

_____, R. A. Brown, L. R. Lemon and C. R. Safford, 1977: Evolution of a tornadic thunderstorm. Preprints, 10th Conf. Severe Local Storms, Omaha, Amer. Meteor. Soc., 84-89.

Cressman, G. P., 1959: An operational objective analysis system. Mon. Wea. Rev., 87, 367-374.

Davies-Jones, R. P., 1982: Observational and theoretical aspects of tornadogenesis. Intense Atmospheric Vortices, Bengtsson and Lighthill, Eds., Springer-Verlag, 175-189.

Deardorff, J. W., 1970: A numerical study of three-dimensional turbulent channel flow at large Reynolds numbers. J. Fluid Mech., 41, 453-480.

Draginis, M., 1958: Liquid water within convective clouds. J. Meteor., 15, 481-485.

Environmental Data Service, 1974: Storm Data. Vol. 16, No. 6, U.S. Department of Commerce, Washington.

Fitzjarrald, D. E., 1973: A laboratory simulation of convective vortices. J. Atmos. Sci., 30, 894-902.

Foote, G. B., and P. S. du Toit, 1969: Terminal velocity of raindrops aloft. J. Appl. Meteor., 8, 249-253.

Fujita, T., 1965: Formation and steering mechanisms of tornado cyclones and associated hook echoes. Mon. Wea. Rev., 93, 67-78.

_____, 1973: Proposed mechanism of tornado formation from rotating thunderstorm. Preprints, 8th Conf. Severe Local Storms, Denver, Amer. Meteor. Soc., 191-196.

Gal-Chen, T., 1978: A method for the initialization of the anelastic equations: Implications for matching models with observations. Mon. Wea. Rev., 106, 587-606.

Gradshteyn, I. S., and I. M. Ryzhik, 1965: Table of Integrals, Series and Products, A. Jeffrey ed., Academic Press, p. 495.

Haltiner, G. J., and F. L. Martin, 1957: Dynamical and Physical Meteorology. McGraw-Hill, 214-221.

Hane, C. E., and B. C. Scott, 1978: Temperature and pressure perturbations within convective clouds derived from detailed air motion: Preliminary testing. Mon. Wea. Rev., 106, 654-661.

____, R. B. Wilhelmson and T. Gal-Chen, 1981: Retrieval of thermodynamic variables within deep convective clouds: Experiments in three dimensions. Mon. Wea. Rev., 109, 564-576.

Heymsfield, G. M., 1978: Kinematic and dynamic aspects of the Harrah tornadic storm analyzed from dual-Doppler data. Mon. Wea. Rev., 106, 233-254.

Klemp, J. B., and R. Rotunno, 1982: High resolution numerical simulations of the tornadic region within a mature thunderstorm. Preprints, 12th Conf. Severe Local Storms, San Antonio, Amer. Meteor. Soc., 532-535.

_____ and _____, 1983: A study of the tornadic region within a supercell thunderstorm. (Accepted forpublication in J. Atmos. Sci., February issue.)

_____ and R. B. Wilhelmson, 1978a: Simulations of right- and left-moving storms produced through storm splitting. J. Atmos. Sci., 35, 1097-1110.

_____ and _____, 1978b: The simulation of three-dimensional convective storm dynamics. J. Atmos. Sci., 35, 1070-1096.

_____, _____ and P. S. Ray, 1981: Observed and numerically simulated structure of a mature supercell thunderstorm. J. Atmos. Sci., 38, 1558-1580.

Leise, J. A., 1978: Temperature retrieval from dual-Doppler radar wind field data. Preprints, 18th Conf. Radar Meteor., Atlanta, Amer. Meteor. Soc., 94-99.

Lemon, L. R., and C. A. Doswell, III, 1979: Severe thunderstorm evolution and mesocyclone structure as related to tornadogenesis. Mon. Wea. Rev., 107, 1184-1197.

Lhermitte, R. M., and L. J. Miller, 1970: Doppler radar methodology for the observation of convective storms. Preprints, 14th Radar Meteor. Conf., Tucson, Amer. Meteor. Soc., 133-138.

Ludlam, F. H., 1963: Severe local storms: A review. Meteor. Monogr., No. 27, Amer. Meteor. Soc., 1-30.

Marshall, J. S., and W. Mck. Palmer, 1948: The distribution of raindrops with size. J. Meteor., 5, 165-166.

Ogura, Y., and N. A. Phillips, 1962: Scale analysis of deep and shallow convection in the atmosphere. J. Atmos. Sci., 19, 173-179.

Pasken, R., and Y. J. Lin, 1982: Pressure perturbations within a tornadic storm derived from dual-Doppler wind data. Preprints, 12th Conf. Severe Local Storms, San Antonio, Amer. Meteor. Soc., 257-260.

Ray, P. S., 1976: Vorticity and divergence fields within tornadic storms from dual-Doppler observations. J. Appl. Meteor., 15, 879-890.

___, B. C. Johnson, K. W. Johnson, J. S. Bradberry, J. J. Stephens, K. K. Wagner, R. B. Wilhelmson and J. B. Klemp, 1981: The morphology of several tornadic storms on 20 May 1977. J. Atmos. Sci., 38, 1643-1663.

Rodgers, R. R., 1964: An extension of the Z-R relation for Doppler radar. Preprints, 11th Weather Radar Conf., Boulder, Amer. Meteor. Soc., 158-161.

Rotunno, R., 1977: Numerical simulation of a laboratory vortex. J. Atmos. Sci., 34, 1942-1956.

Schlesinger, R. E., 1975: A three-dimensional numerical model of an isolated deep convective cloud: Preliminary results. J. Atmos. Sci., 32, 934-957.

_____, 1978: A three-dimensional numerical model of an isolated thunderstorm: Part I. Comparative experiments for variable ambient wind shear. J. Atmos. Sci., 35, 690-713.

Shuman, F. G., 1957: Numerical methods in weather prediction: II. Smoothing and filtering. Mon. Wea. Rev., 85, 357-361.

Starr, V. P., 1976: Factors related to the inception of tornado funnels. Rivista Italiana Di Geofisica, 3, 1-7.

Stratton, J. A., 1941: Electromagnetic theory, McGraw-Hill, p. 410.

Ward, N. B., 1962: The effect of low level wind shear on the formation of atmospheric vortices. Preprints, 2nd Conf. Severe Local Storms, Norman, Amer. Meteor. Soc.

____, 1972: The exploration of certain features of tornado dynamics using a laboratory model. J. Atmos. Sci., 29, 1194-1204.

Wilhelmson, R., and Y. Ogura, 1972: The pressure perturbation and the numerical modeling of a cloud. J. Atmos. Sci., 29, 1295-1307.

_____ and J. B. Klemp, 1978: A numerical study of storm splitting that leads to long-lived storms. J. Atmos. Sci., 35, 1974-1986.

APPENDIX A

PARAMETERIZATION OF SUBGRID TURBULENCE

Effects of subgrid turbulence on resolvable scales of motion are determined following the procedure described by Deardorff (1970) as adapted by Schlesinger (1978) for anelastic flow. Subgrid turbulent forces $F_i(x,y,z)$ are expressed as Reynolds stress divergences

$$F_i = -\frac{1}{\rho_o}\vec{\nabla}\cdot\rho_o\overline{u_i'\vec{V}'}$$

where primes indicate turbulent fluctuations and the overbar represents grid scale volume averages. Velocity variances and covariances are computed from

$$u_i'u_j' = \frac{2}{3}\delta_{ij}E - K_m\left(\frac{\partial u_i}{\partial x_j} + \frac{\partial u_j}{\partial x_i} - \delta_{ij}\frac{D}{3}\right)$$

where E is the subgrid scale kinetic energy per unit mass (assumed to be partitioned equally among the variances), K_m is the momentum eddy mixing coefficient, $D = -\frac{w}{\rho_o}\frac{\partial\rho_o}{\partial z} = \vec{\nabla}\cdot\vec{V}$ and δ_{ij} is the Kronecker delta. The mixing coefficient is taken to be

$$K_m = (0.2\Delta)^2 \quad |\mathrm{Def}|$$

where $\Delta = (\Delta x \Delta y \Delta z)^{1/3}$ and the deformation Def is given by

$$|Def|^2 = \frac{1}{2} \sum_{i=1}^{3} \sum_{j=1}^{3} \left(\frac{\partial u_i}{\partial x_j} + \frac{\partial u_j}{\partial x_i} - \frac{2}{3} \delta_{ij} D\right)^2$$

The kinetic energy then becomes

$$E = 3K_m |Def| \quad .$$

Forces were computed at locations coincident with the thermodynamic variables. For computation purposes, the normal derivatives of the turbulent forces are assumed to be zero at the grid domain boundaries.

APPENDIX B

DERIVATION OF THE ELLIPTIC EQUATIONS FOR PRESSURE AND TEMPERATURE

To derive the pressure equation the momentum equations (1) are written

$$c_p\theta_{vo}\vec{\nabla}\pi' = -\frac{\partial\vec{V}}{\partial t} - (\vec{V}\cdot\vec{\nabla})\vec{V} + \vec{F} + \vec{k}g\left(\frac{\theta'}{\theta_o} + aq_v' - q_c\right) \quad ,$$

multiplied by $\rho_o(z)$, and the divergence taken to yield

$$\vec{\nabla}\cdot\rho_o c_p\theta_{vo}\vec{\nabla}\pi' = -\vec{\nabla}\cdot\rho_o\frac{\partial\vec{V}}{\partial t} - \vec{\nabla}\cdot\rho_o(\vec{V}\cdot\vec{\nabla})\vec{V} + \vec{\nabla}\cdot\rho_o\vec{F} + \vec{\nabla}\cdot\rho_o\vec{k}g\left(\frac{\theta'}{\theta_o} + aq_v' - q_c\right) \quad .$$

The first term on the right can be written $-\frac{\partial}{\partial t}\vec{\nabla}\cdot\rho_o\vec{V}$ and is zero by the anelastic continuity Eq. (2). Selectively performing vector operations, dividing by $\rho_o c_p\theta_{vo}$ and rewriting gives Eq. (6)

$$\nabla^2\pi' + \frac{\partial \ell n(\rho_o\theta_{vo})}{\partial z}\frac{\partial\pi'}{\partial z} = \frac{1}{c_p\theta_o}\left\{-\frac{1}{\rho_o}\vec{\nabla}\cdot\rho_o(\vec{V}\cdot\vec{\nabla})\vec{V} + \frac{g}{\rho_o}\frac{\partial}{\partial z}\left[\rho_o\left(\frac{\theta'}{\theta_o} + aq_v' - q_c\right)\right] + \frac{1}{\rho_o}\vec{\nabla}\cdot\rho_o\vec{F}\right\} \quad .$$

To express the dynamical forcing $\frac{1}{\rho_o}\vec{\nabla}\cdot\rho_o(\vec{V}\cdot\vec{\nabla})\vec{V}$ in terms of vorticity and strain, write in scalor form, i.e.,

$$u \frac{\partial^2 u}{\partial x^2} + v \frac{\partial^2 v}{\partial y^2} + w \frac{\partial^2 w}{\partial z^2}$$

$$+ u \frac{\partial}{\partial y}\left(\frac{\partial v}{\partial x}\right) + u \frac{\partial}{\partial z}\left(\frac{\partial w}{\partial x}\right) + v \frac{\partial}{\partial x}\left(\frac{\partial u}{\partial y}\right) + v \frac{\partial}{\partial z}\left(\frac{\partial w}{\partial y}\right) + w \frac{\partial}{\partial x}\left(\frac{\partial u}{\partial z}\right) + w \frac{\partial}{\partial y}\left(\frac{\partial v}{\partial z}\right)$$

$$+ \left(u \frac{\partial w}{\partial x} + v \frac{\partial w}{\partial y} + w \frac{\partial w}{\partial z}\right) \frac{\partial \ell n \rho_o}{\partial z}$$

$$+ \left(\frac{\partial u}{\partial x}\right)^2 + \left(\frac{\partial v}{\partial y}\right)^2 + \left(\frac{\partial w}{\partial z}\right)^2$$

$$+ 2\left(\frac{\partial v}{\partial x}\frac{\partial u}{\partial y} + \frac{\partial w}{\partial x}\frac{\partial u}{\partial z} + \frac{\partial w}{\partial y}\frac{\partial v}{\partial z}\right) \quad .$$

Collectively, the first nine terms and the continuity equation yield

$$- \frac{\partial \ell n \rho_o}{\partial z}\left(u \frac{\partial w}{\partial x} + v \frac{\partial w}{\partial y} + w \frac{\partial w}{\partial z}\right) - w^2 \frac{\partial^2 \ell n \rho_o}{\partial z^2} \quad .$$

Thus, the dynamic term reduces to

$$\left(\frac{\partial u}{\partial x}\right)^2 + \left(\frac{\partial v}{\partial y}\right)^2 + \left(\frac{\partial w}{\partial z}\right)^2$$

$$+ 2\left(\frac{\partial v}{\partial x}\frac{\partial u}{\partial y} + \frac{\partial w}{\partial x}\frac{\partial u}{\partial z} + \frac{\partial w}{\partial y}\frac{\partial v}{\partial z}\right) - w^2 \frac{\partial^2 \ell n \rho_o}{\partial z^2}$$

which after some algebraic manipulation becomes

$$\frac{1}{4}\left[\left(\frac{\partial u}{\partial x} + \frac{\partial u}{\partial x}\right)^2 + \left(\frac{\partial v}{\partial y} + \frac{\partial v}{\partial y}\right)^2 + \left(\frac{\partial w}{\partial z} + \frac{\partial w}{\partial z}\right)^2 + 2\left(\frac{\partial v}{\partial x} + \frac{\partial u}{\partial y}\right)^2 + 2\left(\frac{\partial u}{\partial z} + \frac{\partial w}{\partial x}\right)^2 + 2\left(\frac{\partial w}{\partial y} + \frac{\partial v}{\partial z}\right)^2\right]$$

$$- \frac{1}{2}\left[\left(\frac{\partial w}{\partial y} - \frac{\partial v}{\partial z}\right)^2 + \left(\frac{\partial u}{\partial z} - \frac{\partial w}{\partial x}\right)^2 + \left(\frac{\partial v}{\partial x} - \frac{\partial u}{\partial y}\right)^2\right] - w^2 \frac{\partial^2 \ell n \rho_o}{\partial z^2} \quad .$$

Recalling the definition of the strain tensor, i.e., $e_{ij} = \frac{1}{2}(\frac{\partial u_i}{\partial x_j} + \frac{\partial u_j}{\partial x_i})$ where $e_{ij} = e_{ji}$, and the definitions of the vorticity components; it follows that

$$-\frac{1}{\rho_o}\vec{\nabla}\cdot\rho_o(\vec{V}\cdot\vec{\nabla})\vec{V} = -e^2 + \frac{1}{2}(\xi^2+\eta^2+\zeta^2) + w^2\frac{\partial^2 \ell n\rho_o}{\partial z^2}$$

and

$$\nabla^2\pi' + \frac{\partial \ell n(\rho_o\theta_{vo})}{\partial z}\frac{\partial\pi'}{\partial z} = \frac{1}{c_p\theta_{vo}}\left\{-e^2 + \frac{1}{2}(\xi^2+\eta^2+\zeta^2) + w^2\frac{\partial^2 \ell n\rho_o}{\partial z^2}\right.$$

$$\left. + \frac{g}{\rho_o}\frac{\partial}{\partial z}[\rho_o(\frac{\theta'}{\theta_o} + aq_v'-q_c)] + \frac{1}{\rho_o}\vec{\nabla}\cdot\rho_o\vec{F}\right\} .$$

To obtain the equation for temperature the curl of the curl of the momentum Eqns. (1) is taken and the result dot multiplied by $\vec{k}$, i.e.,

$$\vec{k}\cdot\vec{\nabla}x\vec{\nabla}x\frac{d\vec{V}}{dt} = -\vec{k}\cdot\vec{\nabla}x\vec{\nabla}x[c_p\theta_{vo}\vec{\nabla}\pi' - \vec{F} - \vec{k}g(\frac{\theta'}{\theta_o} + aq_v'-q_c)] .$$

Solving for $\nabla_H^2\theta'$ where $\nabla_H^2 = \frac{\partial^2}{\partial x^2} + \frac{\partial^2}{\partial y^2}$ leads to Eq. (7)

$$\nabla_H^2\theta' = -\frac{\theta_o}{g}\left\{\vec{k}\cdot\vec{\nabla}x\vec{\nabla}x[\frac{d\vec{V}}{dt} + c_p\theta_{vo}\vec{\nabla}\pi' - \vec{F} - \vec{k}g(aq_v'-q_c)]\right\} .$$

Similarly, the curl of the three-dimensional vorticity Eq. (4) when dot multiplied by $\vec{k}$ and after neglecting the small pressure term yields Eq. (11)

$$\nabla_H^2\theta' = -\frac{\theta_o}{g}\left\{\vec{k}\cdot\vec{\nabla}x[\frac{d\vec{\omega}}{dt} - (\vec{\omega}\cdot\vec{\nabla})\vec{V} + \vec{\omega}(\vec{\nabla}\cdot\vec{V})] - \vec{k}\cdot\vec{\nabla}x\vec{\nabla}x[\vec{F} + \vec{k}g(aq_v'-q_c)]\right\} .$$

Introducing the vectoral component form for $\vec{\omega}$, i.e., $\vec{\omega} = \xi\vec{i} + \eta\vec{j} + \zeta\vec{k}$, and performing the indicated vector operations gives the scalar Eq. (12)

$$\nabla_H^2\theta' = -\frac{\theta_o}{g}\left\{\frac{\partial}{\partial y}\left[\frac{d\xi}{dt} + \left(\frac{\partial v}{\partial y} + \frac{\partial w}{\partial z}\right)\xi - \eta\frac{\partial u}{\partial y} - \zeta\frac{\partial u}{\partial z}\right]\right.$$

$$-\frac{\partial}{\partial x}\left[\frac{d\eta}{dt} + \left(\frac{\partial u}{\partial x} + \frac{\partial w}{\partial z}\right)\eta - \xi\frac{\partial v}{\partial x} - \zeta\frac{\partial v}{\partial z}\right]$$

$$\left.-\nabla_H^2\left[g(aq_v' - q_c) - F_z\right] + \frac{\partial}{\partial z}\left[\frac{\partial F_x}{\partial x} + \frac{\partial F_y}{\partial y}\right]\right\} \quad .$$

APPENDIX C

RESPONSE OF A TRUNCATED GAUSSIAN WEIGHT FUNCTION

The response σ of the three-dimensional weight function $h(r)$ for a finite influence radius r_* is given by

$$\sigma = \int_0^{r_*} \int_0^{2\pi} \int_0^{\pi} e^{-i\vec{K}\cdot\vec{r}}\, h(r)\, dV$$

where $dV = r^2 dr \sin\theta d\theta\, d\phi$

$$K = \frac{2\pi}{\lambda}$$

$$h(r) = e^{-r^2/\nu}$$

and where $\vec{r}$ is a positioning vector, $\vec{K}$ is the wave number vector, λ is the wavelength, $i=\sqrt{-1}$ and ν is a filtering parameter (0.54 km^2 in this study). If the spherical coordinate system is rotated such that $\vec{K}$ is parallel to the z axis (Fig. C1), then $\vec{K}\cdot\vec{r} = Kr\cos\theta$.

The angular portion of the response function is expressed

$$\sigma_\Omega = \int_0^{2\pi} \int_0^{\pi} e^{-iKr\cos\theta} \sin\theta d\theta\, d\phi$$

which after integrating with respect to ϕ yields

$$\sigma_{\Omega} = 2\pi \int_{0}^{\pi} e^{-iKr\cos\theta} \sin\theta d\theta \quad .$$

Integration over θ (Stratton, 1941; p. 410) gives

$$\sigma_{\Omega} = 4\pi j_{0}(Kr)$$

where $j_0(Kr)$ is the spherical Bessel function of zero order. This expression can be written

$$\sigma_{\Omega} = 4\pi \frac{\sin Kr}{Kr}$$

(Abramowitz and Stegun, 1964, p. 438). Hence the response function becomes

$$\sigma = 2\lambda \int_{0}^{r_*} r\, e^{-r^2/\nu} \sin \frac{2\pi r}{\lambda}\, dr \quad .$$

The desired form, found by normalizing the integral with the value for $r_* = \infty$ (see p. 495; Gradshteyn and Ryzhik, 1965), is

$$\sigma = \frac{2\lambda}{\pi\sqrt{\pi}\nu^{3/2}} \int_{0}^{r_*} r\, e^{-r^2/\nu} \sin \frac{2\pi r}{\lambda}\, dr \quad .$$

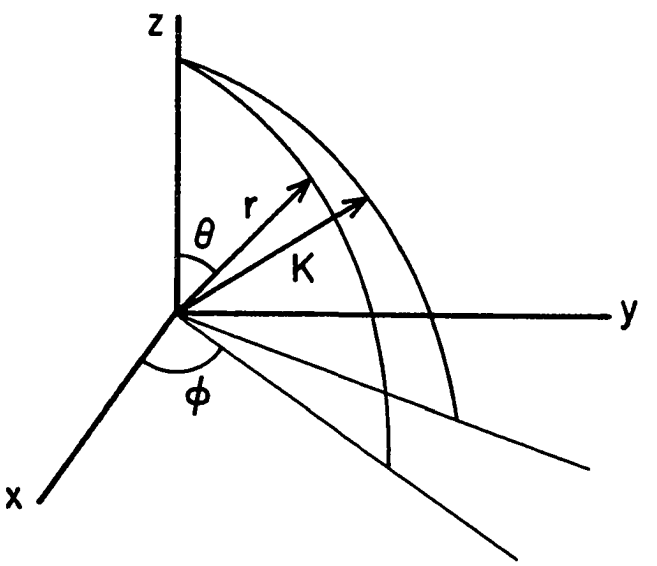

Figure C1. Three-dimensional schematic diagram of the position vector $\vec{r}$ and the wave number vector $\vec{K}$.